Laser-induced Breakdown and Evaporation of Single and Multicomponent Liquid Droplets

Ph.D. Thesis

by

VISHAL JAGADALE

DEPARTMENT OF MECHANICAL ENGINEERING
INDIAN INSTITUTE OF TECHNOLOGY INDORE

June 2024

Laser-induced Breakdown and Evaporation of Single and Multicomponent Liquid Droplets

A THESIS

Submitted in partial fulfillment of the
requirements for the award of the degree
of
DOCTOR OF PHILOSOPHY

by

VISHAL JAGADALE

DEPARTMENT OF MECHANICAL ENGINEERING
INDIAN INSTITUTE OF TECHNOLOGY INDORE

June 2024

INDIAN INSTITUTE OF TECHNOLOGY INDORE

I hereby certify that the work which is being presented in the thesis entitled **Laser-induced Breakdown and Evaporation of Single and Multicomponent Liquid Droplets** in the partial fulfillment of the requirements for the award of the degree of **DOCTOR OF PHILOSOPHY** and submitted in the **Department of Mechanical Engineering, Indian Institute of Technology Indore**, is an authentic record of my own work carried out during the time period from December 2018 to April 2024 under the supervision of Dr. Devendra L. Deshmukh, Professor, IIT Indore and Dr. Yogeshwar Nath Mishra, Research Scientist, KAUST, Saudi Arabia.

The matter presented in this thesis has not been submitted by me for the award of any other degree of this or any other institute.

14/06/2024

Signature of the student with date
(VISHAL S. JAGADALE)

This is to certify that the above statement made by the candidate is correct to the best of my/our knowledge.

14/06/2024

Signature of Thesis Supervisor #1 with date

DEVENDRA L. DESHMUKH

14/06/2024

Signature of Thesis Supervisor #2 with date

YOGESHWAR NATH MISHRA

VISHAL S. JAGADALE has successfully given his/her Ph.D. Oral Examination held on **<Date of PhD Oral Examination>**.

Signature of Thesis Supervisor #1 with date

DEVENDRA L. DESHMUKH

Signature of Thesis Supervisor #2 with date

YOGESHWAR NATH MISHRA

ACKNOWLEDGEMENTS

Crafting the acknowledgment section of a Ph.D. thesis is akin to rolling the credits of a movie - reading it brings both ease and nostalgia, evoking the journey of the research duration. However, composing it presents a unique challenge, akin to the gap between planning experiments and their execution, always taking longer than expected. But to get dressed up in the doctoral cap and gown marks a personal milestone that everyone must experience, encompassing both bitter and sweet moments. Thankfully, in this journey I have met so many wonderful colleagues at work and made so many warm-hearted friends in life, to whom I would like to express my sincerest gratitude.

I am deeply grateful to my gurus for their invaluable guidance, unwavering support, and constant encouragement throughout my journey. Prof. Devendra Deshmukh, my supervisor, has been my mentor since my arrival at IIT Indore as an M.Tech. project intern. I also extend my heartfelt appreciation to my co-supervisor, Dr. Yogeshwar Nath Mishra, for his unwavering support and guidance throughout my Ph.D. journey. Their words of encouragement gave me the Spark and confidence to face my anxiety and unease. The mentorship provided by both has played a pivotal role in shaping my research trajectory and guiding me towards the attainment of my goals.

I thank my PSPC members, Prof. Amod Umarikar, and Prof. Santosh Sahu for their valuable input, constant support, encouragement, and assistance throughout my research. I am also grateful to DPGC, departmental head, and other staff members for their support and guidance.

I would like to extend my heartfelt gratitude to Prof. Dag, Ademir, Lu Di, and the entire team at the University of Gothenburg for their support and encouragement. I would also like to acknowledge the support from Prof. Mats from Chalmers for the experiments with UV Laser. A big thank you to Dr. Chaitanya Rao (IITK) and Dr. Amit (Chalmers) for their invaluable support and contributions. Without them, the experimental campaign would not have been possible and fun.

I am truly grateful for having such a wonderful colleague, Devashish, Arpit, and my seniors Dr. Vasudev, Dr. Aniket, Dr. Rajan, and Dr. Jyotirmoy, for their constant support, guidance, and motivation throughout my Ph.D. journey. I would especially like to thank them for the on-research and off-research discussions and bits of advice. A special thanks to my institute friends Anuj, Ajinkya, Anupam, Vivek, Pankaj, Bhavesh, Rajnish, Ram, Shree, Yogesh for their unwavering support and friendship throughout my academic journey. Without them, the Ph.D. journey would have been less pleasant and fun.

I am also grateful to the lab manager Mr. Ashwin Wagh for his technical support and time-to-time life advice. Similarly, I would like to thank Mr. Ashwin Patil for his help in materials procurement and complex fabrication along with other valuable support.

A special thanks to my Undergraduate friends: Shrivallabh, Akshay, Pavan, Aba, Rohit, Hanmant, Vikas, Nitin, (et al.), my M.Tech friends: Shashank, Abhijeet, Atul, Vivek, Hitendra, Vandan, Yash, (et al.) and my childhood friends and others for their constant support and encouragement.

I am thankful to Dr. Sagar, Uma Mai and Balu mama for their support and the long discussions. Sagar has been an integral part of my research journey, contributing through our intense and passionate discussions about our innovative and ambitious ideas. I would like to thank my dear friends Dadasaheb, Lavaji, Pradip, Swapnil and Nilesh for their immensely inquisitive questions, interest, and encouragement. My lovely nephews have brought priceless happiness to my daily routine.

Finally, I would like to express my deepest gratitude to my family. My parents, my wife, younger brother Sahebrao, Younger sister Vaishali, and cousins Varsha, Vikram, Navnath, Amol and others for their constant love, support, and encouragement throughout my academic journey. Their unwavering faith in me has been the driving force behind my success. I cannot say enough how grateful I feel to have been born into such a family and how much I love them.

Thank you all for being a part of my academic journey and for your invaluable support, guidance, and encouragement. I could not have achieved this milestone without you.

Vishal Jagadale

// हा शोध-प्रबंध माझ्या कुटुंबाला समर्पित आहे //

This thesis is dedicated to my family, immediate and beyond…

// यह शोध-प्रबन्ध मेरे परिवार को समर्पित है //

“Science is a journey that offers an endless array of surprises and wonders”.

……Antoine Lavoisier

“It doesn’t matter how beautiful theory is,
it doesn’t matter how smart you are,
if it doesn’t agree with experiments, it is wrong”.

……. Richard P. Feynman

Abstract

Single droplets studies involving breakup hydrodynamics and evaporation are important for optimizing many industrial applications. This dissertation focuses on studying the sequence of events involved in the laser-induced breakup of single and multi-component liquid droplets using time-resolved high-speed imaging techniques. Laser Induced Breakdown (LIB) is used to investigate the fundamental physics of fluid dynamics and fragmentation phenomenon of acoustically levitated single droplet of pure component liquids (water, ethanol, n-hexane, and iso-octane), and multicomponent liquids (diesel, Rapeseed Methyl Ester (RME), and their emulsions. This study represents a systematic attempt to analyze the sequence of events within a single droplet of fuel, encompassing bubble generation, growth, coalescence, rupture, droplet stretching, and eventual breakup.

This study is divided into two parts: the first part focuses on the laser-induced breakdown, while the second part examines the droplet evaporation. The results obtained from LIB are categorized into two sub parts: early time dynamics and late time dynamics. Early time dynamics reveals the deformation, bubble creation and its dynamics, while the late time dynamics delves into the expansion dynamics and subsequent breakup of the liquid droplets. High-speed imaging reveals distinct atomization patterns, with biofuel emulsions showing higher breakup strength and ethanol addition enhancing atomization efficiency. Fragmentation mechanisms involve Rayleigh–Taylor instabilities, with properties like phase changes and viscosity influencing breakup violence. In femtosecond laser studies, bubble diameter and breakup have a logarithmic relationship with laser energy. The consecutive pulses lead to bubble coalescence through the Bjerknes force. Droplet behavior varies with laser energy, resulting in different sheet formations and breakups. We quantify the secondary droplet size distribution and ligament analysis of single and multicomponent liquid droplets following the atomization processes. The mathematical formulations explain the deformation, expansion dynamics, and associated instabilities in the sheet breakup. Finally, this study explores the laser-induced evaporation of cellulose nanocrystals (CNCs), carboxymethyl cellulose (CMC), and silica droplets. It reveals morphological changes in these droplets across different sample concentrations and varying laser energies. The investigation highlights differences in evaporation rates and structural outcomes. CNC droplets self-assemble into ordered structures, while CMC droplets form gel-like structures due to polymer chain entanglement. Silica droplets rapidly evaporate, deform, nucleate, and fragment under laser heating.

LIST OF PUBLICATIONS

A. Journal papers included in thesis:

1. **Vishal S. Jagadale**, DCK Rao, D. Deshmukh, D. Hanstorp, Y.N. Mishra, "Modes of atomization in biofuel droplets induced by a focused laser pulse", **Fuel 2022**;315:123190. https://doi.org/10.1016/j.fuel.2022.123190. (I. F.: 7.4).

2. **Vishal S. Jagadale,** D. Deshmukh, D. Hanstorp, Y.N. Mishra "Bubble dynamics and atomization of acoustically levitated fuel droplet using femtosecond laser pulses", **Scientific Reports**, (2024) 14:8285. https://doi.org/10.1038/s41598-024-57802-8. (I. F.: 4.6).

3. **Vishal S. Jagadale,** D. Chorey, D. Deshmukh, D. Hanstorp, Y. Mishra "Ultraviolet laser-induced fragmentation of hydrocarbon fuel droplets", **Physics of Fluids,** 36, 097127 (2024). https://doi.org/10.1063/5.0223143. (I. F.: 4.1).

B. International Conferences:

1. **Vishal S. Jagadale,** D. Deshmukh, D. Hanstorp, and Y. Mishra "*Fragmentation of acoustically levitated fuel droplets using femto-nanosecond laser*", **Droplets 2021**, Fifth international conference on droplets, TU Dermstad.

2. **Vishal S. Jagadale,** D. Chorey, D. Deshmukh, D. Hanstorp, Mats Anderson, and Y. N. Mishra "*Laser-Induced breakdown in acoustically levitated fuel droplets",* **ILASS-Asia 2022,** 22nd Annual conference of Institute for Liquid Atomization and Spray Systems-Asia.

C. Journal Papers not included in thesis:

1. V. D. Choudhary, **V. Jagdale**, D. Chorey, and D. Deshmukh, "Combustion and spray breakup characteristics of biodiesel for cold start application," **Cleaner Engineering and Technology**, (2021). https://doi.org/10.1016/j.clet.2021.100285. (Impact Factor:5.3).
2. D. Chorey, **V. S. Jagadale**, M. Prakash, D. Hanstorp, M. Andersson, D. Deshmukh, and Y. N. Mishra, "Simultaneous CH*, C2* and temperature in flames using a DSLR camera and structured illumination "**Applied Optics**, 69(14), (2023). https://doi.org/10.1364/AO.484213. (Impact Factor:1.7).

TABLE OF CONTENTS

LIST OF PUBLICATIONS ..... **i**
TABLE OF CONTENTS ..... **ii**
LIST OF FIGURES ..... **v**
LIST OF TABLES ..... **x**
NOMENCLATURE ..... **xi**
1. Introduction **1**
1.1. Motivation and background 1
1.2. Droplet Atomization/Fragmentation 2
1.3. Droplet Evaporation 4
1.4. Summary 5
1.5. A guide through the thesis 6
2. Literature Review **7**
2.1. Laser matter interactions 7
2.2. Laser-Induced Breakdown (LIB) 8
2.1.1. Mechanisms of LIB 9
2.1.2. Plasma formation 11
2.1.3. Shock wave generation 13
2.1.4. Bubble generation 14
2.1.5. Breakup mechanisms and instabilities 15
2.3. Single droplet Levitation 16
2.4. Scope and objective of the study 18
3. Experimental setup and methodology **19**
3.1. Experimental setup 19
3.1.1. Laser setup 19
3.1.2. Imaging system 22
3.1.3. Optics 23
3.2. Laser induced evaporation of the droplets 23
3.3. Acoustic levitation 25
3.4. Droplet generation and levitation system 27
3.5. Image processing and data extraction 28
3.6. Fuel preparation and its properties 28
3.7. Summary 29

4. Femtosecond laser induced breakdown in liquid droplets 31
4.1. Bubble creation and dynamics 32
4.2. Process of droplet stretching and coalescence of secondary droplets 38
4.3. Sheet Breakup 39
4.3.1. Stable sheet collapse 40
4.3.2. Unstable sheet breakup 44
4.4. Catastrophic breakup 45
4.5. Overview of the FS laser study 47
4.5.1. Results for RME 47
4.5.2. Secondary droplet size distribution 49
4.5.3. Dimensionless number distribution 49
4.6. Summary 52
5. Nanosecond laser induced breakdown in liquid droplets-532 nm 53
5.1. Fragmentation of single component liquids 53
5.1.1. Air Entrapment 53
5.1.2. Breakup mechanisms with different laser energies 54
5.2. Fragmentation of multicomponent liquids 56
5.3. Ligament analysis and secondary droplet distribution 59
5.4. Overview of the nanosecond laser study 64
5.5. Summary 65
6. Ultraviolet-Nanosecond laser induced breakdown in liquid droplets 67
6.1. Plasma formation and Shock wave dynamics 68
6.2. Expansion dynamics 69
6.3. Fragmentation of Iso-octane droplet 72
6.3.1. Complete atomization 73
6.3.2. Droplet deformation and propulsion 75
6.3.3. Sheet breakup through hole formation 77
6.3.4. Stable sheet collapse 80
6.4. Fragmentation of n-hexane droplet 81
6.5. Shear layer formation in fragmenting drop 83
6.6. Fragments impact on the liquid sheet 85
6.7. Instabilities 86
6.7.1. Rayleigh-Taylor (RT) 86
6.7.2. Rayleigh-Plateau (RP) 88

6.7.3. Kelvin–Helmholtz (KH) 89
6.8. Summary 90
7. Droplet Evaporation 91
7.1. Introduction 91
7.2. Laser induced evaporation of CNCs drops 92
7.3. Laser induced evaporation of CMC drops 97
7.4. Laser induced evaporation of Silica drops 99
7.5. Summary 102
8. Conclusions and future scope 103
8.1. Conclusions 103
8.2. Future scope 105
Appendix 106
References 108

LIST OF FIGURES

Figure 1. Processes involved in LIB and its applications. 10

Figure 2. Schematics of plasma formation and shock wave travel during laser droplet interaction. 12

Figure 3. Schematic top view of the experimental setup for laser-induced fragmentation of levitated droplets. The inset represents the droplet configuration used for analysis. 20

Figure 4. Experimental setup for nanosecond laser-induced fragmentation of levitated droplet [131] 21

Figure 5. Experimental setup for femtosecond laser-induced fragmentation of acoustically levitated droplet [132] 22

Figure 6. Experimental setup for laser-induced evaporation of liquid droplets. .. 24

Figure 7. Schematic setup for laser-induced evaporation studies of liquid droplets. 24

Figure 8. Acoustic levitator demonstration: a) Actual droplets trapped in the Acoustic trap b) Acoustic levitation of a small droplet at the pressure node of a plane standing wave formed between transducer c) Experimental setup for the droplet levitation. 26

Figure 9. Graphical depiction of the sequential dynamics of laser-droplet interaction through multiple laser pulses[132]. 32

Figure 10. Regimes of bubble dynamics in a diesel droplet through the interaction of multiple femtosecond laser pulses at El = 250 μJ, D_0 = 1.4 mm. The dotted rectangles highlight the creation of bubbles by individual laser pulses[132]..... 33

Figure 11. Variation of drainage time with equivalent bubble radius of diesel droplet. The inset provides a visual representation of the coalescence process and the parameters employed for the analysis[132]. 35

Figure 12. Variation of Bjerknes force with equivalent bubble radius for diesel fuel at E_l = 250 μJ [132] 37

Figure 13. Ligament-mediated breakup in a diesel droplet through the interaction of multiple femtosecond laser pulses at E_l = 250 μJ and D_0 = 0. 9 mm [132]. .. 39

Figure 14. The process of stable sheet formation in a diesel droplet through the interaction of multiple femtosecond laser pulses at E_l = 1050 µJ and D_0 = 1.1 mm [132]. 40

Figure 15. Experimental and theoretical comparison of temporal variation of the normalized length scale of the sheet. The inset represents the temporal variation of rim diameter for the stable sheet[132]. 42

Figure 16. The process of unstable sheet breakup in a diesel droplet through the interaction of multiple femtosecond laser pulses at E_l = 1050 µJ and D_0 = 0.95 mm[132]. 45

Figure 17. Catastrophic breakdown in a diesel droplet through the interaction of multiple femtosecond laser pulses at E_l = 1050 µJ and D_0 = 0.55 mm [132]. ... 46

Figure 18. Time sequence images of RME droplet showing bubble dynamics and breakup through the interaction of multiple femtosecond laser pulses for different laser energy (E_l) and D_0 = 1.0 mm [132]..... 47

Figure 19. Normalized secondary droplet size distribution of the diesel and RME corresponding to a laser pulse energy of 1050 µJ, and onset droplet diameter of D_0 = 1.0 mm. Inset inside the Fig. 12 represents the probability density function plotted against normalized secondary drop size for diesel and RME droplets. Where D_s and D_0 are the secondary and onset droplet diameters respectively[132]. 48

Figure 20. Regime map of temporal variation of a normalized bubble size distribution at different laser pulse energies for the diesel and RME droplet [132]. 50

Figure 21. The detailed mapping of breakup features observed in the current study [132]. 51

Figure 22. Fragmentation and subsequent air entrapment in water droplet: E_l = 0.5 mJ, D_0 = 0.6 mm, and the maximum diameter of bubble is 0.52 mm [131]..... 53

Figure 23. Fragmentation of water droplet: a) unstable sheet at E_l = 3.14 mJ, D_0 = 0.9 mm b) Stable stretched sheet at E_l = 2.5 mJ, D_0 = 1.1 mm c) Stable stretched sheet E_l = 5.3 mJ, D_0 = 1.3 mm d) prompt fragmentation at E_l = 7.15 mJ, D_0 = 1.2 mm [131]. 54

Figure 24. Fragmentation of Ethanol droplet at different laser energies: a) E_l = 2.5 mJ, D_0 = 1.4 mm b) E_l = 5.3 mJ, D_0 = 1.3 mm c) E_l = 7.15 mJ, D_0 = 1.5 mm [131].....55

Figure 25. Fragmentation of RME droplet at different laser energies: a) E_l = 1.2 mJ, D_0 = 1.4 mm b) E_l = 2.5 mJ, D_0 = 1.2 mm c) E_l = 7.15 mJ, D_0 = 1.8 mm[131]. 57

Figure 26. Fragmentation of RE30 droplet: a) E_l = 0.5 mJ, D_0 = 1.1 mm b) E_l = 1.2 mJ, D_0 = 0.9 mm c) E_l = 2.5 mJ, D_0 = 1 mm[131]. 58

Figure 27. Fragmentation of RE50 droplet: a) E_l = 0.5 mJ, D_0= 1 mm b) E_l = 2.5 mJ, D_0= 0.9 mm[131]. 58

Figure 28. Fragmentation of RE30 droplet at E_l = 2.5 mJ: a) Unstable prompt fragmentation (D_0= 0.6 mm) b) Prompt fragmentation (D_0 = 0.25 mm)[131]...59

Figure 29. Variation of ligament breakup time with ligament diameter for different liquids[131].....60

Figure 30. Variation of secondary drop size with (a) Ligament diameter and (b) secondary drop velocity[131]. 61

Figure 31. Number of drops plotted against the secondary droplet size at E_l = 5.3 mJ, D_0 ~ 1.2 mm for different liquid droplets water, ethanol, RME, RE30, and RE50[131].....63

Figure 32. Overview of nanosecond laser-induced fragmentation for different liquid droplets[131]. 64

Figure 33. Plasma and shock wave generation dynamics during laser droplet interaction.....68

Figure 34. Expansion dynamics: a) Vertical stretching and radial expulsion from the sheet edge b) Expansion of the sheet and gradual accumulation of liquid at the rim, the red arrow indicates the perturbations near the rim edge, c) A depiction of the rim with mass per unit arclength, denoted as m(t), attached to the sheet represents the sheet's outer edge with varying distribution of mass along its circumference. The sheet having a mass per unit arc length m (t), velocity u (r, t), and radius R(t) used for mass and momentum balances[55]. ..70

Figure 35. Overview of laser-induced fragmentation processes of iso-octane droplets; a) Complete atomization of the droplet, D_0= 0.2 mm, E_l = 20 mJ; b)

Ligament mediated breakup of iso-octane, D_0= 0.35 mm, E_l = 12 mJ; c) Sheet breakup through single hole formation within a droplet, D_0= 0.55 mm, E_l = 17 mJ; d) Sheet breakup of droplet through multiple holes merging, D_0= 0.54 mm, E_l = 20 mJ; e) Stable sheet collapse of a droplet, D_0= 0.54 mm, E_l = 17 mJ. 73

Figure 36. Maximum expansion of the droplet as a function of the Weber number (We). The solid line represents the cubic fit with a pre-factor of 0.8. The inset represents the variation of the propulsion speed as a function of laser energy. (The solid line is linearly fitted with a pre-factor of 0.6.) 77

Figure 37. Sheet breakup through nucleation of the holes in an iso-octane droplet: a) Single hole formation on the liquid sheet b) Multiple holes merging on the liquid sheet and its breakup. 79

Figure 38. The variation in diameter of pre-holes and holes over time corresponds to multiple instances of pre-holes and holes. The solid lines are linear fits.. 80

Figure 39. Initial fragmentation of n-hexane droplet showing a vertical expansion of the droplet concerning laser pulse focus position (a-e). Initial narrow opening for (a) to wide opening for (e) at the proximal side of the droplet, see at t = 10 µs. f) Reverse direction fragmentation of the droplet. g) Graphical representation of the laser pulse focus position inside the droplet. h) Stable sheet breakup of the droplet i) Probability density and normalized secondary droplet size distribution of n-hexane droplet depicted in 'e'. j) Comparison of probability density function for images a-e. 82

Figure 40. The initial ejection of the fragments and shear layer formation in the stretching liquid sheet. a) & d): - Shear layer formation; b) & e): - Vortex ring formation around the ejecting drops; c) Initial ejection of the drops. 84

Figure 41. The fragments impacting the liquid sheet membrane: a) capillary waves on the surface We = 0.5 b) Rupture of the membrane We = 4.3. 85

Figure 42. Liquid jet ejection and surface/capillary wave propagation from the liquid sheet surface. The blue arrow shows the liquid jet ejected from the sheet and the red arrow shows the surface/capillary waves travel on the sheet surface. 87

Figure 43. Ligament breaking under the RP instability. 89

Figure 44. Laser-induced evaporation of CNC droplet of D_0= 1.65 mm at 5 W and 5 % concentration. 94

Figure 45. Laser-induced evaporation of CNC droplets at different concentrations and laser energy. a) 0.5 %; b) 1 %; c) 2.5%; d) 5%; e) 0 W; f) 2.5 W; g) 5 W; h) SEM images of the end sample after the evaporation. 96

Figure 46. Laser-induced evaporation of CMC droplet of D_0= 1.61 mm at 5 W and 5 % concentration. 98

Figure 47. Laser-induced evaporation of CMC droplet at 0 W and 5 W laser power. 99

Figure 48. Laser-induced evaporation of Silica droplet of D_0= 1.61 mm at 5 W laser energy. 100

Figure 49. Laser-induced evaporation of Silica droplet of D_0= 1.61 mm at 0 W and 5 W. 101

LIST OF TABLES

Table 1. Properties of water and biofuels used in this study[140–147]. 29

Table 2. Detailed description of regime map presented in the Figure 20[132]. 50

Table 3. Essential characteristics of the ligament and ejected secondary droplets for liquids[131]..... 62

NOMENCLATURE

2D	Three Dimensional
3D	Three Dimensional
CW	Continuous Wave
f	Focal Length
LIBS	Laser-Induced Breakdown Spectroscopy
LIB	Laser-Induced Breakdown
PBS	Polarizing Beam Splitter
Hz	hertz
kHz	killohertz
kg	killogram
fs	Femtosecond
ms	millisecond
ns	nanosecond
µs	microsecond
nm	nanometer
µm	micrometer/micron
mm	millimeter
cm	centimeter
µJ	microjoule
mJ	millijoule
mW	milliwatt
W	Watt
E_l	Laser energy
R_0	Onset droplet radius

D_0	Onset diameter of the droplet
D_b	Bubble diameter
D_s	Secondary droplet diameter
D_L	Ligament diameter
D_P	Diameter at prebreak up instant
D_{rim}	Rim diameter
t	Frame interval time
t_b	Ligament breakup time
τ_c	Capillary time
τ_{cL}	Capillary time of ligament
V_s	Secondary droplet size velocity
V_L	Ligament velocity
V	Propulsion speed
σ_l	Surface tension of the liquid
ρ_l	Density of the liquid
μ_l	Viscosity of the liquid
We	Weber number
r_1 & r_2	radii of two approaching bubbles
r_{max}	Maximum radius of the bubble
γ	fraction of the laser pulse energy converted to the bubble's energy
R_{eq}	Equivalent radius of the bubble
L_s	Length scale of the sheet
a_s	Acceleration of the sheet
P_i	Internal pressure/pressure inside the droplet
P_e	External pressure
P_a	Ambient pressure
b	Rim thickness

R_{max}	Maximum radius of the expanded sheet
u_T	Thermal speed of the expelled vapor
K_B	Boltzmann constant
E_{ab}	Absorbed laser energy
E_{th}	Threshold laser energy
T_b	Boiling point
M	Molecular mass
CNMs	Cellulose nanomaterials
CNFs	Cellulose Nanofibers
CNCs	Cellulose Nanocrystals
CMC	Carboxyl Methyl Cellulose
RT	Rayleigh Taylor
RP	Rayleigh Plateau
KH	Kelvin-Helmholtz

1. Introduction

1.1. Motivation and background

The process of liquid droplet breakup and its dynamics is a crucial phenomenon with widespread practical significance across numerous fields in both science and engineering. This process is characterized by the transformation of a large droplet into numerous smaller fragments of varying sizes. It typically involves the violent separation of the droplet into a polydisperse cloud of tiny droplets. At its core, droplet breakup can be triggered by several factors: surface instabilities within the droplet, relative velocity between the droplet and the surrounding environment, significant changes in the flow field, such as interactions with solid surfaces, exposure to shock waves, laser pulses, or collisions with other droplets. In essence, droplet breakup is a dynamic process influenced by various physical mechanisms. It plays a critical role in a diverse range of applications, including spray systems (combustion devices, power plants, inkjet printing, agriculture, drying, and cooling), biomedical engineering (drug delivery, medical imaging, microsurgery), environmental science (aerosol dynamics, climate, air quality monitor), manufacturing (cleaning). Thus, understanding its intricacies is vital for various scientific and industrial applications.

Over the past several decades, Advances in laser diagnostics and mathematical modeling have propelled research in spray analysis and combustion processes. Laser-induced atomization and evaporation are pivotal in diverse applications due to their precision and controllability. In medical fields, they enable targeted drug delivery through aerosol generation and precise tissue ablation. In industrial processes, they facilitate advanced coating techniques, nanoparticle synthesis, and efficient fuel injection systems. Environmental monitoring benefits from laser-induced evaporation for detecting pollutants in aerosols, while in scientific research, it aids in studying droplet dynamics and heat transfer phenomena. The ability to achieve high spatial and temporal resolution makes laser-induced methods invaluable for optimizing processes across these fields. Atomization methods involve several fundamental processes, including the formation of a jet or sheet and the progression of small disturbances that eventually result in disintegration into

ligaments and drops. These processes are discussed in detail in the following sections.

1.2. Droplet Atomization/Fragmentation

Lefebvre A. H.[1] introduced "effervescent" or "aerated liquid" atomization technique, in the late eighties. This method involves dispersing a small amount of gas within the liquid to be atomized while pressurizing the mixture before injecting it into a low-pressure chamber. Rapid pressure drops cause gas bubbles to expand, breaking liquid into smaller droplets compared to traditional shear methods. High-pressure atomizers rely on liquid's kinetic energy, while twin-fluid atomizers use high-velocity air for interaction[1–3]. The droplet atomization/fragmentation process depends on formation of liquid sheets, shells, holes, jets, and ligaments, which ultimately break into stable fragments and droplets. Liquid sheet atomization is complex as multiple mechanisms may be at play. The significance of each mechanism varies across different flow regimes, influenced by factors like sheet properties, velocity, turbulence, and ambient air conditions. The thin sheet is formed and eventually breaks through the nucleation of holes[4] or impact of small drops[5,6] or instabilities on the sheet. The impact of fine droplets of another liquid induces the nucleation of holes due to localized Marangoni stresses[7,8]. Hole formation in a liquid film can also result from inertial instability, such as when the film is violently accelerated perpendicular to its plane. Regardless of the specific hole piercing mechanism, the process involves three main steps: the synchronous nucleation of holes across the sheet, the growth of these holes leading to the formation of a web of ligaments from the rims, and the subsequent breakup of this ligament web into a collection of droplets.

Droplet impacts on both solid and liquid surfaces, along with laser impact on droplets play a pivotal role in a wide array of applications. These include ink-jet printing, rapid cooling of hot surfaces such as turbine blades and rolls in steel production, as well as processes like annealing and quenching in metalworking. Droplet impact also affects fire suppression systems, internal combustion engines, incinerators, spray painting, plasma spraying, and agricultural crop spraying. Understanding and optimizing droplet-surface interactions are crucial for enhancing efficiency and performance across these diverse applications[9–18]. The

result of drop impact is influenced by several factors, including the velocity and angle of impact, drop size, liquid properties (density, viscosity, and viscoelasticity), surface or interfacial tension, solid surface roughness and wettability, non-Newtonian effects for complex fluids, as well as non-isothermal effects such as solidification and evaporation, and the potential for air entrapment.

Droplet impact on solid surfaces involves a dynamic and complex phenomenon such as deformation, spreading, and sometimes fragmentation or rebound, influenced by factors such as droplet velocity, surface roughness, and surface energy. Rioboo *et. al.* (2001)[10] reported the six possible outcomes after the droplet impact on the solid surface, includes deposition, prompt splash, corona splash, receding breakup, partial rebound and complete rebound. In 1908, Worthington[9] conducted one of the earliest systematic investigations in impact of liquid droplet and solid ball in liquid pool. It has revealed diverse phenomena like craters, Worthington jets, crown formation, and bubble entrapment. Prosperetti & Oguz (1993)[19] and Rein (1993)[20] highlighted moderate-velocity impacts (1–30 m/s) creating hemispherical craters in liquid pools.

The impact on droplets by laser pulses has garnered significant attention due to its wide-ranging applications in various scientific, industrial, and technological fields. When a focused laser beam impacts a droplet, it rapidly heats a thin layer on the droplet's surface, causing it to undergo a phase change. This sudden change generates a recoil pressure, which acts on the droplet and leads to its deformation and fragmentation[21]. Interestingly, the behavior of the droplet during this process shares similarities with what occurs when two droplets collide head-on or when a droplet impacts a dry surface, particularly in terms of how the droplet expands and breaks apart. However, when the laser pulses are of very high intensity and extremely short duration (sub-nanosecond), the dynamics of the process change significantly due to the compressibility of the liquid. In essence, the behavior of the droplet under such conditions deviates from what is observed with lower intensity or longer duration laser pulses, as the compressibility of the liquid introduces additional complexities to the process. Droplets are conventionally treated as transparent dielectrics when exposed to visible light. When a high-intensity laser pulse is focused within the droplets and exceeds the specific energy threshold (~

GW/cm^2), it triggers the optical breakdown of the liquid[22–25]. This breakdown manifests as a luminous spark accompanied by intense sound characterized by the generation of charged particles. A high temperature (~ order of 10^6 K) plasma is formed because of this breakdown, followed by a shock wave propagation[26–29]. Laser induced fragmentation plays a crucial role across various cutting-edge technologies and flow scenarios. In the automotive sector, high-speed droplet impact affects fuel combustion within engines, while in supersonic combustion engines, shock wave-induced breakup influences liquid atomization. Similarly, in semiconductor manufacturing, advanced techniques like extreme ultraviolet nanolithography rely on laser-induced droplet fragmentation to reduce microchip size.

1.3. Droplet Evaporation

While atomization and sprays typically are not directly associated with evaporation processes, in many cases, atomization aims to increase liquid surface area, thus accelerating evaporation rates. Particularly in combustion applications, there is a significant focus on understanding evaporation dynamics across various gas pressures and temperatures, both in steady and unsteady states. Introducing the concept of an effective evaporation constant[30] has greatly simplified the calculation of evaporation rates and droplet lifetimes for liquid hydrocarbon fuels. As droplets move through the combustion chamber, their size and composition change, influencing dynamic behavior and gasified fuel distribution. Droplet evaporation in sprays is affected by factors like gas flow convection and droplet interactions. Understanding these processes is crucial for fuel spray modeling. Studying single droplet evaporation is necessary for grasping basic multicomponent droplet evaporation.

- **Cellulose Nanomaterial (CNM):**

The oil and gas industry, in response to increasing global fossil fuel consumption and sustainability concerns, is turning to cellulose nanomaterials (CNMs) for innovative and eco-friendly solutions. CNMs[31], including cellulose nanofibers (CNFs), cellulose nanocrystals (CNCs), and bacterial cellulose (BC), offer promise due to their abundance, cost-effectiveness, renewability, and exceptional

properties. Recent focus has also been on cellulosic nanomaterials, such as nano fibrillated, nanocrystalline, and bacterial celluloses, which exhibit unique properties like nanoscale dimensions and high strength. CNCs, derived from various cellulose sources through acid hydrolysis, are firm, rod-shaped particles with sizes in the sub-micron range. Their properties are influenced by the cellulose source and hydrolysis conditions[31–34]. Evaporating aqueous CNC suspensions form iridescent chiral nematic films with reflection colors based on the chiral pitch. However, controlling the pitch and understanding CNC liquid crystalline traits and self-assembly for optical regulation remain underexplored, including the effects of geometric constraints.

1.4. Summary

Despite extensive research on laser-matter interactions, including fragmentation and shock dynamics, there remains significant scope for investigating laser-induced opto-hydrodynamics within single and multicomponent liquid droplets. Utilizing single nanosecond to multiple femtosecond laser pulses allows the study of phenomena such as deformation, expansion, plasma formation, shock wave dynamics, bubble dynamics, and breakup mechanisms. A key advantage of laser-induced breakdown is the precise energy deposition within droplets. Combining acoustic levitation with laser-induced fragmentation enables completely non-intrusive droplet manipulation. This study aims to experimentally investigate the distinct atomization and breakup mechanisms of contact-free single-component liquid droplets and biofuel-based multi-component droplets using nanosecond and femtosecond laser pulses.

There are a few questions whose understanding is still unclear, and we aim to address them through this study:

1. How do laser energy and droplet properties change the breakup mechanisms of single and multicomponent liquid droplets?
2. How do single and multiple laser pulses affect the dynamics of droplet deformation and fragmentation?
3. What is the role of microbubble generation inside droplets that beneficial in various scientific and industrial applications?
4. How do instabilities affect the ligament formation and the size distribution of secondary droplets?

5. What are the effects of laser heating on the structural and thermal properties of cellulose nanomaterials?

1.5. A guide through the thesis

This thesis focuses on investigating the interaction dynamics between laser pulses and liquid droplets, with particular attention given to exploiting the laser pulse energies and pulse sequences.

Chapter two provides an in-depth review of the relevant literature pertaining to the study, as well as an overview of the methodologies employed. The chapter delves into the intricate interactions between lasers and matter across various contexts.

In **Chapter three**, we detail the experimental setup and methodology employed for this study. This chapter gives details of laser setup, acoustic levitation, and fuel preparation.

In **Chapter four**, we explore the fluid dynamic deformation and fragmentation of diesel, RME, and water droplets through the application of focused femtosecond laser pulses. Utilizing multiple pulses, we delve into the examination of bubble dynamics, coalescence, and breakup mechanisms at varying energy levels.

Chapter five delves into the investigation of fluid dynamic deformation and fragmentation of single and multicomponent biofuel droplets. The study aims to elucidate the mechanisms underlying the breakup of the droplets.

Chapter six focuses on investigating the formation of laser-induced plasma and the dynamics of shock waves induced by nanosecond laser pulses with a wavelength of 266 nm. The study sheds light on the expansion dynamics, shear layer formation, various fragmentation processes in droplets of iso-octane and n-hexane.

In **Chapter seven**, we study the laser induced evaporation of the cellulose nanomaterials such Cellulose Nanocrystals (CNCs), Carboxyl Methyl Cellulose (CMC) and silica droplets.

2. Literature Review

2.1. Laser matter interactions

Lasers possess distinctive energy attributes, including spectral purity, spatial and temporal coherence, and high intensity. Their interaction with matter results in reflection, scattering, absorption, or transmission, contingent upon material properties such as physical, chemical, and optical attributes, as well as laser parameters. Key factors influencing laser-matter interaction encompass laser energy, wavelength, spatial and temporal coherence, exposure time, and pulse duration, enabling precise focusing at specific points. When directed through matter, lasers can induce processes such as ionization, excitation, and scattering, offering invaluable insights into the properties of various materials. Various types of laser-matter interactions have been harnessed for diverse applications.

When a light ray interacts with a liquid droplet, it imparts both energy and momentum, leading to scattering and absorption of light. This change in momentum results in a force exerted on the droplet. This force can counteract the droplet's weight, allowing for its levitation and stabilization within a laser beam. Debye[35] provided an expression for the radiation force acting on a transparent particle based on Maxwell's equations, while Roosen[36] determined the forces acting on a droplet in a laser beam with a Gaussian intensity distribution using an approach grounded in geometrical optics. These studies contribute to our understanding of how light can be utilized to manipulate and control droplets in various applications. The force acting on the droplet can be divided into two components: one parallel and the other perpendicular to the axis of the laser beam. In the case of transparent droplets, the force perpendicular to the axis always points toward the center of the laser beam and disappears when the droplet is positioned on the axis. This stabilization on the axis occurs due to this phenomenon. Conversely, for fully reflecting spheres, this component is directed away from the axis, rendering the position on the axis unstable.

Laser interaction in liquid environments presents distinctive traits across various technical fields. Short-pulsed laser irradiation triggers the explosive vaporization of liquids, a phenomenon harnessed for laser cleaning to eliminate

microcontaminants (Park *et al.*, 1994)[37] and in medical laser surgery[38–41]. Efforts have been made to gain a deeper understanding of superheated liquids and transitions from liquid to vapor, aiming to enhance control in relevant applications. Monitoring the transient evolution of bubble nucleation and phase change initiation has been facilitated by employing optical reflectance and scattering probes simultaneously (Yavas *et al.*, 1994)[42]. Numerical heat-conduction calculations indicate that the solid surface can reach temperatures significantly above its normal level. Real-time monitoring of surface temperature during laser-induced vaporization is crucial, as it plays a key role in heterogeneous nucleation. The kinetics and dynamics of heterogeneous bubble nucleation are particular research interests[43–45]. The interaction of short-pulsed laser light with liquids generates increased pressure[46]. This efficient conversion of laser energy into pressure finds application in technical and medical domains, including laser cleaning for surface contaminant removal, laser tissue ablation, corneal sculpturing (Vogel *et al.*, 1990)[38], and gallstone fragmentation (Teng *et al.*, 1987)[47]. Moreover, it finds extensive applications in surface treatment for metals and nondestructive material testing. The amplification of pressure within a liquid or at its interface with another medium stems from plasma formation, bubble cavitation, and rapid evaporation. Plasma formation typically occurs under high-intensity laser irradiation, associated with processes like ablation or optical breakdown. The collapse of bubbles generates a potent pressure impulse, as elucidated by Rayleigh (1917)[48]. High-speed photography has revealed that cavitation bubbles near a solid boundary induce the formation of liquid jets (Vogel *et al.*, 1989)[49], which are accountable for cavitation damage. Numerous technical applications rely on pressure generated through implosive bubble collapse, including ultrasonic cleaning. In the context of liquid film ablation by short-pulsed lasers, pressure generation is attributed to rapid bubble expansion due to instantaneous heating (Do *et al.*, 1993)[50].

2.2. Laser-Induced Breakdown (LIB)

Laser-induced breakdown (LIB), like naturally produced plasmas, takes two different forms: laser-induced thermal breakdown and optical breakdown. Laser-induced thermal breakdown occurs for long exposures to continuous wave (cw) or repetitively pulsed laser sources at high average power. It occurs primarily in materials which have a high linear absorption coefficient, i.e. those which are

opaque at the laser wavelength. The relatively slow absorption of energy from the laser produces heating of the medium, followed by melting, vaporization, and collisional ionization. Optical breakdown occurs primarily for short pulse exposures in the microsecond to femtosecond time regime. Here, the short pulse interaction time does not allow breakdown by linear absorption or direct heating. In this regime, the high peak powers and irradiances characteristic of short pulses produce plasma formation through processes such as formation of an electron cascade and direct ionization of the medium by multiphoton absorption.

Various methods have been developed to investigate different phenomena associated with individual droplets, including fragmentation, deformation, expansion, bubble dynamics, cavitation, coalescence, and evaporation [29,51–55]. Laser-matter interaction, and in particular laser-induced breakdown (LIB), has emerged as a progressive technique for scrutinizing and analyzing these phenomena. The application of LIB within a single droplet has proven useful in exploring atomization processes, cleaning techniques, and biomedical applications. The nanosecond and/or femtosecond pulsed lasers or continuous laser such as CO_2 lasers or fiber lasers have been used to investigate LIB in droplets [56–65]. The breakup mechanisms associated with the deformation and fragmentation of the liquid droplet can be achieved by a focused laser pulse. This approach has been extensively used to study the mechanisms and various breakup patterns. The mechanism/process of LIB and its wide range of applications are depicted in the Figure 1. The detailed mechanisms of LIB and plasma formation are explained in the following sections.

2.1.1. Mechanisms of LIB

Laser-induced breakdown (LIB) can occur through two mechanisms: direct ionization of the medium via multiphoton absorption[66–70] or cascade ionization[70–72], also known as avalanche ionization. Both multiphoton and cascade breakdown can occur in solids, liquids, or gases. However, in plasmas within solids or liquids, the concept of “free electrons" differs from that in gas plasmas. In condensed media, electrons exist in bound states within molecules or lattice sites, as well as in quasi-free states where their kinetic energy allows movement through the lattice

without being trapped by localized potential wells. Cascade ionization breakdown occurs in two stages: (i) cascade initiation by creating seed electrons and (ii) cascade amplification to high free electron densities. Cascade initiation necessitates the presence of one or more free electrons at the onset of the pulse within the focal volume. In impure media, these "seed" electrons typically arise from impurity ionization due to thermal excitation, establishing an initial free electron density before the pulse. In pure media, seed electrons must be generated by ionizing a few molecules through multiphoton absorption. Multiphoton breakdown is a straightforward process where each electron is independently ionized by absorbing multiple photons simultaneously. It occurs rapidly and independent of impurities or collisions, making it applicable even in sparse media. However, it requires very high irradiances to become significant and is typically overshadowed by cascade breakdown, which is more common. Cascade breakdown dominates in long pulse and continuous wave exposures in condensed media and dense gases. In contrast, multiphoton breakdown becomes prevalent in the femtosecond pulse regime and in diffuse gases, where low collision rates inhibit cascade formation[24,26,73].

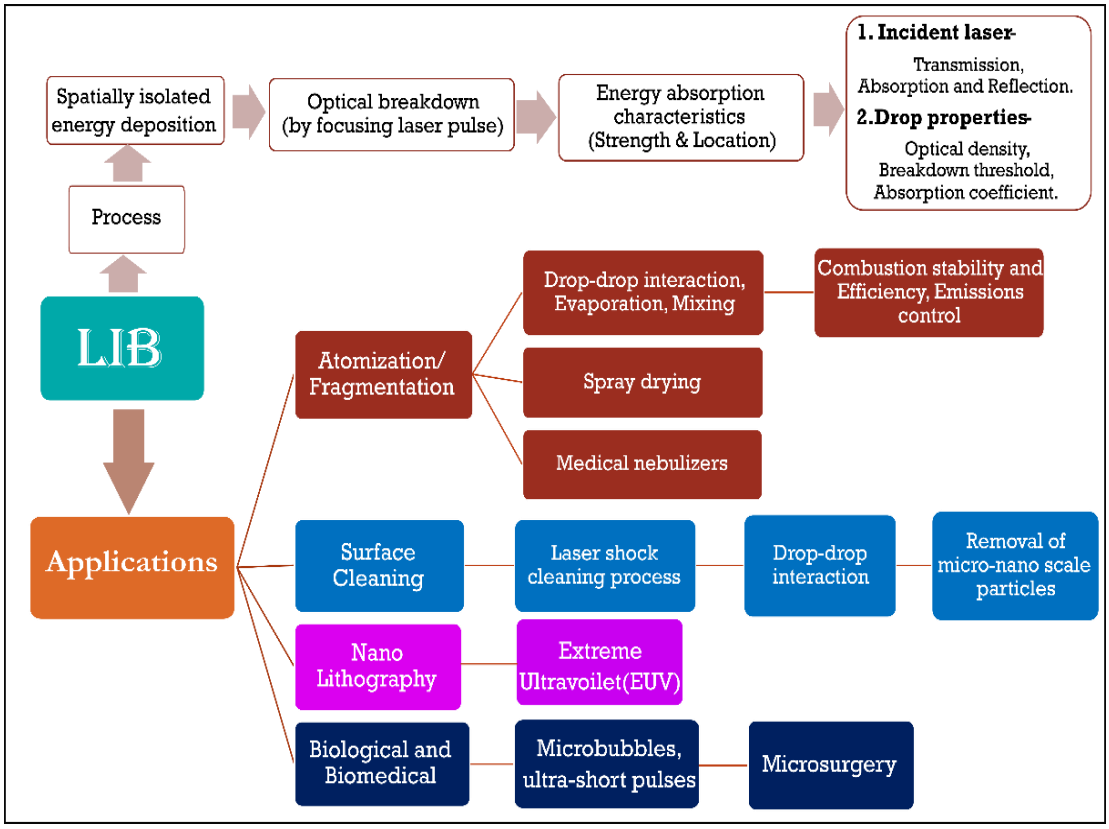

Figure 1. *Processes involved in LIB and its applications.*

Over the past five decades, there has been a continual trend of shortening laser pulse durations from microsecond range (1 μs = 10^{-6} sec) (the free-running regime) to nanosecond range (1 ns = 10^{-9} sec) (with Q-switching) to picosecond range (1 ps = 10^{-12} sec) and femtosecond range (1 fs = 10^{-15} sec) with the development of mode locking. A laser is categorized as a femtosecond laser if its pulse duration falls within the range of a few to several hundred femtoseconds. Ultra-short laser pulses, particularly femtosecond pulses, play a pivotal role in controlling the dynamics of LIB. Over the past three decades, the study of femtosecond pulse interaction with droplets has led to a diverse range of applications[28,74–82]. When a tightly focused femtosecond laser pulse interacts with condensed matter, it initiates optical breakdown or filamentation phenomena[76–78]. This intricate interaction entails several physical processes, including light absorption, nonlinear ionization, plasma formation, bubble generation, thermal conduction, ablation, and electron-photon collisions. The absorption of femtosecond laser light by the medium triggers a cascade of events, beginning with nonlinear ionization processes. This leads to the formation of plasma, a highly ionized state of matter, which further interacts with the surrounding environment. Concurrently, rapid heating induced by the laser pulse can result in the generation of bubbles within the medium, altering its physical properties. Thermal conduction plays a crucial role in distributing the absorbed laser energy within the medium, influencing the spatial and temporal evolution of the interaction. Ablation, the removal of material from the surface, occurs because of intense localized heating and subsequent vaporization. Additionally, electron-photon collisions contribute to the complex dynamics observed during femtosecond pulse interactions, further shaping the outcome of the process.

2.1.2. Plasma formation

For decades, researchers have been exploring the rapid formation of laser-induced plasma (LIP). A high-intensity laser pulse swiftly transfers energy to the target surface, causing instant absorption, ionization, and vaporization of the material. This process generates an extremely hot vapor plume, often referred to as a "plasma plume." The laser-induced plasma consists of three main regions: the core, Knudsen layer, and outer region. The core, nearest to the target surface, is the hottest and densest part, predominantly ionized due to high temperatures. Surrounding the core

is the Knudsen layer, where particles reach equilibrium velocity distribution within a few mean free paths. In the mid-region, ions and neutrals coexist due to ongoing ionization and recombination processes. The outer region is relatively colder, dominated by neutrals, potentially absorbing radiation from the core and mid-regions. Beyond lies a shock wave front resulting from the plasma's explosive expansion, preceding the plasma plume[83]. Plasmas exhibit significantly stronger absorption of visible radiation compared to transparent materials, primarily due to inverse bremsstrahlung absorption by free electrons within the plasma. The plasma generated from LIB can swiftly heat up under the laser beam, reaching temperatures around 10^4 K, resulting in visible plasma emission and plasma pressures ranging from 10^4 to 10^5 bar. These high temperatures and pressures cause plasma to expand rapidly at supersonic velocities, leading to the production of audible acoustic sound, shock waves, and cavitation effects.

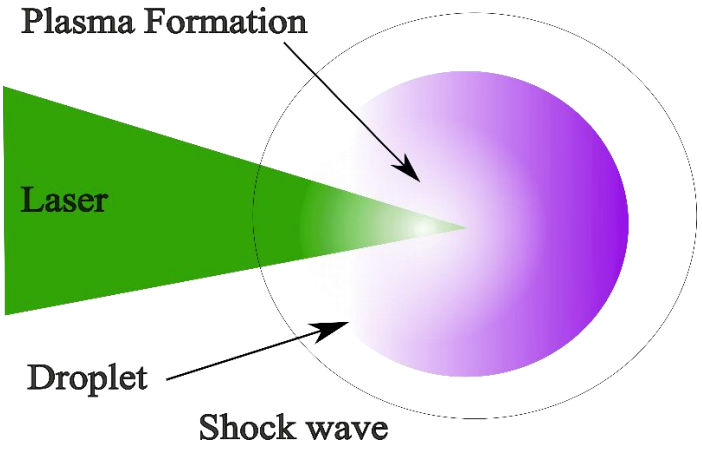

Figure 2. *Schematics of plasma formation and shock wave travel during laser droplet interaction.*

For nanosecond laser pulses with irradiances below 10^8 W/cm², thermal vaporization is the primary mechanism for plasma ignition. However, for picosecond laser pulses with irradiances ranging from 10^8 to 10^{13} W/cm², both thermal and non-thermal mechanisms contribute to plasma ignition. With femtosecond laser pulses at irradiances exceeding 10^{13} W/cm², the main mechanism for plasma ignition shifts to non-thermal processes, specifically Coulomb's explosion[83,84]. Figure 2 shows the laser induced plasma formation in the droplet along with the shock wave travel in the medium

LIP has garnered significant attention across various applications, including inertial confinement fusion, pulsed laser deposition in material science, and lithography[83–86]. Specifically, extreme ultraviolet (EUV) lithography stands out as a promising technology for next-generation semiconductor devices with resolutions below 5 nm. LPP has emerged as a preferred option for EUV light sources due to its high efficiency, scalability in power, and spatial flexibility around the plasma. In this setup, metal droplets serve as targets irradiated by pulsed lasers to generate hot dense plasma that emit EUV light[54,87]. A recent study by Zhenyu Zhao & Weizhong Li [88] reported the numerical simulation of the expansion of the laser induced plasma on the droplet surface. The initial plasma formation utilized a pressure inlet boundary condition, facilitating analysis of how ambient pressure impacts both the initial plasma and its subsequent adiabatic expansion on the droplet surface. This investigation encompassed the study of how ambient pressure affects the velocity and temperature distribution within plasma.

2.1.3. Shock wave generation

Laser-induced shock waves[89–97] can trigger various mechanisms leading to the development of instabilities and breakup of droplets. When a high-intensity laser pulse interacts with a droplet, it rapidly heats the surrounding medium, causing it to expand explosively. This sudden expansion generates a shock wave that propagates through the droplet, inducing significant mechanical stress and deformation. One mechanism by which shock waves contribute to droplet breakup is through the generation of surface instabilities. As the shock wave travels through the droplet, it can perturb the surface of droplet, leading to the formation of ripples or waves. These surface disturbances can grow and amplify due to the pressure gradients induced by the shock wave, eventually causing the droplet to fragment into smaller droplets. Additionally, shock waves can induce internal cavitation within the droplet. As the shock wave passes through the droplet, it creates regions of low pressure, causing the formation and collapse of cavitation bubbles within the liquid. These rapid bubble dynamics can impart significant mechanical forces on the droplet, further contributing to its fragmentation. The shock waves can also trigger acoustic streaming effects within the droplet, leading to complex flow patterns and shear forces[16,93,98]. These hydrodynamic instabilities can disrupt the

droplet's internal structure, promoting breakup into smaller droplets. Overall, the interaction of laser-induced shock waves with droplets can initiate a cascade of physical processes, including surface instabilities, cavitation, and acoustic streaming, all of which contribute to the breakup of the droplet into smaller fragments.

2.1.4. Bubble generation

The process of generating bubbles through the focusing of multiple laser pulses comprises several steps. When high-power laser radiation at the focal point exceeds the breakdown threshold (> 10^{12} W/cm^2)[82], it triggers the formation of free electrons due to multiphoton ionization and tunnel ionization. Consequently, the liquid undergoes rapid excitation, ionization, and dissociation into a high-temperature plasma (~ 10^4 K) within the focal region[28]. Subsequently, recombination processes occur, and the plasma is replaced by a vaporized fluid mass, which forms micro-bubbles [60,99]. The nature of bubble formation (single or multiple, spherical or non-spherical) depends on factors such as laser energy, focusing conditions, and the properties of the liquid medium [99–101]. Laser pulse-induced bubbles are of particular importance, as they play a crucial role in cellular microsurgery [100], removing thrombus (blood clot) from clogged arteries [39], and clearing bile duct stones through breakup and lithotripsy [41].

The generation of bubbles by launching the laser pulses in water [81,102–105] and employing diverse approaches has been investigated in numerous studies. Potemkin and Mareev [81] observed the evolution of multiple cavitation bubbles within a single filament stimulated by a femtosecond laser pulse in water. Laser-induced filamentation, characterized by the formation of thread-like structures due to self-focusing (by optical Kerr effect), played a pivotal role in this phenomenon. Expanding on this, Potemkin *et al.* [102] explored different regimes of filamentation and the associated dynamics of shock waves and micro-bubbles induced by filaments in water. They achieved this by employing various focusing techniques, including the introduction of aberrations, modifying laser parameters such as pulse energy, and manipulating the properties of the medium, such as its linear absorption characteristics. Jukna *et al.* [103,104] reported the significant impact of pulse duration on the shape and intensity of acoustic signals arising from the filamentation of

ultrashort terawatt laser pulses in water. These signals were closely linked to the mechanism of super filamentation in water. A study by Rao *et.al.*[60] reported femtosecond laser induced microbubble generation in the liquid pool. The study explores the dependency of bubble size, shape and population density on laser energy, number of laser pulses and the liquid medium. Koukouvinis *et al.*[106] examined the interaction of laser-induced bubble with free surface, comparing experimental findings and Computational Fluid Dynamics (CFD) simulations utilizing the Volume of Fluid (VOF) methodology. The simulations effectively predicted bubble expansion and collapse, aligning with both qualitative and quantitative observations. Rosselló *et al*. [90] investigated the laser-induced bubbles and jetting inside millimetric droplet. They reported on vapor bubble expansion within water droplets, acoustics secondary cavitation, and the formation of liquid jets near highly curved surfaces. Raman *et al.*[107] studied the dynamics between a laser-generated cavitation bubble and a submillimeter-sized water droplet submerged in silicone oil. The study revealed three distinct interaction phases: deformation, external emulsification, and internal emulsification. Notably, during bubble collapse, the droplet elongates towards the bubble, influenced by the bubble's flow sink effect. Nevertheless, most investigations into laser-assisted bubble dynamics have primarily focused on individual bubbles, particularly at low laser energy levels (< 200 μJ). It is crucial to recognize that laser-induced cavitation bubbles [27,90,107–109] play a pivotal role in laser-induced breakdown in liquids. Therefore, comprehending the hydrodynamics of multiple bubbles during the process is imperative. Equally significant is the examination of the interaction among micro-bubbles generated by temporally separated laser pulses. This interaction sheds light on how residual bubbles and their fragments from previous pulses interact with bubbles generated by subsequent pulses.

2.1.5. Breakup mechanisms and instabilities

The fragmentation of liquid is primarily attributed to the momentum disparity between the liquid and the surrounding gas. This discrepancy in momentum induces a shear instability on the interface between the liquid and gas, giving rise to the formation of wave structures. Subsequently, these liquid waves evolve into thin

sheets, which, under the influence of surface tension develop rims at their free ends[110]. These liquid rims experience transverse instabilities, leading to the formation of fingers that eventually break into ligaments and droplets[53,54,111,112]. Aerodynamic droplet fragmentation is classified into five distinct breakup modes: multimode breakup[97,113], vibrational[114], sheet thinning[115], catastrophic breakup[116], and bag breakup[117,118]. Some breakup occurs due to instabilities such as Rayleigh–Taylor (RT) and Rayleigh–Plateau (RP) when the edge of the radially expanding droplet fragments[7,14,53,119].

Another significant breakup mechanism involves the formation of holes within sheet preceding the development of ligaments. These holes undergo expansion, merging either with each other or with a retracting end rim, ultimately resulting in the rupture of the liquid sheet and formation of droplets[54,55,120]. This additional process underscores the complexity and variety of mechanisms at play during atomization. The rupture of the sheet through hole formation is reported in different investigations[121–123]. G.G. Agbaglah[124] revealed the dynamics of the merging of two holes and a single hole with a rim using three-dimensional simulations. Ling et al.[125] reported hole formation and subsequent liquid sheet breakup during atomization. A common outcome following hole collision involves the creation of a smooth or rough liquid bridge. This bridge, in turn, detaches into a ligament that either breaks into multiple smaller drops or collapses into a single large drop. The final outcome of the detached ligament depends on its aspect ratio and the associated Ohnesorge number [126–128]. Therefore, investigating the mechanisms leading to ligament formation in the context of hole collisions and understanding the characteristics of the resulting ligaments becomes important for atomization studies.

2.3. Single droplet Levitation

The disintegration of bulk liquid is observed during events such as raindrops splashing on solid surfaces or the fragmentation of raindrops into smaller droplets under external force. Both mechanisms contribute significantly to the dispersion and distribution of liquid particles in diverse environmental and industrial contexts. Single droplet study is used to understand important physical phenomena such as breakup, evaporation, liquid-matter interaction etc.

Droplet suspension techniques involve methods to suspend liquid droplets in a controlled manner, often without physical contact with any surface. Various techniques available offers unique advantages and is selected based on factors such as droplet size, composition, and the desired level of control and manipulation. These methods find applications in various fields including materials science, biology, chemistry, and physics, facilitating research and technological advancements in droplet-based systems and processes. Some common techniques are discussed below.

A **single moving droplet** refers to a liquid droplet that is in motion, typically within a controlled environment. This motion can be induced by various means, such as external forces like gravity, air currents, or applied fields, including electric, magnetic, or acoustic forces. A free-falling droplet refers to a liquid droplet falling through a medium, usually air, under gravity, enabling the study of droplet dynamics and properties through high-speed imaging and laser-based diagnostics. In contrast, aerodynamically suspended droplets are maintained aloft in a gas stream using aerodynamic forces, with controlled airflow and pressure creating low-pressure or turbulent regions for droplet suspension. This technique is commonly applied in spray drying, aerosol generation, and particle characterization, with airflow parameters precisely regulated for effective suspension. Droplet suspension with thin fibers utilizes surface tension and capillary action to hold liquid droplets along fine, thread-like fibers, creating a large surface area-to-volume ratio ideal for applications in materials science, biomedical engineering, and environmental monitoring. Electrostatic levitation suspends objects using electric fields, leveraging Coulomb's law for non-contact droplet manipulation, with uses in fluid dynamics and pharmaceutical research. Electromagnetic levitation relies on magnetic fields to counteract gravity, enabling precise control of droplets in containerless processing and extreme conditions. Optical levitation employs laser-induced optical forces to suspend and manipulate particles, aiding studies of colloidal systems, biological cells, and light-matter interactions. Acoustic levitation uses high-frequency sound waves to trap particles at pressure nodes, providing stable suspension for experimental analysis. It is detailed explained in the experiment and methodology section.

2.4. Scope and objective of the study

Although there have been numerous investigations on single and multi-component liquid droplets, comprehensive studies on the bubble dynamics and subsequent breakup characteristics of fuel droplets under focused single and multiple laser pulses are lacking in the literature. There is significant potential for exploring laser-induced opt-hydrodynamics in single and multicomponent liquid droplets. Our study addresses this gap by examining these specific dynamics in the acoustically levitated liquid droplets. This study represents the first systematic attempt to observe and analyze the entire sequence of events within a single droplet of fuel, encompassing bubble generation, growth, coalescence, rupture, droplet stretching, and eventual breakup. Experimental findings from single droplet experiments are interpreted through the application of fundamental physical principles and theoretical analyses pertaining to bubble dynamics and droplet breakup phenomena. Moreover, the laser's interaction with the droplet presents an opportunity to manipulate the liquid, offering potential advantages for various industrial applications.

Based on the literature survey and identification of gaps, we have organized the study into four main objectives.

I. To investigate fragmentation/breakup mechanisms using laser pulse in single and multicomponent fuel droplets.

II. To study the effect of nanosecond laser pulse interaction in acoustically levitated liquid droplets.

III. Bubble dynamics and atomization of liquid droplets using femtosecond laser pulses.

IV. Laser induced evaporation of suspended liquid droplets.

At the core of the study, high-speed shadowgraph imaging is used to capture the opto-hydrodynamics inside the droplet. In summary, this study is divided into three main parts: the first part focuses on bubble creation and dynamics, while the second part investigates the breakup of fuel droplets and finally laser induced evaporation of the cellulose nanomaterials.

3. Experimental setup and methodology

3.1. Experimental setup

The experimental setups to study laser pulse interaction with a single acoustically levitated droplet are described in this chapter. The laser setup, imaging system and acoustic levitation setup are explained in detail.

3.1.1. Laser setup

Three distinct laser configurations are employed in the study. Two Nd: YAG nanosecond lasers with wavelengths of 266 nm and 532 nm and one femtosecond laser operating at a wavelength of 775 nm, are used. The details of the laser setup are comprehensively explained in the subsequent sections. These lasers offer different temporal and spectral characteristics, allowing us to explore a wide range of processes and interactions. A detailed overview of the laser setup in subsequent sections provides insight into the experimental methodology employed, including beam focusing, energy calibration, and control parameters.

3.1.1.1. Nanosecond laser of 266 nm wavelength

The schematic of the experimental arrangement for the UV laser-induced deformation and fragmentation is illustrated in Figure 3. The laser arrangement describes a laser beam from a Q-switched Nd: YAG laser (Spectra-Physics Quanta Ray) generating a fourth harmonic wavelength of 266 nm, pulse duration of 5 ns, repetition rate of 10 Hz, maximum energy per pulse 20 mJ, and laser beam diameter of 10 mm. The laser energy is measured close to the laser exit port using an energy meter (Nova- II OPHIR). The beam size near the laser focus varies with laser energy and is measured using laser burn paper. Throughout the experiments, the diameters of laser focus spots (in tens of microns) are much smaller than the size of the droplets.

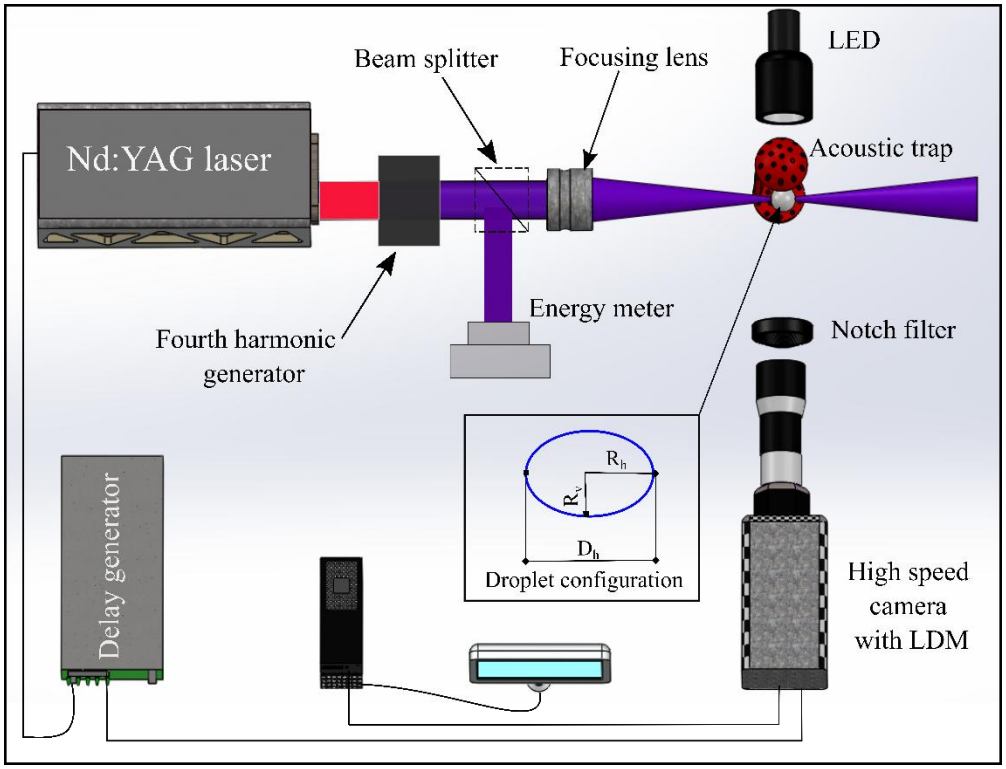

Figure 3. *Schematic top view of the experimental setup for laser-induced fragmentation of levitated droplets. The inset represents the droplet configuration used for analysis.*

3.1.1.2. Nanosecond laser of 532 nm wavelength

Figure 4 shows the experimental setup that consists of nanosecond laser system to fragment a levitated droplet, an acoustic levitator, and optical imaging systems. A Q-switched Nd: YAG laser (Quantel Brilliant B) of 532 nm wavelength, pulse duration 5 ns, repetition rate 20 Hz, maximum energy per pulse 350 mJ, and laser beam diameter of 4 mm is used in the present work. The laser energy was measured close to the laser exit port using an energy meter (Nova- II OPHIR). The beam size near the laser focus varies with laser energy and was measured using laser burn paper. The spot radius at the focus changed from 25 µm at 0.2 mJ to 80 µm at 6 mJ. Throughout the experiments, the diameters of the laser focus spot (of the order of tens of microns), were much smaller than the size of the droplets.

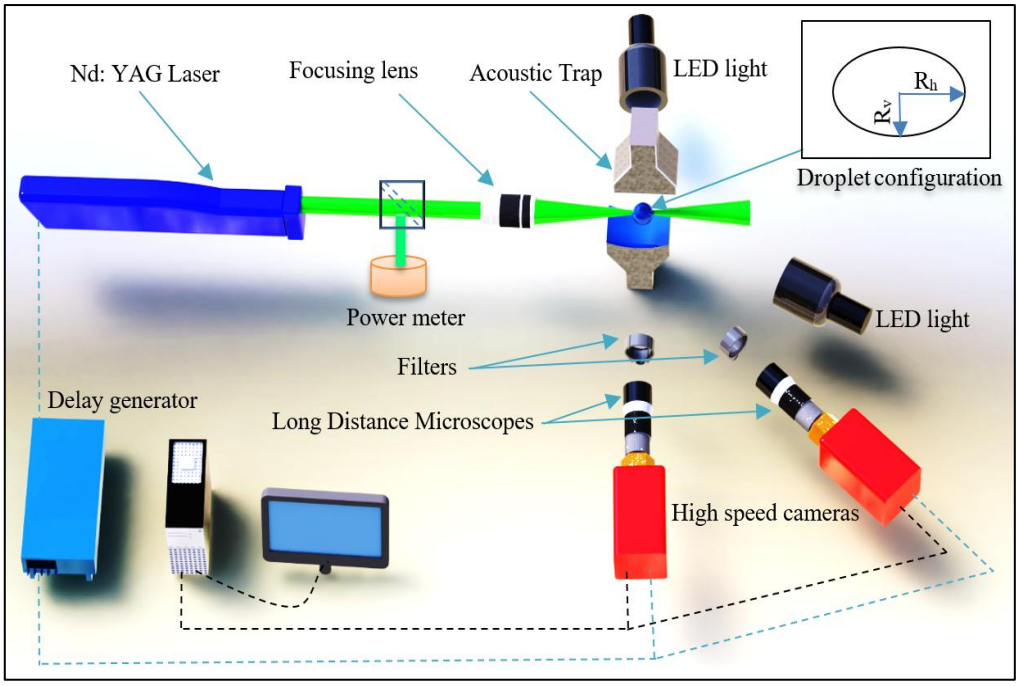

Figure 4. *Experimental setup for nanosecond laser-induced fragmentation of levitated droplet* [129].

3.1.1.3. Femtosecond laser of 755 nm wavelength

The schematic of experimental setup pictured in Figure 5 shows the Femtosecond laser induced droplet dynamics in acoustic levitator. The CPA series femtosecond laser is compact, integrated Ti: Sapphire amplified laser system and is comprised of Laser head, ORC 1000-power supply, Dt-505 Pockel cell driver and temperature stabilization unit. The CPA series laser head contains the SErF fiber laser, Pulse stretcher and diode laser in the bottom level and Regenerative amplifier, ORC-1000 frequency-doubled Nd: YAG pump laser and pulse compressor in the top level. The laser output used in this study has a beam diameter of 10 mm, wavelength of 775 nm, 150fs pulse duration, and 1 kHz repetition rate. The laser energy is controlled using quarter Wave plate (λ/4, 830nm) and Polarizing Beam Splitter (PBS) combination shown in Figure 5. A quarter-wave plate is designed such that the phase shift created between the fast and slow axes is a quarter wavelength (λ/4). If the input beam is linearly polarized with the polarization plane aligned at 45° to the wave plate's fast or slow axis, then the output beam will be circularly polarized. If the linearly polarized beam is aligned at an angle other than 45°, then the output will be elliptically polarized. The laser energy used in this study varies from 1 mw

to 1050 mw and it is measured after wave plate using FS power meter (FIELDMASTER, COHERENT, LM-10 HTD). The maximum energy per pulse is 1050 µJ with an average power of 1.05 W. The laser beam waist size at focus changes with laser energy and it is smaller than droplet size for all experiments.

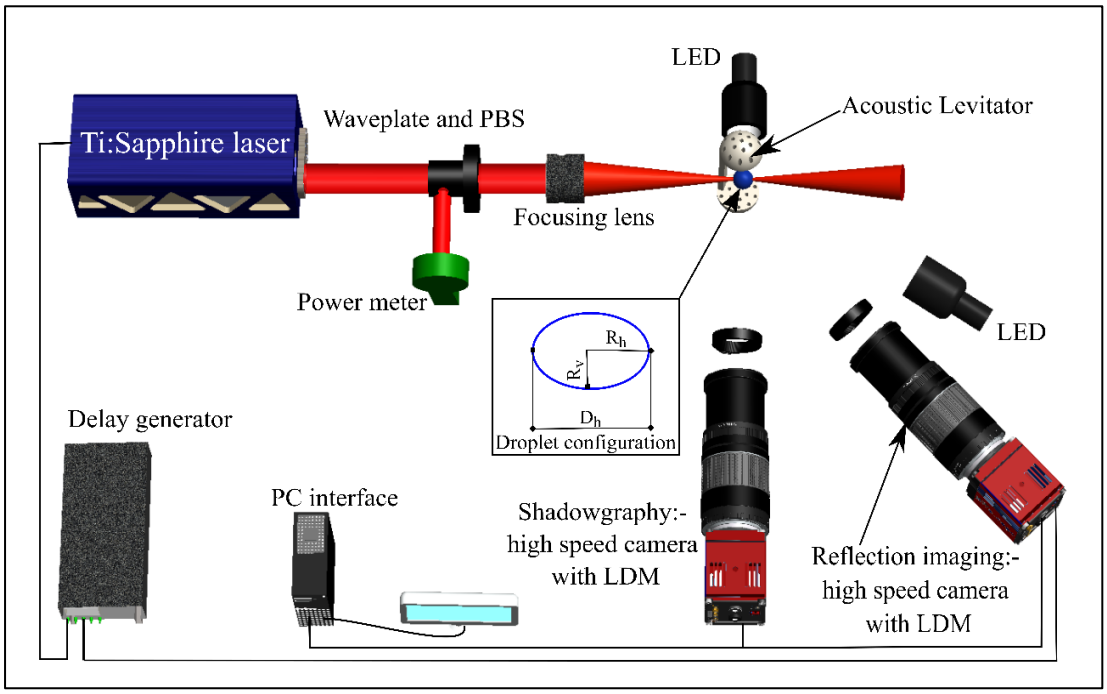

Figure 5. *Experimental setup for femtosecond laser-induced fragmentation of acoustically levitated droplet* [130].

3.1.2. Imaging system

The dynamics of droplet fragmentation are recorded using two identical high-speed cameras, Phantom Miro LAB310 from Vision Research, as illustrated in Figure 4 and Figure 5. One camera is operated at 11000 frames per second (fps) with a resolution of 512×512 and an exposure time of 18 µs, while the second camera recorded at 5400 fps with a resolution of 768 x 768 and an exposure time of 140 µs. Both cameras are equipped with long-distance microscopes (Infinity Model K2 DistaMax). The pixel resolution for shadowgraphy is 6.75 µm/pixel, and for reflection imaging, it is 11.0 µm/pixel. Illumination is provided by two white light LEDs (Thorlabs), with one camera capturing the reflection of LED light from the droplet and the other recording the backlighting shadow of the droplet. Additionally, an optical measurement unit, shown in Figure 5, contained a high-speed camera (Phantom v1210) with a microscopic objective lens (Navitor 12x

zoom), illuminated by an LED fiber optic lamp (Thorlabs HPlS200). The shadowgraph of droplet dynamics is captured at 35 kfps and 190 kfps with a resolution of 10 µm/pixel.

3.1.3. Optics

The primary optical components utilized in the setup include a focusing lens to concentrate the laser beam, notch filters to block laser light and prevent camera saturation, and a beam splitter. A focusing lens (high-power doublet Achromat, 532 nm wavelength, and focal length f = 100 mm) is employed to focus the laser beam inside the droplet, as depicted in Figure 4. For a 266 nm wavelength, a high-power doublet achromat lens with a focal length of 150 mm is used. In the case of a femtosecond laser, precise focusing of the laser beam at the droplet's center is achieved using a near-infrared high-power doublet with a focal length of 100 mm.

3.2. Laser induced evaporation of the droplets

Figure 6 and Figure 7 illustrate the experimental setups employed for the investigation of droplet evaporation dynamics. The setup comprises: an Ytterbium linearly polarized continuous laser with wavelength of 1064 nm and beam diameter of 6 mm, an acoustic levitator, and a high-speed camera equipped with a zoom lens. The experimental study focuses on three types of samples: cellulose nanocrystals (CNCs), Carboxymethyl cellulose (CMC), and silica droplets. For each sample, experiments are conducted using four different concentrations of CNCs (0.5%, 1.0%, 2.5%, and 5.0%) at varying laser energy levels (0 W, 2.5 W, and 5 W). Aqueous suspensions are prepared using distilled water as solvent. The setup allows controlled investigation of the evaporation behaviour of droplets containing different materials under various experimental conditions. A high-speed camera, coupled with the zoom lens (256 X 256 with 9.5 µm/pixel resolution, exposure of 2 µs), facilitates high-resolution images of the droplet evaporation phenomena.

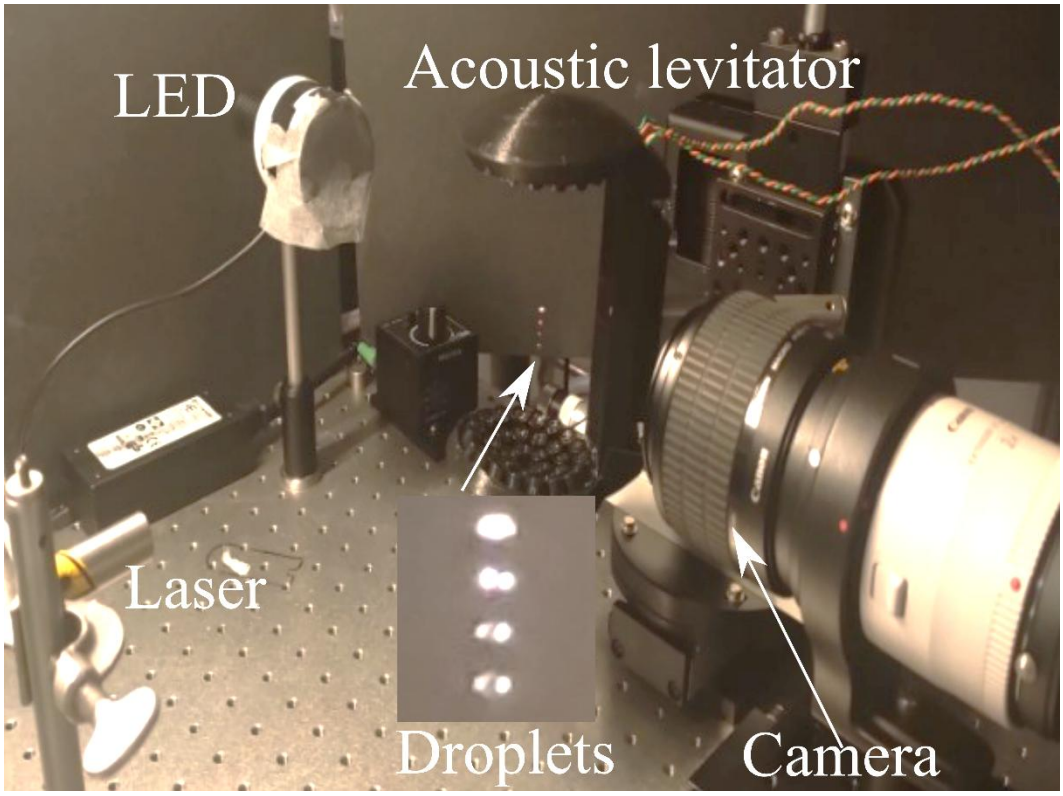

Figure 6. *Experimental setup for laser-induced evaporation of liquid droplets.*

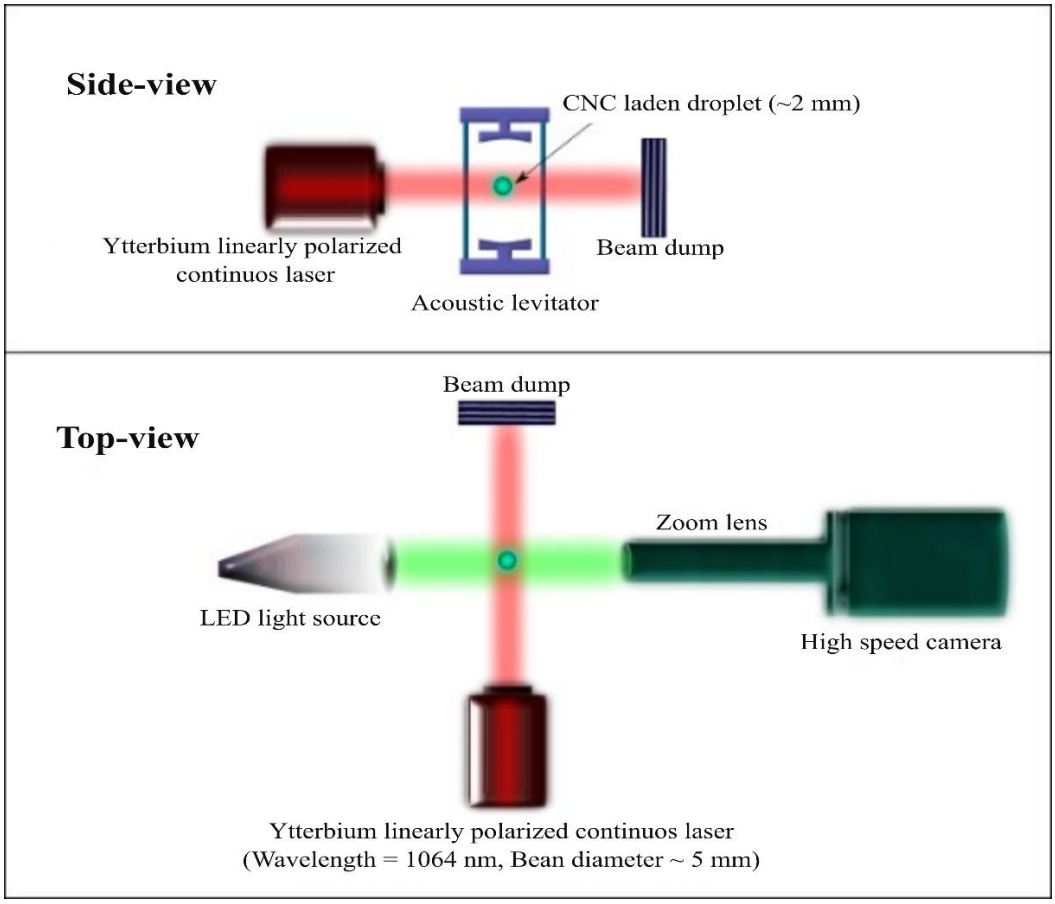

Figure 7. *Schematic setup for laser-induced evaporation studies of liquid droplets.*

3.3. Acoustic levitation

Acoustic levitation[131,132] employs forces of acoustic radiation to counteract gravity force, allowing objects to seemingly float in mid-air. The phenomenon was first demonstrated almost a century ago, it remained largely constrained for a long time to objects much tinier than the acoustic wavelength. The recent advances in acoustic levitation have expanded its capabilities. Now, objects can be suspended, rotated and translated is space using acoustic forces. The advantage of this technique is contactless method, avoids solid wall boundary around sample and not dependent on any physical properties of the sample[132], [131]. A standing wave is formed between emitter and reflector which has nodes (minimum pressure zone) and antinodes (maximum pressure zone). This is achieved by maintaining the distance of emitter and reflector to multiple of half of the sound wavelength[131]. Once the droplet is suspended, its axial position, size and shape affects the measurements performed. Hence, the stability of the droplet in the acoustic levitator is important as unstable droplet pose difficulty for laser beam focusing at the center of drop[133,134]. This is done by increasing the operational voltage of acoustic levitator. Also, the higher voltage can lead to shattering of the droplet when placed at node[135]. Apart from stability, the shape of the droplet changes with respect to forces acting on it. The action of acoustic radiation pressure and suction stress (due to Bernoulli Effect from streaming flow) droplet flattens. The reverse of this, the force due to surface tension and internal pressure opposes flattening. The relationship of these forces is defined by dimensionless entity, acoustic bond number (relates the acoustic effect to surface tension effect)[131,136]. A notable development is the use of "acoustic tweezers," which are capable of precisely manipulating small particles or biological samples. These devices use focused sound beams to trap and move objects with high precision.

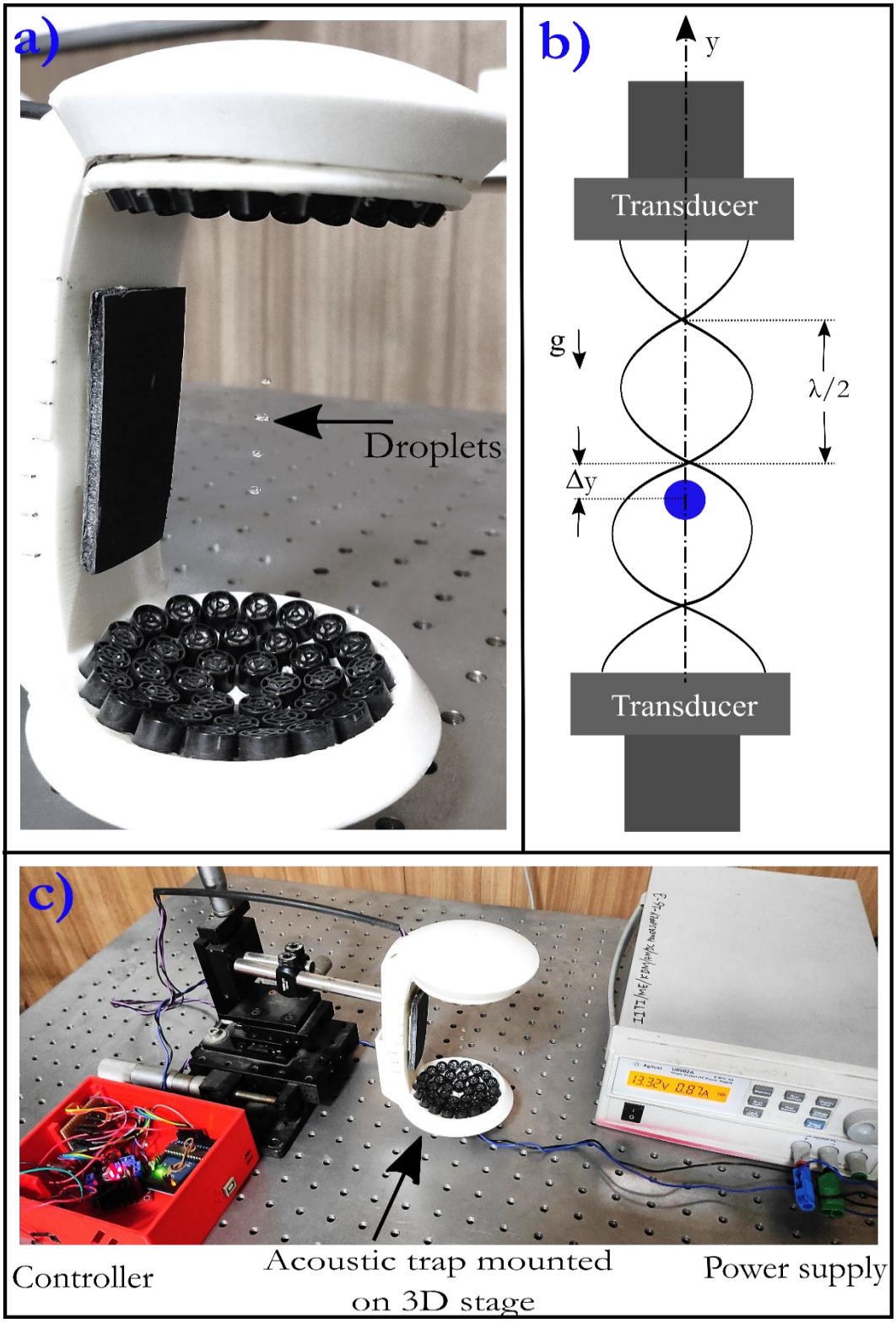

Figure 8. *Acoustic levitator demonstration: a) Actual droplets trapped in the Acoustic trap b) Acoustic levitation of a small droplet at the pressure node of a plane standing wave formed between transducer c) Experimental setup for the droplet levitation.*

3.4. Droplet generation and levitation system

The acoustic levitation works on the principle of generating a standing wave between the emitter and reflector (see Figure 3, Figure 4, & Figure 5). The nodes (minimum pressure zone) and antinodes (maximum pressure zone) of the standing wave are used to levitate solids and liquids in mid-air [132,133]. The various nodes are controlled by maintaining the distance of the emitter and reflector to a multiple of half of the sound wavelength. We used a home-built 3D-printed single-axis acoustic levitator that consisted of 72 transducers of 10 mm diameter each, operating at a resonance frequency of 40 kHz [133]. Transducers were arranged circumferentially over a pair of semi-spherical plastic supports. The reflector and transmitter pair were separated by 12.4 cm. The control system for the transducers consists of an Arduino nano board generated square wave signal, which was amplified using a L297N Dual H-Bridge stepper motor drive. The droplet was moved vertically by adjusting the phase of one of the driver's channels. The stable droplet in the acoustic levitator was necessary for the laser beam focusing at the center of the droplet [133,134,136]. The droplets were produced using a microliter syringe and needle arrangement at ambient conditions (approximately 293 K and 50% relative humidity). These droplets were placed close to the pressure nodes such that the acoustic pressure balances the gravity force to levitate a stable droplet. The experiments were conducted in the lab at room temperature and atmospheric pressure conditions. The stability and shape of the droplet were adjusted by changing the input voltage. By lowering the voltage, the shape of the droplet was controlled near spherical, i.e., the surface tension was dominating the acoustic force. The acoustic force increased above the surface tension by increasing the voltage, which changed the spherical drop to an elliptical shape. Once the droplet was stable in the acoustic trap, the laser pulse was aimed to focus at the center of the droplet. In the present work, owing to the moderate surface tension and viscosity of the liquids, all the droplets were stable and spherical at the pressure node of the acoustic levitator. The equivalent onset radius of the droplet under levitation is defined as $R_o = ({R_h}^2 \times R_v)^{1/3}$, where R_h and R_v are the horizontal and vertical radius of the droplet, respectively (see droplet configuration in the inset of Figure

3, Figure 4, & Figure 5) [122,137]. Thus, $D_o = 2R_o$ represents the onset diameter of the droplet.

3.5. Image processing and data extraction

The shadow and reflection images of droplets, captured from the experimental setup, underwent post-processing and analysis utilizing MATLAB and ImageJ software. In MATLAB, various image processing techniques, such as segmentation, edge detection, thresholding, and morphological operations, are applied to isolate and enhance features of interest within the images. This included separating droplets from the background, detecting boundaries, and refining segmented regions. Subsequently, in ImageJ, additional analysis is conducted, encompassing measurement, quantification, particle analysis, and visualization. Measurement tools are utilized to extract droplet parameters like diameter and area, velocity, acceleration. Visualization tools facilitated the creation of histograms and scatter plots to interpret the results.

3.6. Fuel preparation and its properties

In the present study, various fuels including water, diesel, n-hexane, iso-octane, ethanol, Rapeseed Methyl Ester (RME), as well as emulsions of RME and ethanol, are used. To create the RME-ethanol emulsions, RME and ethanol are mixed in different proportions using a magnetic stirrer. To prevent phase separation of RME and ethanol, 2% (v/v) of surfactant SPAN 80 (Sorbitan Monooleate) is added. The properties of these emulsions are estimated using the mixture rule. Two emulsions of RME and ethanol are prepared: RE30 (70% RME and 30% ethanol), and RE50 (50% RME and 50% ethanol). By systematically varying the proportions of RME and ethanol and employing a surfactant phase separation could be prevented. Table 1 provides a comprehensive overview of the physical and chemical properties of these biofuels.

Table 1. *Properties of water and biofuels used in this study*[138–145].

Properties	Units	Water	Ethanol	RME	RE30	RE50	Diesel	Isooctane	n-Hexane
Density, at 0.1 MPa	kg/m^3	997	789.4	886-900	857-867	837-844	837	691	660
Viscosity, at 293 K	mm^2/s	1.02	1.13	6-9	4.5-6.63	3.5-5.06	3.04	0.72	0.45
Surface tension, at 293 K	N/m	0.073	0.022	0.0332	0.0298	0.0276	0.0258	0.0187	0.0179
Boiling point	K	373	337.5	593 - 605	516-525	465-471	447	368	342
Latent heat of vaporization	kJ/kg	2260	846	260 - 297	435-461	553-571	277	308	335
Specific heat (C_p)	kJ/kg K	4.18	2.414	2.47	2.454	2.442	1.75	2.1	2.26
Thermal conductivity	W/m K	0.609	0.166	0.149	0.154	0.157	0.15	114	86
Refractive index	------	1.33	1.36	1.45	1.42	1.405	1.46	1.38	1.37

3.7. Summary

This chapter provides a comprehensive overview of the experimental setup involved in investigation for Laser Induced Breakdown (LIB) of levitated liquid droplets. It begins by detailing the configuration of laser systems, encompassing both nanosecond and femtosecond laser specifications, acoustic levitation, and optical arrangements. This setup is designed to facilitate the study of distinct opto-hydrodynamic phenomena resulting from laser-droplet interactions. Finally, the chapter examines modifications to the laser setup to enable the evaporation of Carbon Nanomaterials (CNMs). The chapter outlines the setup and methodology for laser-induced evaporation, which allows for characterizing the evaporation process of CNMs. These discussions lay the foundation for understanding the results achieved in-line with the predetermined objectives.

4. Femtosecond laser induced breakdown in liquid droplets

The strength and location of Laser-Induced Breakdown (LIB) within the droplet during the interaction with the laser determine the characteristics of Opto-hydrodynamic phenomena, including fragmentation, deformation, propulsion, and breakup. These characteristics predominantly rely on the properties of the droplet, such as its optical density and breakdown threshold, as well as the distribution of laser energy within the droplet. The distribution of laser energy inside the droplet is influenced by its optical properties, including absorption, transmission, and reflection. Consequently, the control of the opto-hydrodynamic phenomenon can be achieved by adjusting the laser's intensity or the properties of the droplet. Increasing the laser intensity can result in more pronounced effects, and vice versa, and by controlling these parameters, the opto-hydrodynamic phenomena can be tailored for different applications. This section focuses on the interaction of the multiple femtosecond laser pulses on the dynamics of bubbles and breakup for different liquid droplets. The temporal evolution of the droplet after the laser pulses interaction, from the inception of bubble formation to its eventual breakup, is categorized into three modes:

a. **Bubble creation and dynamics:** This mode encompasses the formation of bubbles, their merging, and coalescence.

b. **Expansion and stretching of the droplet:** Consists of the droplet's expansion and stretching.

c. **Bubble rupture and sheet breakup:** This mode relates to the rupture of bubbles and the subsequent breakup of the droplet.

These observed modes are explained in terms of temporal dynamics, specifically early-time and late-time dynamics, as illustrated in Figure 9. Early-time dynamics describe the two modes: bubble and expansion dynamics, while late-time dynamics elucidate droplet rupture and sheet breakup.

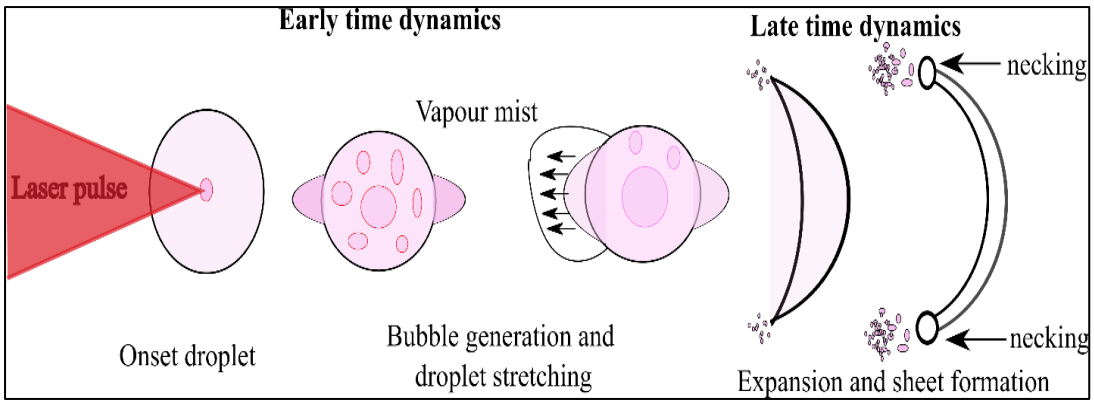

Figure 9. *Graphical depiction of the sequential dynamics of laser-droplet interaction through multiple laser pulses*[130].

4.1. Bubble creation and dynamics

This section explores the dynamics of bubbles formed in different liquid droplets when subjected to multiple femtosecond laser pulses. Figure 10 provides a visual representation of reflection images captured during the evolution of a diesel droplet as it interacts with a train of femtosecond laser pulses. The laser beam is focused inside the droplet, leaving the droplet's surface unaffected. Notably, the size and breakup of the resulting bubble can be controlled by adjusting the laser pulse energy and the number of pulses. At lower laser energy levels, the observed dynamics encompass the stages of bubble formation, coalescence, and rupture. The breakups strongly depend on the laser pulse energy and initial droplet size. This dependence arises from the amount of energy required to generate a sufficiently large bubble that can break the droplet. The process of bubble dynamics can be categorized into three distinct regimes:

I. **Formation of bubbles:** regime I involves the creation of bubbles. Each laser pulse induces the formation of a single bubble within the droplet. The oscillations due to the laser pressure pulse and hydrodynamic processes, including internal recirculation, are observed during the frame interval. With multiple bubbles inside the droplet, as bubbles approach neighboring bubble, the secondary Bjerknes force causes their coalescence resulting in a single larger bubble.

II. **Rupture of bubble, ligament stretching, and droplet breaking:** In regime II, the bubble ruptures, followed by the stretching of ligaments and the subsequent breakup of the droplet. Subsequent laser pulses lead to the breakage of the merged/coalesced bubble, causing the rupture of the droplet surface, evident in as jetting or splashing of bubbles from the droplet wall.

III. **Coalescence of bubbles and secondary droplets:** Regime III is characterized by the coalescence of bubbles and the formation of secondary droplets. Upon droplet surface rupture, secondary droplets are produced, as depicted in Regime II in Figure 10. The secondary droplets formed during the breakup process may coalesce in the presence of the acoustic field used for droplet levitation.

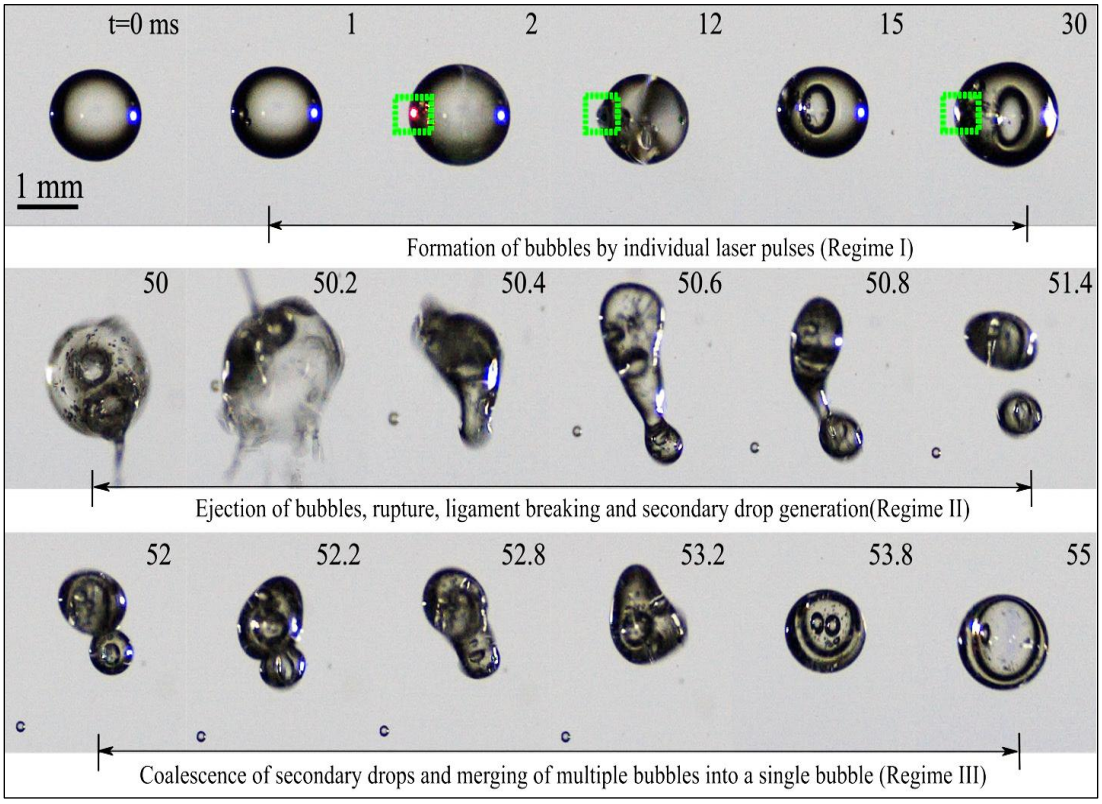

Figure 10. *Regimes of bubble dynamics in a diesel droplet through the interaction of multiple femtosecond laser pulses at E_l = 250 µJ, D_0 = 1.4 mm. The dotted rectangles highlight the creation of bubbles by individual laser pulses*[130].

Regime I correspond to the initial creation of small bubbles through the action of femtosecond laser pulses. Initially, multiple small bubbles emerge because of laser energy absorption. When the first laser pulse is launched, it generates a small-sized bubble within the droplet (t = 1 ms). At t = 2 ms, the introduction of another pulse leads to the formation of another bubble (highlighted within a dotted rectangle). Subsequent laser pulses generate new bubbles. These small bubbles subsequently coalesce to create larger bubbles with diameters of approximately 200 µm (Regime II). It is also possible that while a laser pulse primarily generates a bubble inside the droplet, the droplet's surface may rupture, as observed at t = 50 ms and 50.2 ms, initiating the breakup of droplet. Following the rupture of the droplet's surface, ligament stretching, and the eventual breakup occur, as evidenced by t = 50 ms (Regime II). The secondary droplets formed during the breakup process may coalesce, facilitated by the acoustic field employed for droplet levitation. The bubbles initially present in the parent droplet continue to coalesce, ultimately forming a larger bubble of approximately 600 µm in size (Regime III). Multiple pulses produce small bubbles which agglomerate during the laser pulse and bubble interaction to form large bubbles as seen in Figure 10. The energy of the bubble is proportional to the cube of its maximum radius and can also be expressed in terms of laser energy E_l as [146]

$$E_B = \frac{4 \times \pi \times P_i}{3} \times r^3{}_{max} = \gamma \times E_l \qquad (4.1.1)$$

where P_i and γ are pressure on the bubble by the liquid droplet and the fraction of the laser pulse energy converted to the bubble's energy respectively. From Figure 10, it is evident that bubbles generated by individual laser pulses coalesce and form a single larger bubble. The coalescence process depends on several physical parameters, including bubble size, the forces at play between two approaching bubbles, and the drainage time. The approximated equivalent radius for two approaching bubbles can be defined as

$$R_{eq} = \frac{2r_1 r_2}{r_1 + r_2} \qquad (4.1.2)$$

where r_1 and r_2 are the radii of two approaching bubbles. The size of these bubbles in the present study is in the range of 40-150 µm. As two bubbles approach each other, a thin layer of liquid forms in the contact region between them. This liquid

film progressively grows in area until it reaches a critical thickness, at which point it ruptures. This rupture event results in the fusion of the two bubbles into a single, larger bubble, as depicted in Figure 10 at t = 30 ms and t = 55 ms. The time from formation of contact area to complete fusion of bubble is often referred to as the coalescence time or film drainage time (t_{Ds}), can be obtained using the equation formulated by Kirkpatrick and Lockett [147]

$$t_{Ds} = r_f \sqrt{\frac{\rho_l \times R_{eq}}{16\ \sigma_l} \times ln\frac{h_0}{h_c}} \qquad (4.1.3)$$

where r_f represents the radius of the bubble contacting area, h_0 is the initial liquid film thickness, and h_c is the critical film thickness at which the film ruptures. For numerical calculation, the properties of diesel fuel used are, density (ρ_l) and surface tension (σ_l) are 837 kg/m^3 and 0.0258 N/m, respectively. The values for initial and critical film thicknesses typically fall within the range of 1-10 µm and 0.01 µm, respectively, as reported in the work by Oolman and Blanch [52]. For our analysis, we have adopted an initial film thickness (h_0) of 6 µm and a critical film thickness (h_c) of 0.01 µm.

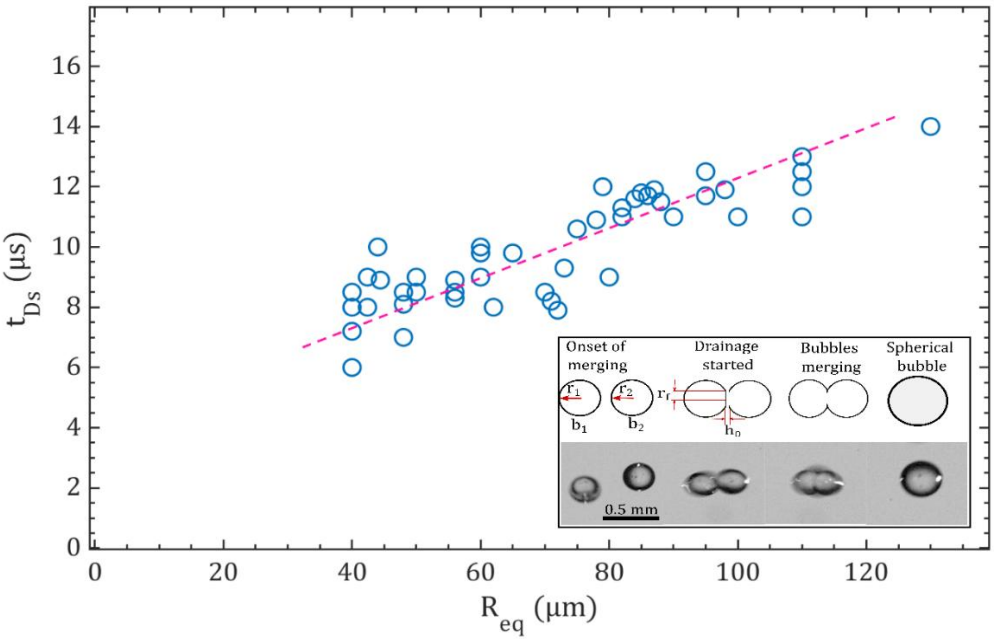

Figure 11. *Variation of drainage time with equivalent bubble radius of diesel droplet. The inset provides a visual representation of the coalescence process and the parameters employed for the analysis*[130].

The linear variation of drainage time with an equivalent bubble radius is observed in Figure 11. This indicates that the time required for drainage during the coalescence of bubbles exhibit a linear increase with the equivalent radius of the bubbles. The coalescence process starts as two bubbles (b_1 of radius r_1 and b_2 of radius r_2) move close to each other. Drainage commences when these two bubbles reach a distance of h_0, marking the initial thickness of the interposed film between them, causing it to flatten. The film continues to drain until it reaches a critical thickness ($h_c << h_0$) and then ruptures at the radius of the contact area (R_f). This process results in the formation of a single bubble and the corresponding drainage time (t_{Ds}) is an order of a few microseconds (~ 6 to 15 μs). Similar phenomena have been reported for acoustically generated bubbles[148] and microbubbles generated by individual laser pulses for different liquids [60]. Several factors come into play when assessing the merging of bubbles, including the speed of their approach, the viscosity of the surrounding fluid, and the forces acting on microbubbles that lead to their coalescence.

The interaction of coalescing or rebounding bubbles is considerably influenced by the generation of an acoustic field within the liquid caused by the laser pulse pressure. This acoustic field adds complexity to the coalescence process due to the Bjerknes forces exerted on the micro-bubbles. Bjerknes forces represent the translational forces acting on the bubbles within a sound wave and fall under the category of acoustic radiation force. External sound fields give rise to primary Bjerknes force, while secondary Bjerknes force emerges as an attractive or repulsive force between pairs of bubbles within the same sound field. These secondary forces result from the pressure field-generated oscillations of each bubble. An individual laser pulse creates the bubbles inside the droplet. The formed bubbles accelerate because of the strong pressure field generated by the laser pulse. As these bubbles approach each other, the secondary Bjerknes force is created between them. The final merger or coalescence of the bubbles depends on the Weber number and secondary Bjerknes force. The magnitude of the Bjerknes force depends on several factors, such as the size and shape of the bubbles, the frequency and intensity of the acoustic field, and the properties of the surrounding liquid.

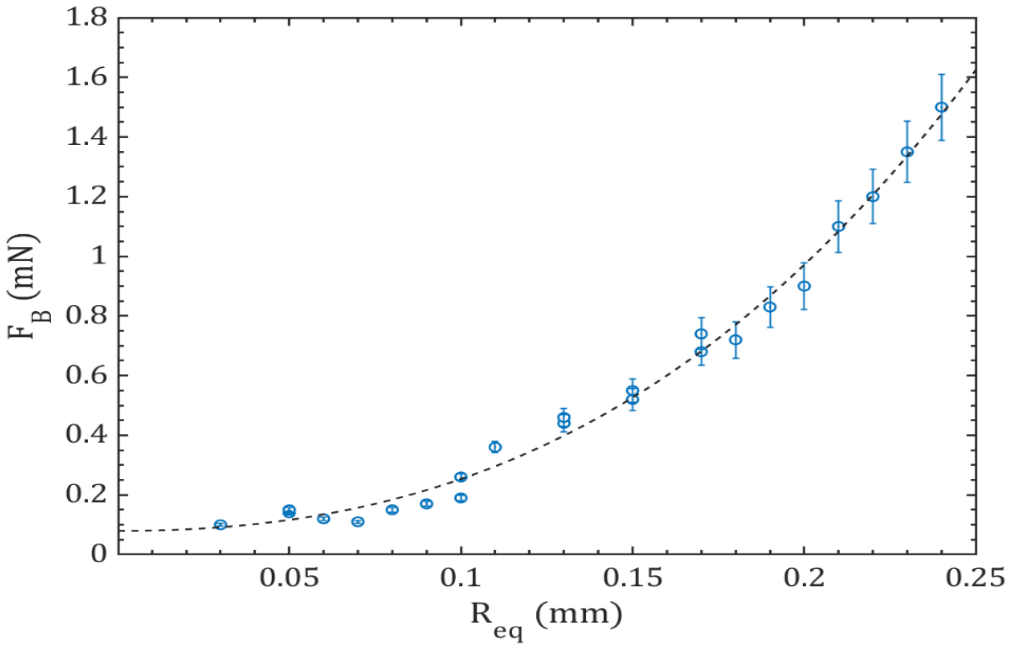

Figure 12. *Variation of Bjerknes force with equivalent bubble radius for diesel fuel at E_l = 250 µJ* [130].

The coalescence of bubbles can occur due to both primary and secondary Bjerknes forces, depending on the size of the bubbles. In this study, the emphasis is on measuring the secondary Bjerknes force, which is responsible for bubble-to-bubble interactions. The secondary Bjerknes force can be expressed in terms of volume change in a single acoustic cycle, taking into account the radii and radial velocities of the two interacting bubbles [149–151]

$$F_B = \frac{4\pi\rho}{r^2{}_{12}} \left(r_1{}^2 u_1 r_2{}^2 u_2\right) \qquad (4.1.4)$$

where r_{12} is the separation distance between the two micro-bubbles taken from the center of the bubbles, r_1, and r_2 are the radii of the two approaching bubbles, and u_1 and u_2 are the radial velocities of the respective bubbles. Figure 12 shows that the Bjerknes force increases exponentially with the equivalent bubble radius. This means that larger bubbles experience stronger forces than smaller bubbles when subjected to the same acoustic field. The Bjerknes force between the bubbles in this case is between 0.05 to 2.50 mN. The behavior of the bubbles when subjected to the acoustic field can vary. Sometimes, the bubbles may bounce off each other, while other times they may coalesce. The bubble may collapse due to the impact of free boundary during bubble interaction. If it does not collapse, it slows down the

motion of the bubbles. However, the major influence on the bubble interaction is caused by the laser-generated pressure field, which further creates a secondary Bjerknes force between the two bubbles. The coalescence or rebound of the approaching micro-bubbles can be predicted using a dimensionless Weber number (*We*), which is expressed in terms of ρ_l (the density of the liquid), *U* (the velocity of the two approaching bubbles), σ (the surface tension) and R_{eq} (the equivalent radius of the bubbles), given by

$$We = \frac{\rho_l U R_{eq}}{\sigma} \tag{4.1.5}$$

The values of *We* decide the coalescence or bounce back of the drops/bubbles. In this study, mostly $We < 0.2$ hence the process of coalescence is dominant over the bounce back of the bubbles.

4.2. Process of droplet stretching and coalescence of secondary droplets

In this section, droplet stretching, and the coalescence process of secondary droplets are discussed. Like the process of bubble dynamics, this phenomenon can also be divided into three distinct regimes: I. Bubble formation II. Ligament stretching and its breakage and III. Secondary droplet coalescence. When the laser pulses interact with the droplet, multiple bubbles are generated by individual laser pulses. These bubbles grow and merge to form larger bubbles. An increase in the size of the bubble leads to the stretching of the droplet. The elongation/ stretching of the droplet in the forward direction can be seen in Figure 13 (shadow images of droplet) from the time interval t = 25 ms to 25.4 ms. The stretching and eventual rupture of the droplet results in the formation of a long thick ligament. This ligament undergoes the Rayleigh plateau instability and eventually breaks into several secondary droplets. Following the detachment of these secondary droplets from the ligament, they proceed to coalesce with each other, ultimately forming a single drop. The coalescence or rebound of approaching secondary drops is influenced by the external acoustic field, as illustrated in Figure 13.

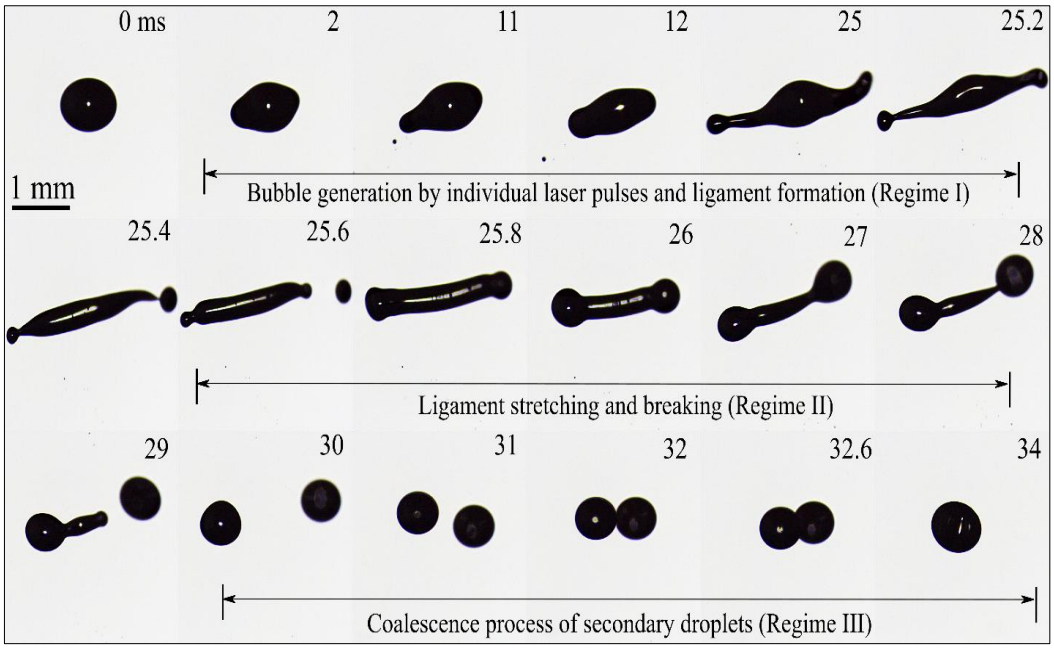

Figure 13. *Ligament-mediated breakup in a diesel droplet through the interaction of multiple femtosecond laser pulses at E_l = 250 µJ and D_0 = 0. 9 mm* [130].

The entire process of droplet coalescence can be divided into three consecutive stages (Regime III): (1) starting with their contact followed by the development of a thin bridge of fluid between them, (2) the subsequent contraction and breaking of the bridge, and (3) the growth of the connection neck between two droplets. In the first stage of coalescence (t = 31 ms), there exists a thin bridge between the two deformed droplets. Once this bridge breaks, a connection neck between two droplets is formed, and the process of coalescence is initiated (t = 32 ms), second stage. After the initiation of the connection between two droplets, the radius of the connection neck (t = 32.6 ms) increases. The growing speed of the neck results from a competition between the capillary forces driving the coalescence and opposing viscous forces. Finally, two droplets coalesce into one bigger droplet (t = 34 ms) in the third stage of the droplet coalescence process.

4.3. Sheet Breakup

In this section, droplet rupture followed by sheet formation and its breakup is discussed. At peak strength of 1050 µJ laser energy per pulse primarily results in the bubble generation inside the droplet and later fragmentation of the droplet through sheet breakup. Introduction of multiple laser pulses further generate multiple bubbles and leads to droplet ruptures. Afterward, the droplet will expand

in a vertical direction and a liquid sheet is formed. During the sheet formation, multiple fragments come out from the edge of the sheet. It's important to note that the droplets of similar onset diameters of the different liquids may fragment at varying numbers of laser pulses. The sheet breakup is categorized into two primary types: a) Stable sheet breakup and b) Unstable sheet breakup.

4.3.1. Stable sheet collapse

The shadowgraph images in Figure 14 show the sheet formation and its breakup of droplets of diesel subjected to a laser energy of 1050 µJ per pulse. The propulsion of the droplet depends on laser energy absorbed by the droplet which depends on local asymmetric boiling. This process leads to the formation of small vapor bubbles that break up and generate a thrust force on the droplet. It is important to note that the effects of laser radiation pressure and acoustic radiation pressure on the droplet during this process are insignificant. This means that the force generated by the vapor bubble formation and breakup is the main force responsible for propelling the droplet.

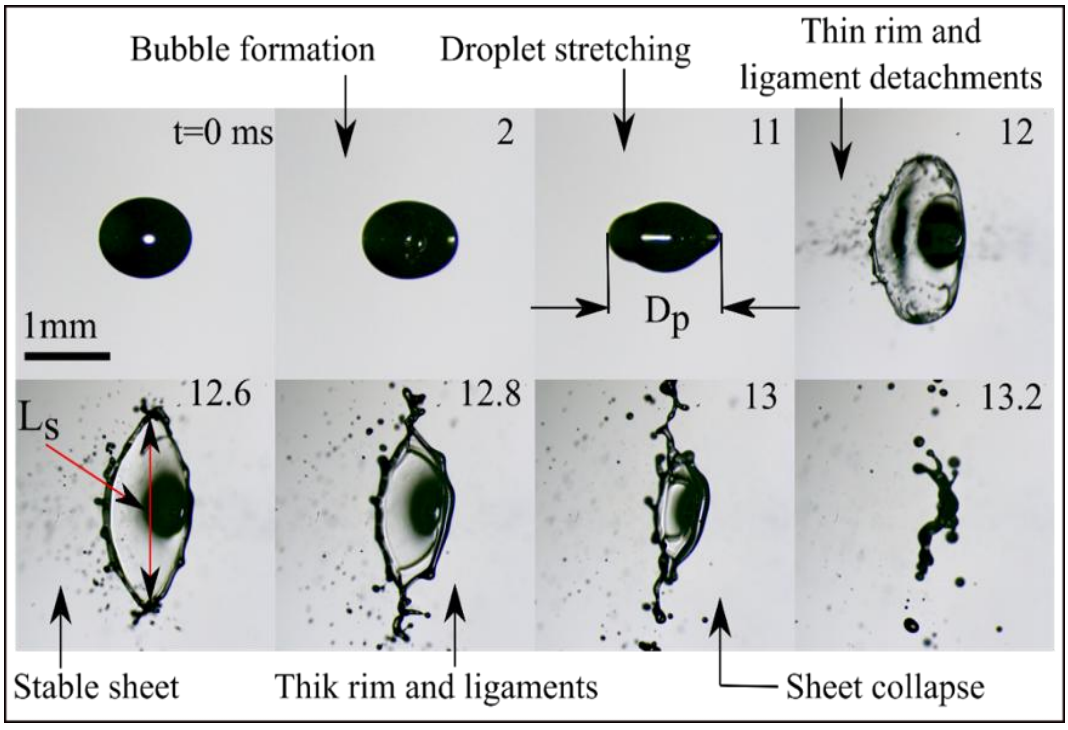

Figure 14. *The process of stable sheet formation in a diesel droplet through the interaction of multiple femtosecond laser pulses at E_l = 1050 µJ and D_0 = 1.1 mm* [130].

The induced thrust force deforms and stretches the droplet (see at t ~ 11 ms) resulting in breaking the droplet with primary ligament detachment (t ~ 12 ms) and forming a thin rim. Further, the liquid sheet is expanded to form a stable thick sheet. During this process of expansion, the rapid acceleration of the sheet is observed which is in order of $\alpha \sim 10^4$ m/s^2. The very high acceleration of the sheet is prone to Rayleigh-Taylor instability. The growth of this instability is calculated by Villermaux and Clanet [110]

$$\Delta t_{RT} = \left(\frac{\sigma_l}{\rho_l \times a^3}\right)^{1/4}, \tag{4.3.1}$$

where σ_l and ρ_l are the liquid surface tension and density respectively. Theoretically, the calculated growth rate is $\Delta t_{RT} \sim 0.03\ ms$ which is less than the experimental frame interval (0.2 ms). The initial (t ~ 12 ms) formed liquid sheet has a thin rim at the edge and a thick one at the center. Further, the gradual accumulation of the liquid at the edges of the sheet makes the sheet edge thicker and the rim diameter increases. This process leads to the forming of a more stable sheet having a thick rim and ligaments emerging from the edges (t ~ 12.6 ms). At the beginning of the process, small undulations form on the rim which may not be immediately discernible in the experimental observations. As the process continues, these undulations become more pronounced and develop into perturbations with a specific wavenumber, k_r, from which ligaments begin to grow. The wavelength of the corrugations provides an experimental measure of the growth rate of the Rayleigh-Taylor instability on the rim. This instability mode, growing fast on the rim, is expressed by Klein *et al.* [54] as

$$k_r \sim (a\rho_l/\sigma_l)^{\frac{1}{2}}. \tag{4.3.2}$$

The experimentally observed growth rate (6.12 ± 0.15 mm^{-1}) is of approximately the same order as the theoretically calculated (18 mm^{-1}) growth rate. Further, the formed ligaments undergo the Rayleigh-Plateau instability and eventually break up into smaller secondary droplets. The ligament breakup time is the time between the formation of the ligament and the pinching of the first droplet from the ligament. This experimental ligament breakup time is measured, and the value is compared to the capillary time scale of the ligament (τ_{cL}). This time is expressed in terms of surface tension, the density of the liquid, and the ligament diameter L_d, which is given by [129,152]:

$$\tau_{cL} = \sqrt{\frac{\rho_l \times {L_d}^3}{\sigma_l}}. \qquad (4.3.3)$$

The theoretically measured ligament capillary time is 0.4 ms whereas the experimental breakup time observed is 0.6 ± 0.2 ms. Once the ligaments break, the sheet collapses under the influence of surface tension. The lifespan of the sheet is the time when the sheet collapses, hence the experimental collapse time is compared with the capillary time scale of the sheet. The capillary time is theoretically given by Avila and Ohl [122].

$$\tau_c = \sqrt{\frac{\rho_l \times {D_p}^3}{8\,\sigma_l}}, \qquad (4.3.4)$$

where D_p is the diameter of the liquid droplet at a pre-breakup instant. The theoretical capillary time calculated is 1.2 ms and the observed experimental sheet collapse time is 1.0 ms.

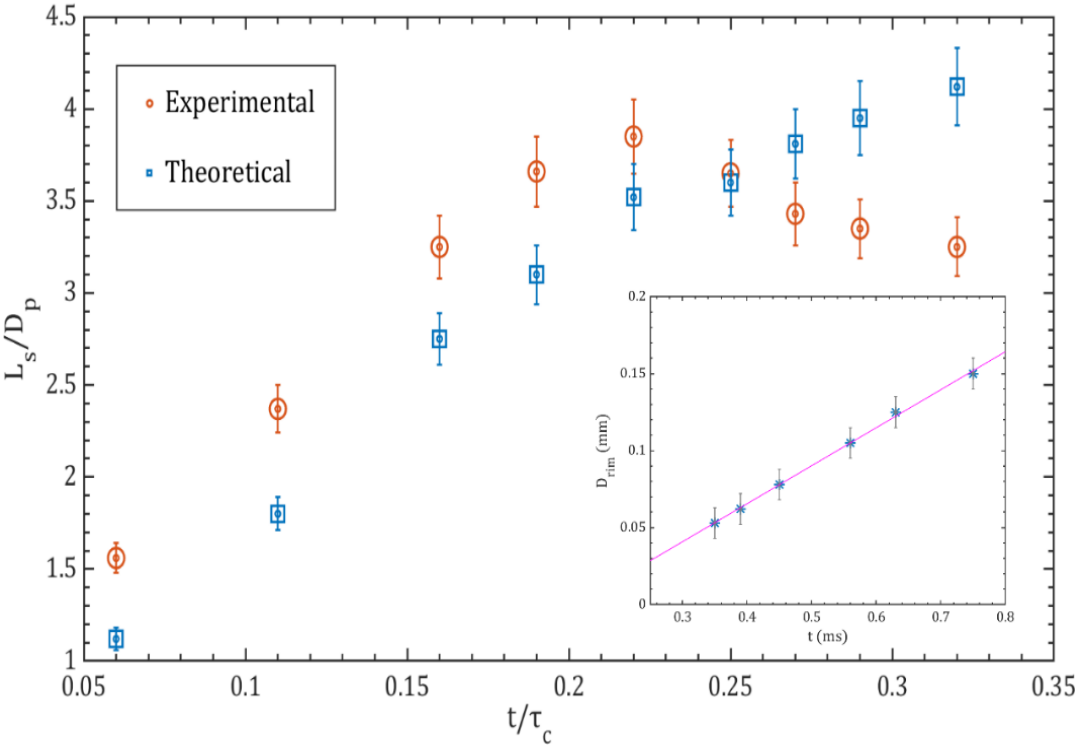

Figure 15. *Experimental and theoretical comparison of temporal variation of the normalized length scale of the sheet. The inset represents the temporal variation of rim diameter for the stable sheet*[130].

Figure 15 describes the experimental and theoretical evolution of the stable sheet diameter over time, along with the increase in the rim diameter due to continuous liquid accumulation at the edge. The results obtained from the experiments for the

evolution of the length scale of the sheet nearly match with the evolution of the sheet theoretically predicted. The inset in Figure 15 depicts the linear relationship between the rim diameter and time. The theoretical model proposed by Klein et al. [55] is used to explain the observed sheet evolution dynamics in the experimental study. A mathematical model can be used to describe the development of a stable liquid sheet over time is expressed as [53]

$$\frac{L_s(t)}{D_p} = 1 + \sqrt{3\,We_d}\ \frac{t}{\tau_c}\,(1 - \sqrt{3}\,t/2\tau_c)^2, \tag{4.3.5}$$

where, We_d is given by

$$We_d = \frac{E_{k,d}}{E_{k,cm}}\,We. \tag{4.3.6}$$

Here, $\frac{E_{k,d}}{E_{k,cm}}$ is the ratio of deformation to propulsion kinetic energies which depends on the laser beam profile[55]. The Weber number (We) is a dimensionless parameter that describes the ratio of the kinetic energy of a droplet to the surface energy that resists the deformation of the droplet. In the case of sheet fragmentation caused by nucleated bubbles, the Weber number is modified because the presence of bubbles can change the surface tension of the liquid, which affects the energy required to deform the liquid sheet. However, under conditions of higher laser intensities, the nucleated bubble vanishes. In this scenario, the modified Weber number is defined as the displacement kinetic energy of the drop to its surface energy, which is given by

$$We \sim \frac{\rho_l D_p U^2}{\sigma_l}, \tag{4.3.7}$$

where *U* is the axial velocity of the sheet. The Weber number (We^*) is sometimes rescaled to We_d to account for the energy required for deformation that is not available for propulsion. The ratio of kinetic energy to propulsion energy can be expressed in terms of the radial velocity inside the sheet ($u_r \sim r/t_{max}$), which is given by

$$\frac{E_{k,d}}{E_{k,cm}} \sim \frac{\int_0^R {u_r}^2\, r\, dr}{U^2 \int_0^R r\, dr}, \tag{4.3.8}$$

Here, the time taken for the sheet to reach its maximum extension is represented by t_{max} and the maximum radius of the stable sheet is denoted by $R_{S_{max}}$. Then the ratio $\frac{E_{k,d}}{E_{k,cm}}$ can be written as

$$\frac{E_{k,d}}{E_{k,cm}} \sim \frac{(R_{S_{max}})^2}{2\,U^2\,(t_{max})^2}. \qquad (4.3.9)$$

The derived equations are based on energy conservation along the curved streamline, extending from the heart of the crushing droplet to the expanding sheet. However, when an expanding sheet reaches its maximum radius, the theoretically calculated time exceeds the experimentally observed time. After reaching its maximum expansion, the sheet undergoes deceleration and collapses due to surface tension forces. This deceleration leads to a reduction in the sheet's radius, consequently causing a decrease in the Weber number (W_{ed}). As a result, there is a decrease in the normalized time for the experimental case. In essence, the discrepancy between theoretical and experimental times can be attributed to the dynamic behavior of the sheet, which involves both expansion and subsequent collapse, influenced by surface tension effects. The discrepancy in the normalized time scale arises from variations between the theoretical capillary time and the experimental sheet collapse time. Specifically, when t/τ_c >0.2 (Figure 15), the theoretical capillary time scale surpasses the experimental sheet collapse time. Consequently, this leads to an augmentation in the normalized time scale for the experimental case, contributing to an increase in the length scale of the stable sheet. Conversely, the theoretical case exhibits the opposite trend, experiencing a decrease in the length scale of the stable sheet due to the theoretical capillary time scale being higher than the experimental sheet collapse time during this timeframe.

4.3.2. Unstable sheet breakup

The shadowgraph images displayed in Figure 16 provide a chronological overview of the formation and subsequent breakup of unstable sheets generated from diesel droplets subjected to laser pulses with an energy of 1050 μJ. The early-time dynamics shows a phenomenon similar to that of the stable sheet breakup process. However, the late-time dynamics show the breaking process via unstable sheet formation.

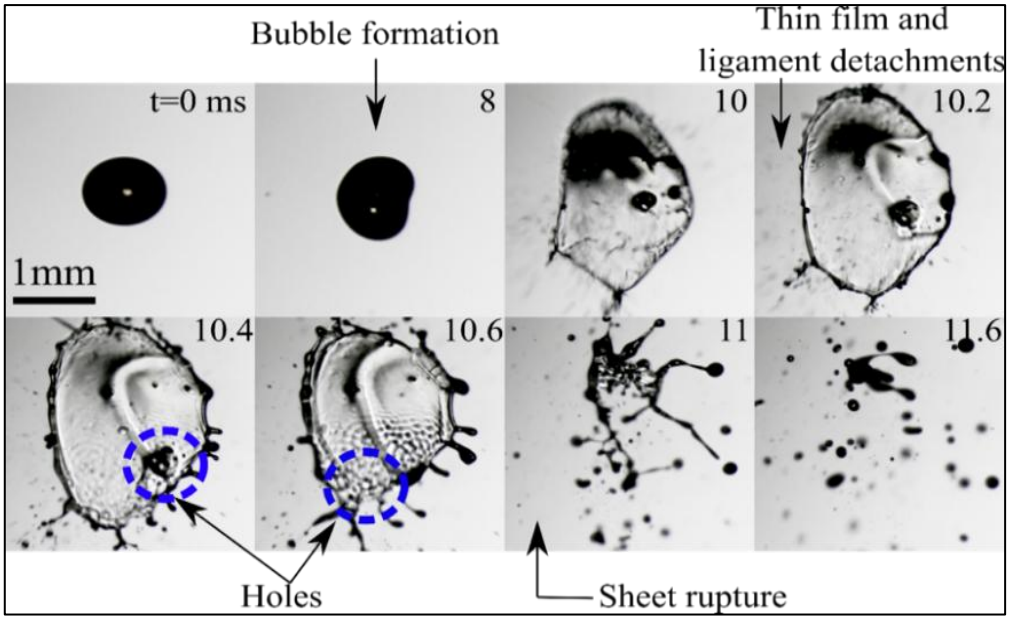

Figure 16. *The process of unstable sheet breakup in a diesel droplet through the interaction of multiple femtosecond laser pulses at E_l = 1050 µJ and D_0 = 0.95 mm*[130].

The breaking of the bubble induces the thrust force that deforms the droplet into a sheet (t_1 ~ 10 ms). This sheet evolves in an unstable manner, developing undulations and holes on its surface by t = 10.4 ms. The evolution of the hole causes localized thinning of the sheet and finally, it ruptures (t =11 ms). The liquid ligaments are formed due to the merging of holes in the sheet and surface undulations, as visible at t = 10.6 ms in Figure 16. These ligaments then become Rayleigh–Plateau unstable and form relatively large droplets as compared to the initial ejecta on the left-hand side of the droplet, as seen at t = 10 ms in Figure 16. The evolution of the holes represented by growth rate/velocity of the holes. Hence, by measuring the velocity of the holes (V_H), the local planner sheet thickness (H) can be obtained by Taylor-Culick law [122,153]

$$H = 2\,\sigma/\rho\,V_H{}^2. \qquad (4.3.10)$$

4.4. Catastrophic breakup

Following the growth of a bubble within the droplet, the bursting of the bubble leads to catastrophic breakup of droplet generating secondary micro-droplets. Figure 17 shows the breakup process of the diesel droplet at 1050 µJ and the onset diameter of the droplet is D_0 = 0.55 mm.

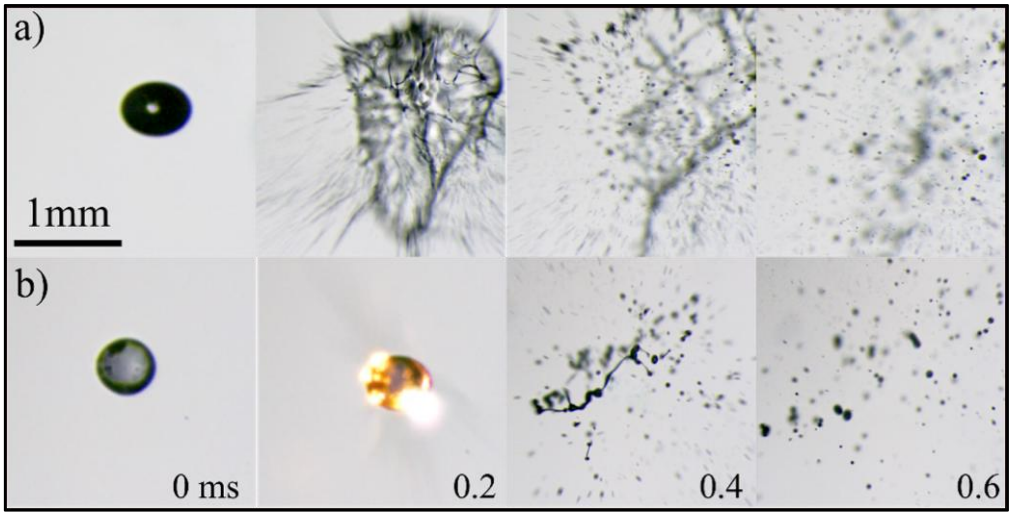

Figure 17. *Catastrophic breakdown in a diesel droplet through the interaction of multiple femtosecond laser pulses at E_l = 1050 µJ and D_0 = 0.55 mm* [130].

The pressure force (F_p) due to the breaking of the bubble can be expressed in terms of internal pressure (P_{in}), ambient pressure (P_a), and radius of the bubble (r_b) is given as

$$F_P \sim (P_{in} - P_a)\, \pi\, {r_b}^2. \tag{4.4.1}$$

Similarly, the surface tension force is expressed as

$$F_s \sim \sigma_l \pi\, D_p \tag{4.4.2}$$

Weber number for droplet is of the order of 10^4. The sizes and the velocities of the secondary droplets are in the range of ~ 10 to 80 µm and ~ 1 to 5 m/s respectively. The Pearson correlation [154] is used to indicate the dependency of the secondary droplet size and its velocity. It is observed that the size of the secondary droplets increases, with corresponding decrease in velocity and vice versa. Hence it indicates that the secondary droplet size and the corresponding velocity are negatively correlated with a Pearson correlation coefficient of ~ -0.6. The empirical equation of the Pearson correlation coefficient [154] is given as

$$\mathrm{Correl}(D_S, V_S) = \frac{\sum (D_S - \bar{D}_S)(V_S - \bar{V}_S)}{\sqrt{\sum (D_S - \bar{D}_S)^2 \sum (V_S - \bar{V}_S)^2}}, \tag{4.4.3}$$

where $\overline{D}_S$ and $\overline{V}_S$ are the average diameter and average velocity of the secondary droplets, respectively. Note that similar breakup patterns are observed for larger droplets when the laser energy exceeds 1050 µJ, which will be considered in our future investigations.

4.5. Overview of the FS laser study

4.5.1. Results for RME

Figure 18 presents the evolution of an RME (Rapeseed Methyl Ester) droplet under varying laser energies. Similar to the phenomenon observed in diesel droplets, the process involves bubble dynamics followed by sheet breakup in the case of RME. However, the key difference is longer time required for breakup compared to that of the diesel. At lower energy levels (Figure 18 d), the process includes bubble generation, droplet stretching, and coalescence. As we increase the energy, dynamics change to sheet formation and breakup (Figure 18 a-c).

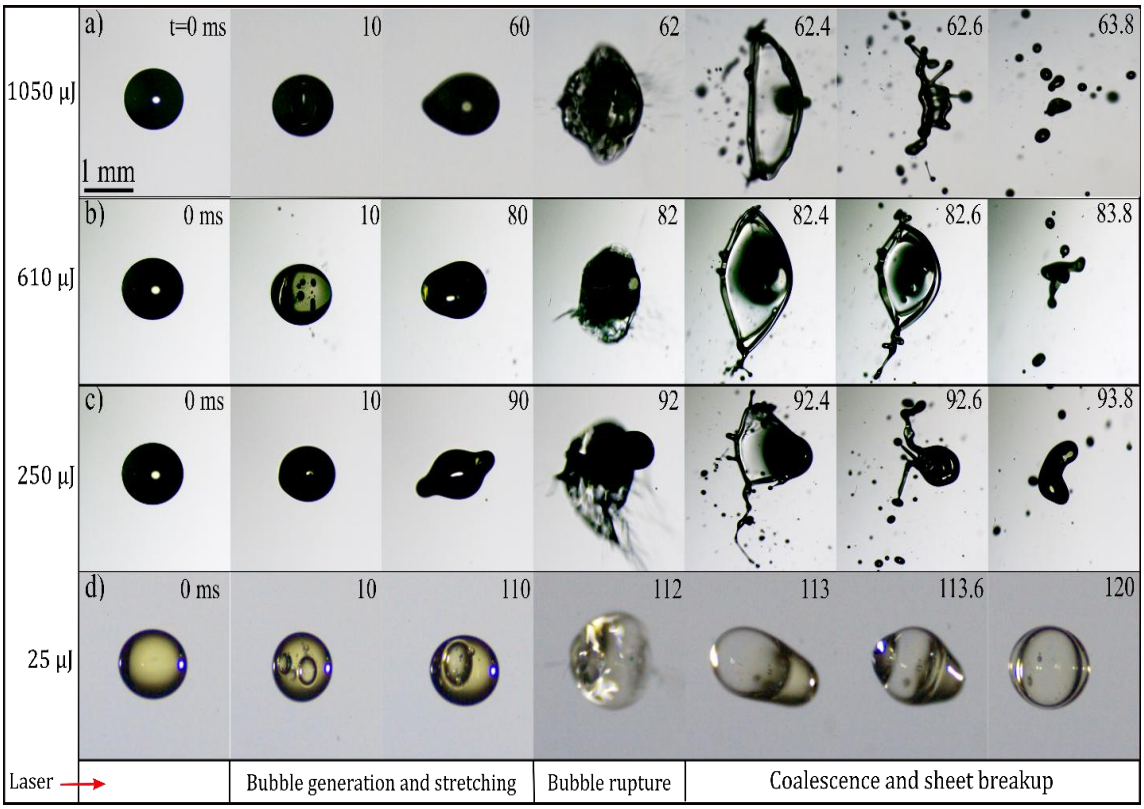

Figure 18. *Time sequence images of RME droplet showing bubble dynamics and breakup through the interaction of multiple femtosecond laser pulses for different laser energy (E_I) and D_0 = 1.0 mm* [130].

When a bubble expands, it causes the rupture of a thin liquid film. This process can lead to the formation of submicron-sized droplets. For smaller droplets, the film separating the expanding bubble from the atmosphere may rupture earlier, resulting in a more violent acceleration of the droplet. This can lead to the formation of submicron-sized droplets and a coarser fragmenting front part of the droplet. This process is likely caused by Rayleigh-Taylor's instability. On the other hand, larger droplets or moderate energies may later result in the film rupturing. In this scenario, the pressure difference between the expanding bubble and the atmosphere results in a less violent acceleration of the droplet body, causing it to deform into a sheet. The behavior of the sheet depends on its size and surface tension. Smaller sheets are dominated by surface tension and collapse back into a droplet, while larger and thinner sheets may rupture, leading to Rayleigh-Plateau unstable liquid films. For even larger droplets or lower energies, the droplet may remain intact with only minimal loss of mass.

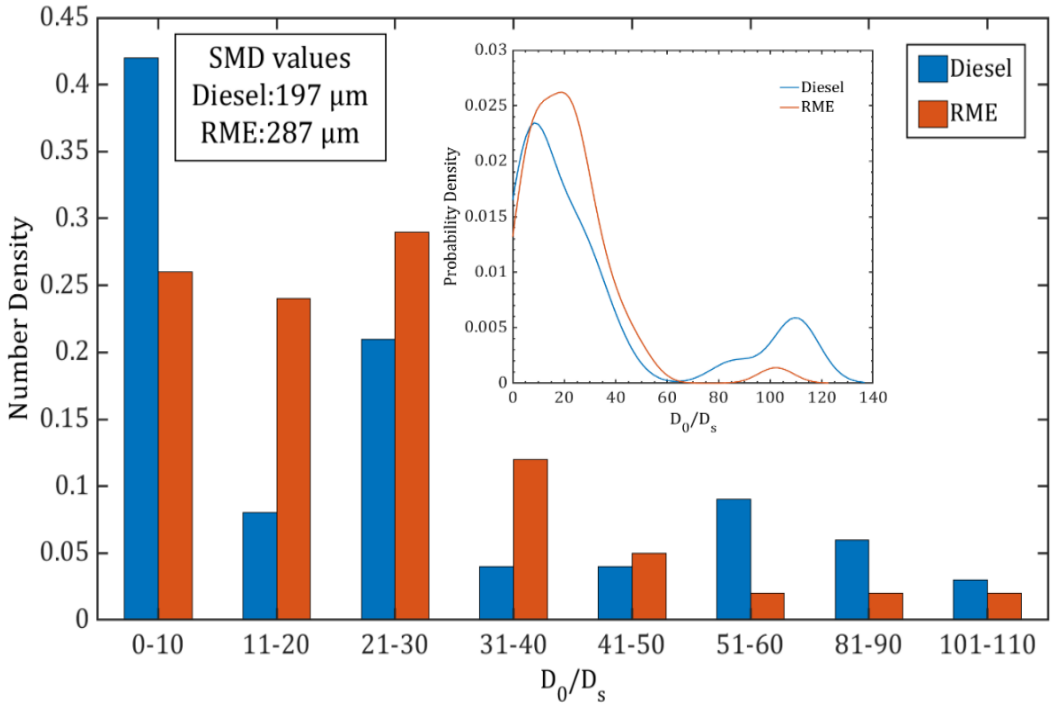

Figure 19. *Normalized secondary droplet size distribution of the diesel and RME corresponding to a laser pulse energy of 1050 µJ, and onset droplet diameter of D_0 = 1.0 mm. Inset inside the Fig. 12 represents the probability density function plotted against normalized secondary drop size for diesel and RME droplets. Where D_s and D_0 are the secondary and onset droplet diameters respectively*[130].

4.5.2. Secondary droplet size distribution

Figure 19 illustrates the normalized secondary droplet size distribution for diesel and RME droplets at an energy level of 1050 μJ. There is a discernible difference in the trend of droplet size distribution between diesel and RME. The secondary droplets, primarily generated by ejected fragments, tend to be smaller than the droplets formed through sheet breakup. The Sauter Mean Diameter (SMD) values for diesel and RME represent the average size of the droplets generated after the breakup process.

4.5.3. Dimensionless number distribution

The bubble generation and droplet breakup process observed above are summarized in Figure 20. The three different regimes observed in the process of bubble formation and breakup from the diesel and RME droplets experiments are shown. The first regime i.e. bubble generation is observed at a small D_b/D_o ratio, which indicates the generation of multiple bubbles for both fuels. The time taken for bubble generation of both fuels at lower laser energy levels is higher. As the ratio D_b/D_o increases, the regime changes to droplet stretching (regime II: yellow shade) and subsequently undergoes bubble rupture and sheet breakup (regime III: represented in pink color). In all the cases, the time required for RME is generally longer compared to that of diesel fuel. Regime III is observed at a higher D_b/D_o ratio and at a moderate ratio i.e. only droplet stretching occurs. Note here that, the time required for the breakup of both the liquid droplets decreases with increasing laser energy. The graphs show the different regimes of bubble formation and time as a function of laser energy and effect of liquid properties. Increasing the laser energy reduces the time for bubble formation and quickly shifts to droplet rupture and sheet breakup. The physical properties of RME (absorption coefficient, surface tension and viscosity) delay the process of bubble formation, stretching and breakup. The changes in the regimes from bubble dynamics to sheet breakup are presented in Table 2. Initially, the bubble dynamics is observed at all laser energy and lower ratio D_b/D_0 for both diesel and RME fuels. For $D_b/D_0 > 0.5$, sheet breakup is observed at 750 μJ and 1050 μJ laser energy for diesel, while in the case of RME, it is observed only at a higher laser energy of 1050 μJ. Droplet stretching

is observed from $D_b/D_0 > 0.4$ at all energy for RME and diesel, specifically at 250 -750 µJ laser energy.

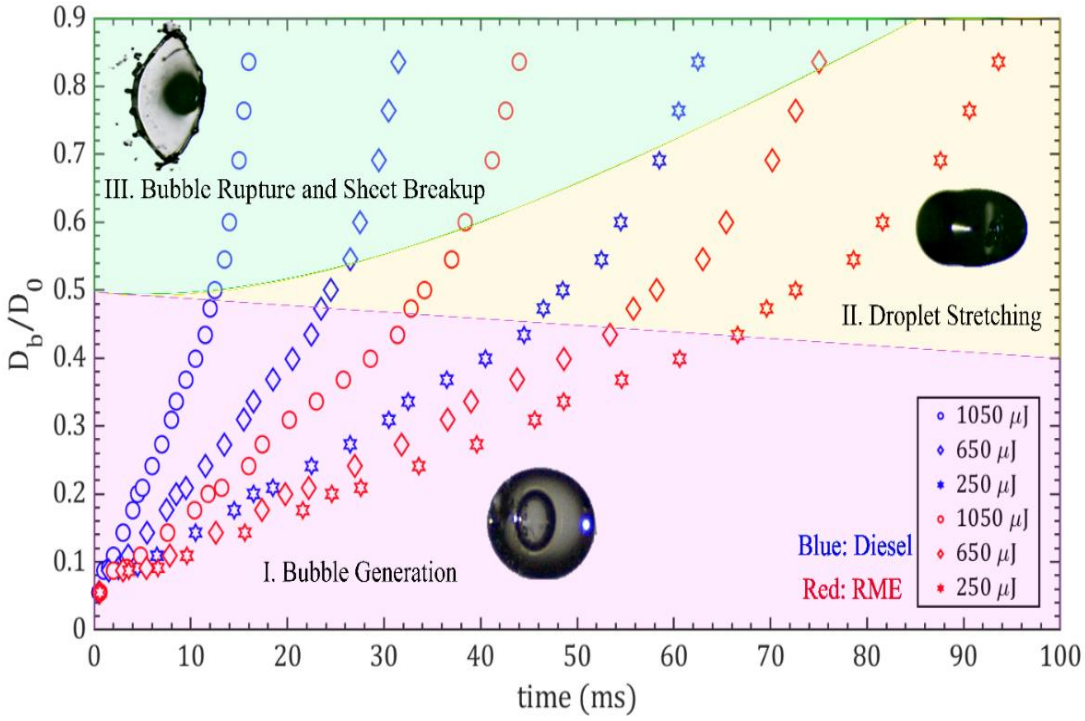

Figure 20. *Regime map of temporal variation of a normalized bubble size distribution at different laser pulse energies for the diesel and RME droplet* [130].

Table 2. *Detailed description of regime map presented in the Figure 20*[130].

Regimes	D_b/D_0	Laser energy	Liquids
I. Bubble generation	< 0.5	All	Both
II. Droplet stretching	> 0.4	250 µJ	Both
		750 µJ	Both
		1050 µJ	RME
III. Bubble rupture and Sheet breakup	> 0.5	750 µJ	Diesel
		1050 µJ	Both

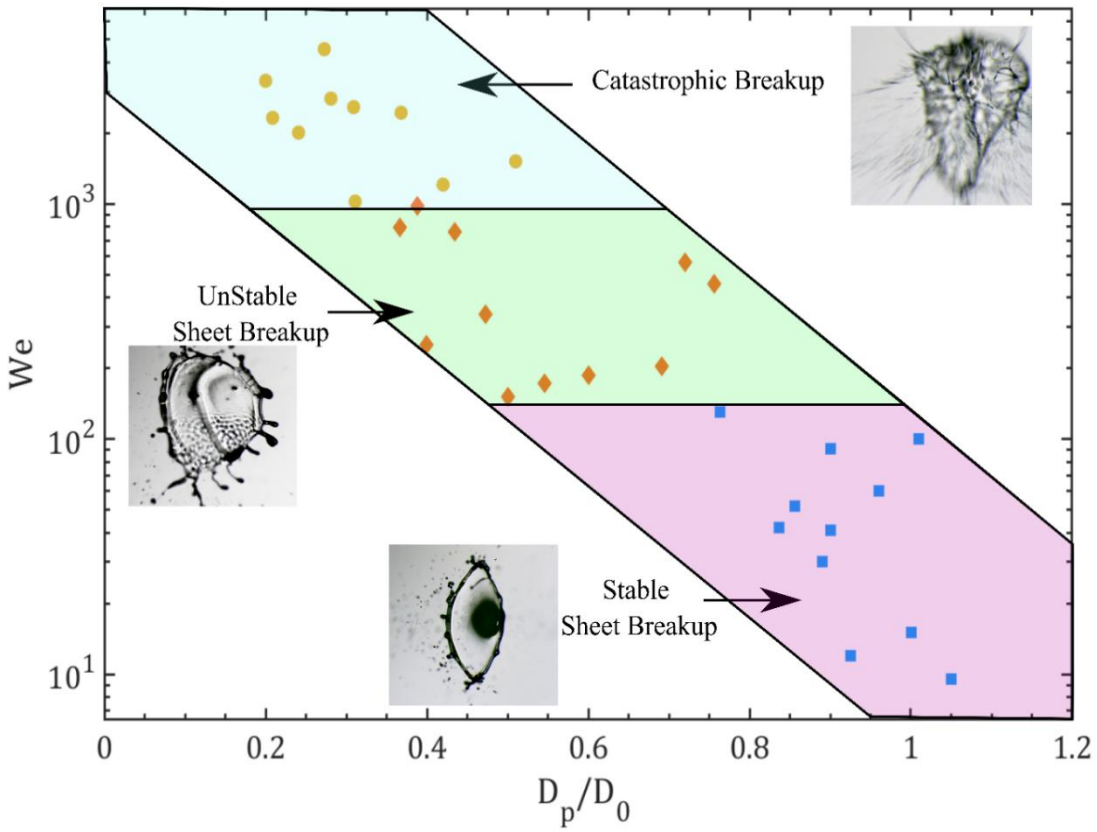

Figure 21. *The detailed mapping of breakup features observed in the current study* [130].

The detailed mapping of the breakup features is illustrated in Figure 21. In this work, we observed the breakup feature changes from low strength stable sheet to high strength catastrophic breakup depending on the laser energy and diameter at a pre-breakup instant. The mapping of the breakup mode is decided by the ratio D_p/D_0 and Weber number, We as shown in Figure 21. The stable sheet breakup is observed at a higher ratio D_p/D_0 and lower We, whereas the lower ratio D_p/D_0 and higher We corresponds to unstable sheet breakup. When the bubble breaks, the impulse pressure is applied on the drop surface. Because of this, the fluid motion develops inside the droplet. The propulsion of the liquid sheet represented by axial velocity U follows the global mass conservation given as

$$P_i \tau_i {D_p}^2 \sim \rho_l {D_p}^3 U, \tag{4.5.1}$$

where

$$U \sim \frac{P_i \tau_i}{\rho_l D_p}. \tag{4.5.2}$$

Here P_i denotes the impulse pressure on the droplet after bubble breakup, U is the axial velocity of the sheet, and τ_i represents the time scale on which impulse acts. In this study, for same-size bubble breakup the impulse pressure P_i and time scale τ_i remain constant. Hence, the axial velocity of the sheet is approximated to be inversely proportional to the pre-breakup diameter and expressed as

$$U \sim {}^{1}/_{D_p}. \qquad (4.5.3)$$

Therefore, from equations (4.5.2) and (4.5.3), the Weber number is expressed as

$$\mathrm{We} \sim {}^{1}/_{\mathrm{D_p}}. \qquad (4.5.4)$$

Hence, the dependency of the We are given by the equation (4.5.4) shows the stable sheet corresponds to the higher ratio 'D_p/D_0' and lower 'We', whereas the unstable sheet breakup corresponds to the lower ratio 'D_p/D_0' and higher 'We'. More violent fragmentation of droplets is observed at very high We and lower ratio which is represented as catastrophic breakup. Hence, for constant onset diameter of the droplet, the weber number depends on the prebreakup diameter of the droplet. Therefore, the D_p is deciding parameter for behavior of the breakup. The breakup behavior changes with liquid properties and laser pulse energy. In summary, The transition of the weber number with droplet ration for different liquids describe the breakup behavior and its strength.

4.6. Summary

This chapter gives insights to the dynamics of femtosecond laser-induced bubbles and the breakdown of diesel and RME droplets. It reveals a logarithmic correlation between bubble size/breakup and laser energy, leading to violent droplet acceleration and submicron droplet formation. Micro-bubble formation and interaction are influenced by laser energy and pulse number, impacting size distribution. The process involves stages of bubble generation, droplet stretching, sheet formation, and catastrophic breakup. Droplet behavior varies based on size and energy, with sheets either collapsing or rupturing. Overall, these insights contribute to optimizing combustion parameters by providing the understanding of the atomization characteristics of liquids and also finding applications in areas like nano-microchip removal, microemulsions and polymer fragmentation.

5. Nanosecond laser induced breakdown in liquid droplets-532 nm

The interaction of nanosecond laser pulse with the droplet leads to either droplet deformation or fragmentation. Here, two primary modes of breakup are observed, viz. sheet breakup (stable and unstable) and droplet rupture leading to air entrapment.

5.1. Fragmentation of single component liquids

5.1.1. Air Entrapment

In inkjet-based fabrication, the size of entrapped air bubbles is critical, as it can negatively impact uniformity and conductance. At very low impact velocities, the lubricating air film may destabilize and disrupt asymmetry, enabling the escape of air. The droplet partially ruptures at a low incident laser energy, allowing air to get entrapped inside the residual droplet. The droplet subsequently retains its spherical shape and does not undergo further breakup. Figure 22 shows the reflection images of an air bubble trapped inside the droplet.

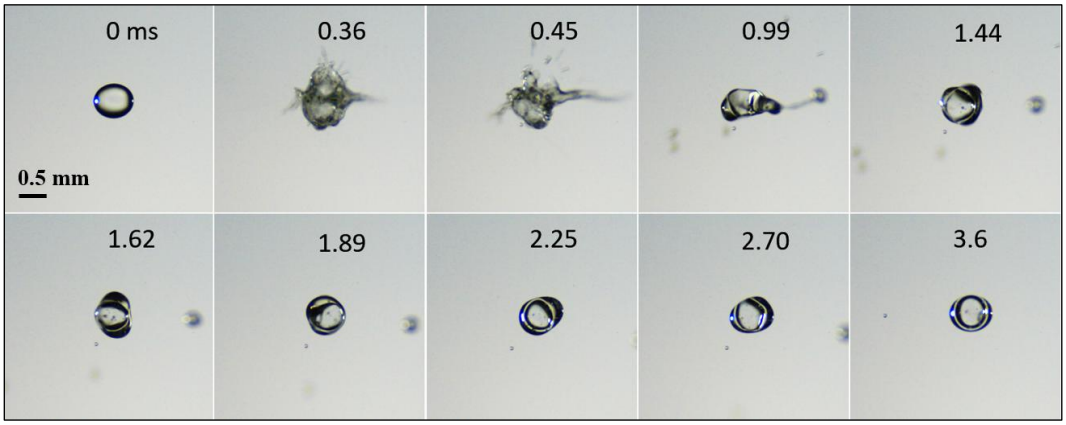

Figure 22. *Fragmentation and subsequent air entrapment in water droplet: E_l = 0.5 mJ, D_0 = 0.6 mm, and the maximum diameter of bubble is 0.52 mm* [129].

5.1.2. Breakup mechanisms with different laser energies

Figure 23 shows the sequence of images corresponding to the fragmentation of water droplets for different incident laser energies. The reflection images associated with the sheet formation and its collapse is shown in Figure 23 (a) for 3.14 mJ laser energy. A stable sheet is formed, which eventually collapses and breaks into large ligaments. These ligaments subsequently undergo pinch-off and result in the formation of secondary droplets. The secondary drops generated are of the order of 100 µm in diameter. Figure 23 (b)-(d) show the shadowgraphs of the influence of laser pulses with energy 2.5 mJ, 5.3 mJ, and 7.15 mJ on the water drops. As seen in Figure 23 (b)-(c), initially, small fragments are ejected (t = 0.09 ms) before the formation and radial expansion of the sheet. The sheet propels forward due to the impact of the laser, and a circular rim is created. The ligaments are formed due to instability in the circular rim which subsequently undergo pinch-off, and ejection of fine secondary droplets occur from the sheet rim (t = 0.18 ms).

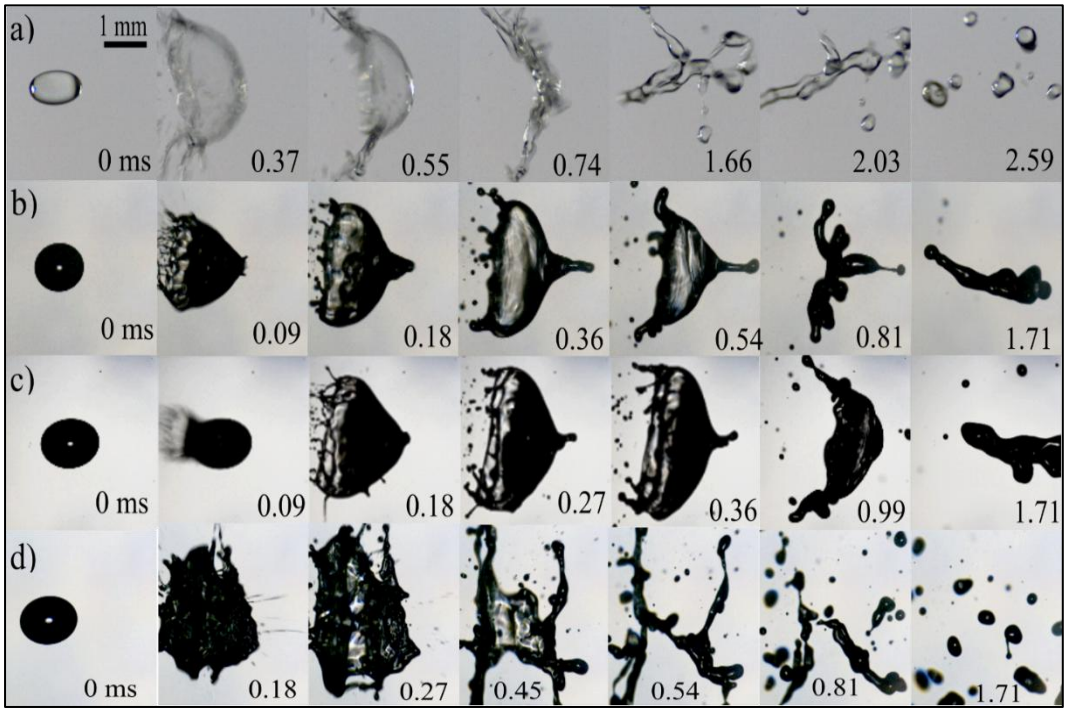

Figure 23. *Fragmentation of water droplet: a) unstable sheet at E_l = 3.14 mJ, D_0 = 0.9 mm b) Stable stretched sheet at E_l = 2.5 mJ, D_0 = 1.1 mm c) Stable stretched sheet E_l = 5.3 mJ, D_0 = 1.3 mm d) prompt fragmentation at E_l = 7.15 mJ, D_0 = 1.2 mm* [129].

As the sheet expands, a ligament/jet emanates from the center of the sheet and grows towards the direction of the laser. The ligament subsequently breaks into a droplet (t = 0.81 ms in Figure 23 (b)). The liquid sheet formed is more stable and thicker compared to Figure 23 (c). The vertical expansion of the droplet is minimal, to only about 75% of the sheet size shown in Figure 23 (c), and a negligible mist is produced on the side where laser pulse interacts with the droplet. The maximum expansion of the sheet is reached at t = 0.36 ms, where it collapses due to the influence of surface tension. When the incident laser energy is increased, prompt fragmentation occurs (Figure 23 (d)). A rapid breakup from both sides of the droplet results in the formation of long ligaments. The ligaments break into the secondary droplets with diameters in the range ~ 30-495 µm. Figure 24 shows the shadowgraphs of fragmentation of ethanol droplets at various laser energies. In Figure 24 (a)-(b), the initial droplet expansion is similar to that observed in a water droplet in Figure 23. The sheet expansion is maximum at 0.74 ms, and the sheet remains intact up to 1.3 ms. Later this sheet collapses under the influence of surface tension and disintegrates into small droplets. The sheet lifetime depends on the onset diameter of the droplet. The average secondary droplet size generated after the breakup is in the range of ~ 60-100 µm, depending on the laser energy and onset droplet diameter. At higher laser energy, Figure 24 (c), the sheet expansion is maximized, and thick ligaments are formed, which subsequently undergoes Rayleigh-Plateau breakup.

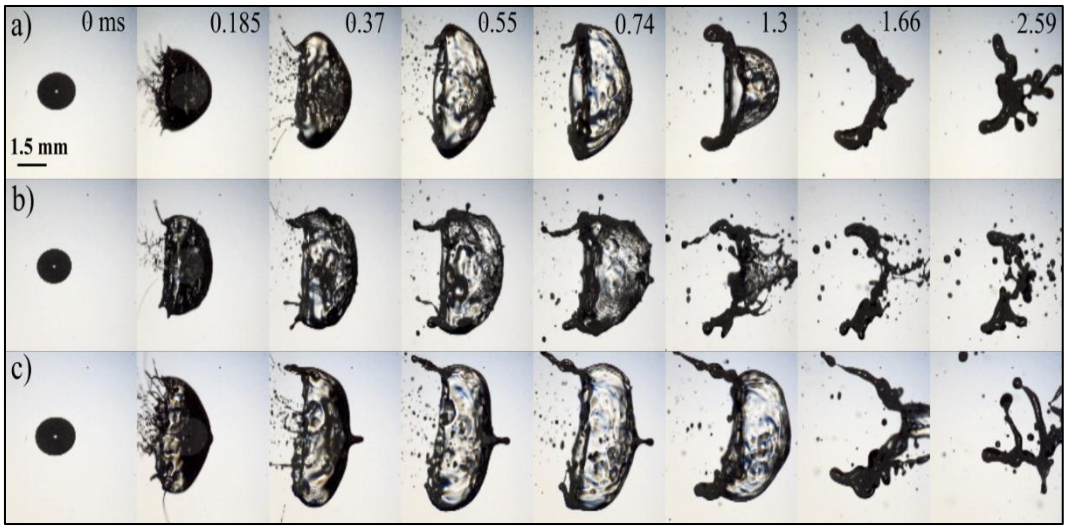

Figure 24. *Fragmentation of Ethanol droplet at different laser energies: a) E_l = 2.5 mJ, D_0 = 1.4 mm b) E_l = 5.3 mJ, D_0 = 1.3 mm c) E_l = 7.15 mJ, D_0 = 1.5 mm* [129].

In all these cases, the propagation of capillary waves is observed on the sheet's surface due to the impact of fragments on the liquid sheet. The capillary time (τ_c) is calculated by equating the surface energy to the kinetic energy of the sheet with negligible mass loss at the onset of the droplet breakup [122] given by

$$\tau_c = \sqrt{\frac{\rho_l * {R_0}^3}{6 * \sigma_l}}. \qquad (5.1.1)$$

Here σ_l and ρ_l are the liquid surface tension and density, respectively. The acceleration of the sheet (a) is approximately 30×10^3 m/s^2 calculated from Figure 24 (c). For Figure 24 (c), τ_c = 1.28 ms, which agrees well with the observed sheet lifetime, i.e., τ_c = 1.3 ms. Figure 23 (c) shows a significant radial acceleration between 0.09 ms and 0.18 ms. Hence, the sheet is prone to Rayleigh-Taylor instability (RT) [122], and the growth time (Δt_{RT}) of instabilities can be estimated from the model of Villermaux and Clanet [110]. From equation (4.3.1), the growth time for the ethanol droplet shown in Figure 24 (c) is Δt_{RT} = 0.11 ms. A lower limit for the initiation of the instability cannot be assessed since the time interval between two frames is 0.185 ms. The liquid sheet starts to decelerate after some time, and liquid accumulates at the edge of the sheet, creating a rim. This liquid accumulation is observed in Figure 24 (c) (t = 0.185 ms) and similarly in Figure 23 (b) (t = 0.18 ms). The ligament attached to the sheet becomes thick at t = 1.3 ms, and subsequently, it becomes Rayleigh-Plateau unstable, resulting in the droplet ejection from the edge of the sheet (t = 1.3 ms). A similar type of sheet breakup has also been reported in emulsion droplets [137] and water droplets [122].

5.2. Fragmentation of multicomponent liquids

The shadowgraph images of fragmentation of RME at various laser energies are shown in Figure 25. The RME has a higher viscosity and high absorption of laser energy compared to water and ethanol (see Table 1). Like water, air entrapment occurs at low incident laser energy (1.2 mJ). As seen in Figure 25 (a), when the laser pulse interacts with the droplet, the surface of the droplet ruptures and traps the surrounding air. The air bubble trapped inside the droplet (t = 0.45-0.63 ms) is not sufficient to completely fragment the droplet.

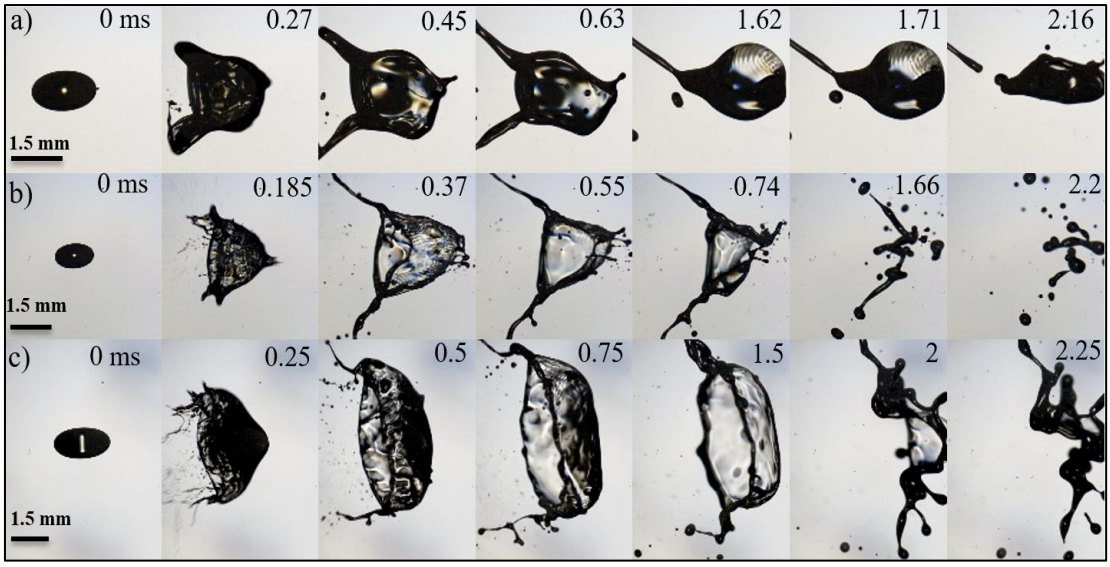

Figure 25. *Fragmentation of RME droplet at different laser energies: a) E_l = 1.2 mJ, D_0 = 1.4 mm b) E_l = 2.5 mJ, D_0 = 1.2 mm c) E_l = 7.15 mJ, D_0 = 1.8 mm*[129].

Two long ligaments are stretched out of the droplet at the upper and lower side, as seen at t = 0.63 ms. These two ligaments break into small droplets, and the remaining liquid collapses due to surface tension. As laser energy increases, sheet formation and its collapse occur (Figure 25 (b)-(c)), which leads to the creation of several secondary droplets. For the laser pulse energy of 2.5 mJ, RME (Figure 25 (b)) shows two long ligaments compared to water (in Figure 23 (b)) and ethanol (in Figure 24(a)) stretching from the liquid sheet. These ligaments later retract and form large secondary droplets of RME. In the case of ethanol, the length of these ligaments is very small, and thus smaller droplets emerge from the rim of the sheet. The higher viscosity of the RME acts as a damping force in the breakup of the ligaments. Therefore, despite the strong absorption of RME with the laser, the breakup strength is weak compared to ethanol and water.

Figure 26 shows the fragmentation of RE30 droplets for different laser energies. At lower laser energy of 0.5 mJ, the droplet undergoes fragmentation and is transformed into a sheet (Figure 26 (a)). The sheet experiences a reactionary thrust due to the fragmentation of the droplet. Subsequently, the sheet collapses under the influence of surface tension, and thick ligaments are created. These ligaments are prone to Rayleigh-Plateau instability and break into several secondary droplets. As the laser energy is increased (E_l = 1.2 mJ), it seems that the droplet fragments from both sides, due to which the residual droplet does not experience a reactionary

thrust force. Meanwhile, the air is trapped inside the residual droplet as seen in the oval-shaped droplet in Figure 26 (b) at 0.37 ms. The collapse of the residual droplet leads to the formation of relatively thin ligaments (0.74 ms) compared to the lower energy case (Figure 26 (a)). These ligaments further break into small-sized secondary droplets, as seen at 0.92 ms. The droplet fragmentation becomes more intense when the laser energy is further increased (E_l = 2.5 mJ). Moreover, no air entrapment occurs with a higher incident laser energy (Figure 26 (c)).

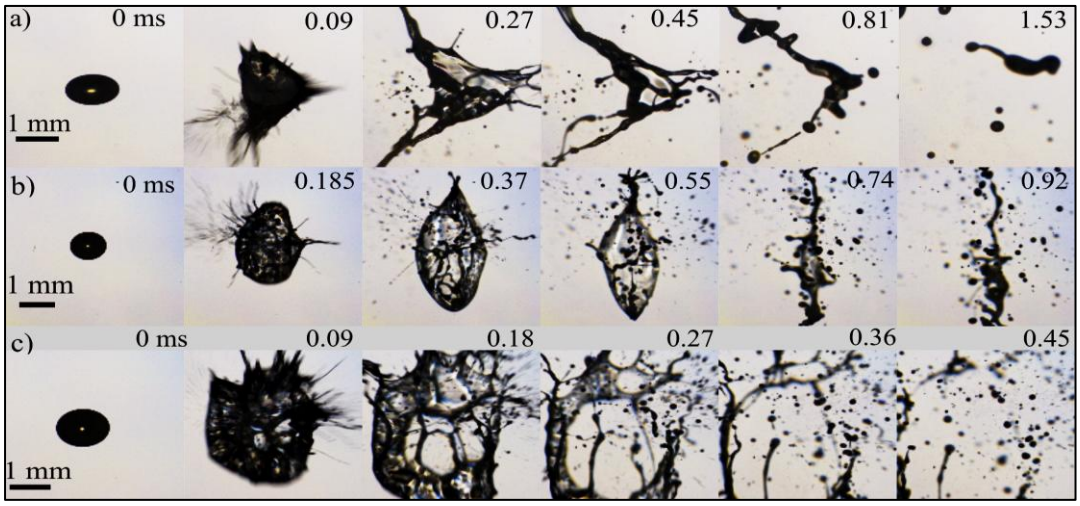

Figure 26. *Fragmentation of RE30 droplet: a) E_l = 0.5 mJ, D_0 = 1.1 mm b) E_l = 1.2 mJ, D_0 = 0.9 mm c) E_l = 2.5 mJ, D_0 = 1 mm*[129].

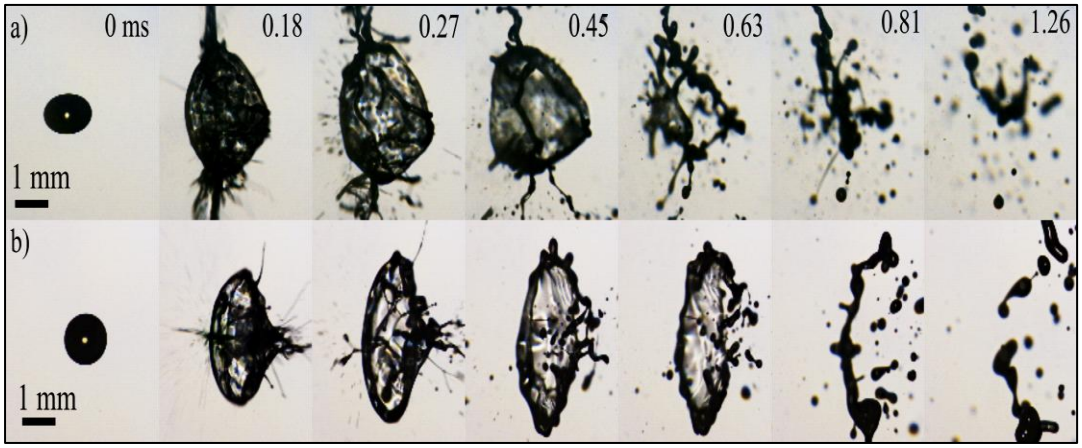

Figure 27. *Fragmentation of RE50 droplet: a) E_l = 0.5 mJ, D_0= 1 mm b) E_l = 2.5 mJ, D_0= 0.9 mm*[129].

Figure 27 shows the breakup of the RE50 emulsion droplet for different laser energies. Similar to RE30 emulsion, air entrapment occurs in the RE50 droplets that consequently collapse and produce thin ligaments and secondary droplets (Figure 27). It is observed that the RE30 droplets exhibit more intense

fragmentation compared to RE50, which can be attributed to its higher absorption to 532 nm laser compared to RE50.To understand the influence of the size of parent droplet on the breakup strength, the initial droplet size is reduced. Figure 28 (a) shows unstable prompt fragmentation in RE30 (D_0 = 0.6 mm), where sheet formation occurs, which ruptures and fragments into fine droplets. The secondary droplets produced are in the range of ~ 15-60 µm. When the size of the parent droplet is further reduced (D_0 = 0.25 mm), prompt fragmentation or catastrophic breakup occurs (Figure 28 (b)), where the droplet rapidly fragments into uniform-sized secondary droplets in the diameter range of ~ 15-20 µm. A vapor cloud is formed due to the intense bursting of the droplet (t = 0.18 ms). The secondary droplets produced due to catastrophic breakup are very small compared to the modes of breakup discussed earlier. This breakup mode is observed for small-sized parent droplets and high laser energies. Catastrophic breakup is not observed at low laser energies even for small-sized droplets.

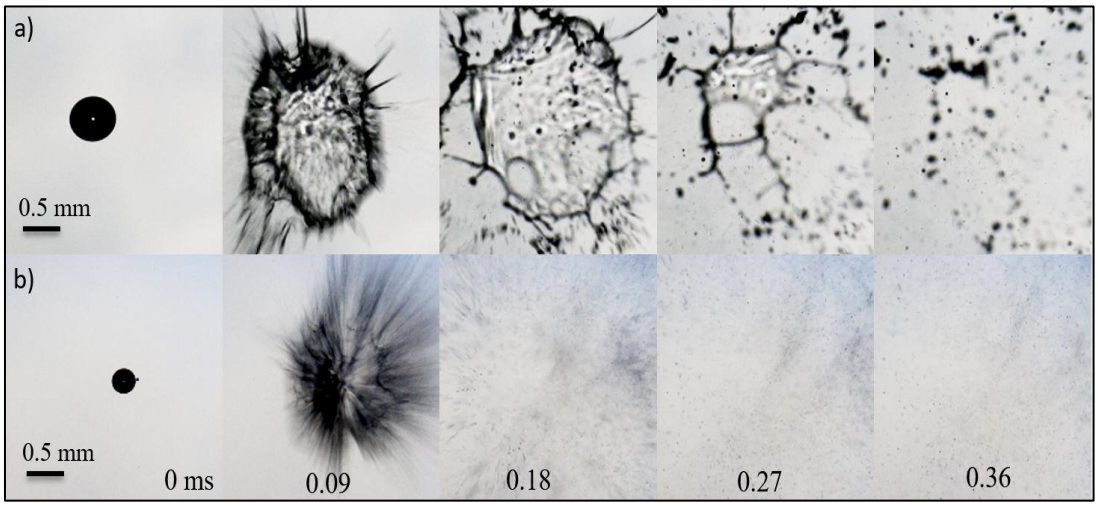

Figure 28. *Fragmentation of RE30 droplet at E_l = 2.5 mJ: a) Unstable prompt fragmentation (D_0= 0.6 mm) b) Prompt fragmentation (D_0 = 0.25 mm)*[129].

5.3. Ligament analysis and secondary droplet distribution

As discussed in earlier sections, the breakup of droplets leads to the formation of ligaments, which subsequently undergo breakup via Rayleigh-Plateau instability. When a ligament extends out of the fragmented droplet, necking on the ligament

leads to a pressure surge, and the continuous decrease of the neck radius results in the detachment of the tip from the ligament. The pinch-off of these ligaments can be compared to the ubiquitous capillary-driven jet breakup [21]. In the present work, the ligaments having an aspect ratio larger than π (~3.14) were observed to undergo pinch-off, which affirms that the ligament breakup occurs via the Rayleigh-Plateau instability. A similar observation has been reported in acoustically levitated evaporating as well as burning droplets[137,152,155]. The characteristic time scale associated with the ligament breakup (ligament breakup time) is estimated, and as expected, it is found to be longer for thicker ligaments. The ligament breakup time is the time at which the ligament originates until the last secondary droplet is separated from the ligament.

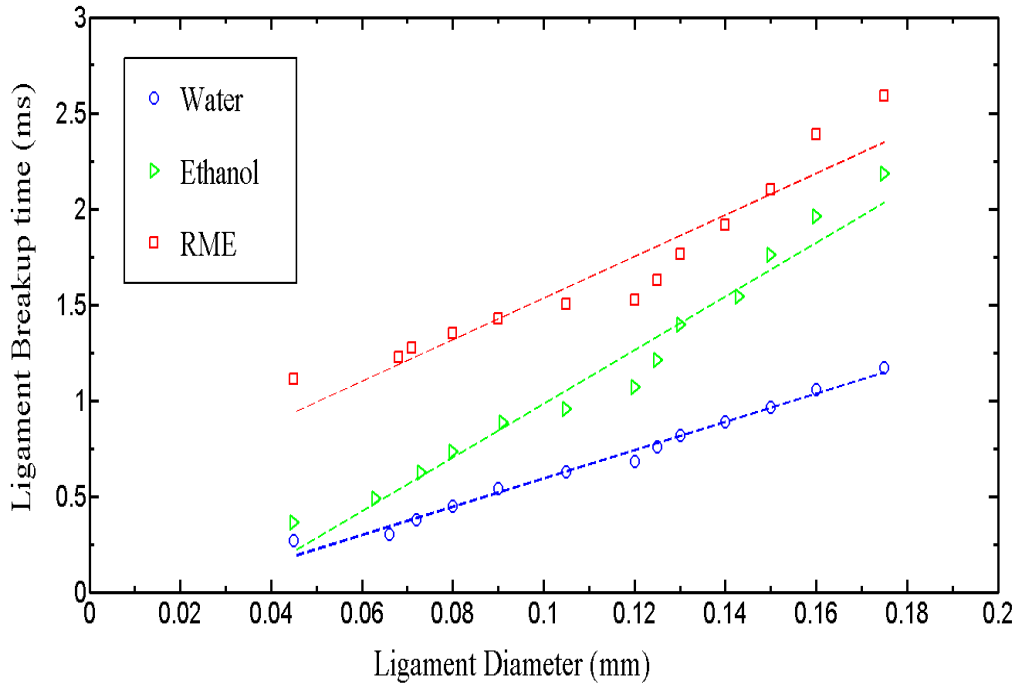

Figure 29. *Variation of ligament breakup time with ligament diameter for different liquids*[129].

Figure 29 shows the variation of ligament breakup time for different ligament diameters. Irrespective of the liquids, the ligament lifetime varies nearly linearly with its diameter. Since the ligament breakup is predominantly surface tension dominated, the breakup time of ligaments corresponding to water is significantly shorter than ethanol and RME. Moreover, the breakup time for the same ligament diameter is higher for RME compared to water and ethanol due to its higher viscosity (see Table 3). The diameter of secondary droplets is observed to vary

linearly with the ligament diameter for all the liquids, as seen in Figure 30 (a) and are found to be positively correlated (with a positive correlation coefficient of 0.87, 0.89, and 0.95 corresponding to water, ethanol, and RME, respectively). The correlation coefficient indicates the linear dependence between ligament diameter and secondary droplet diameter.

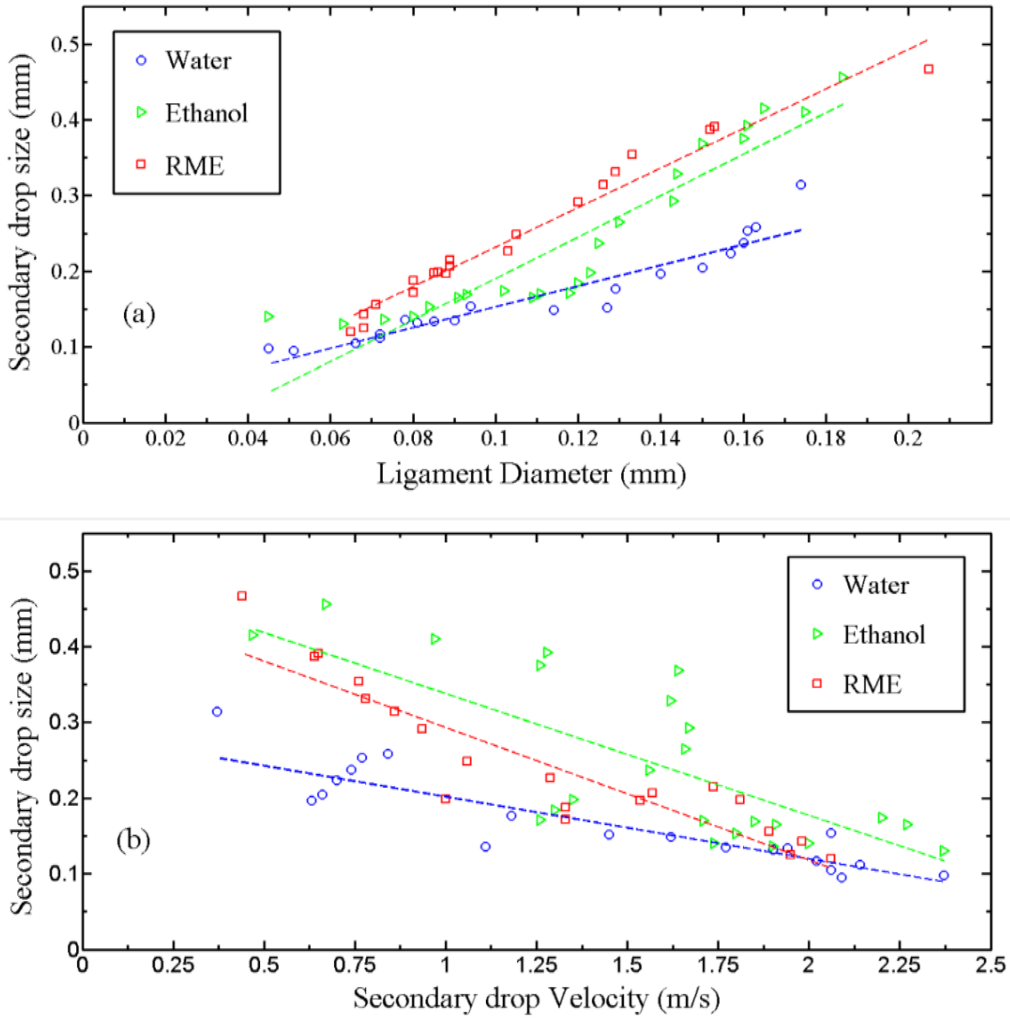

Figure 30. *Variation of secondary drop size with (a) Ligament diameter and (b) secondary drop velocity*[129].

The Pearson correlation coefficient[154] can be expressed as

$$\mathrm{Correl}(D_L, D_S) = \frac{\sum(D_L - \bar{D}_L)(D_S - \bar{D}_S)}{\sqrt{\sum(D_L - \bar{D}_L)^2 \sum(D_S - \bar{D}_S)^2}} \,. \qquad (5.1.2)$$

where $\bar{D}_L$ and $\bar{D}_S$ are the average ligament diameter and average secondary droplet diameter, respectively. Similarly, as the size of the secondary droplets increases, the corresponding velocity decreases (Figure 30 (b)), indicating the secondary droplet

size and the corresponding velocity are negatively correlated (correlation coefficient ~ -0.8, -0.67, and -0.91 corresponding to water, ethanol, and RME, respectively).The experimental ligament breakup timescale (τ_b) can be compared with the theoretical capillary time ($\tau_c = \sqrt{\rho_l D_L{}^3/\sigma_l}$), where D_L is the diameter of the ligament, ρ_l is the liquid density, and σ_l is the liquid surface tension. It is found that the experimental timescale of ligament breakup and the capillary timescale are of the same order except for RME, where viscosity seems to play a role in inhibiting the breakup of the ligament. From Table 3, the predictions of the capillary time are consistent with the experimental ligament breakup time, while the pre-factors are not. RME has higher pre-factors than water and ethanol, indicating viscosity effect.

Table 3. *Essential characteristics of the ligament and ejected secondary droplets for liquids*[129].

Liquids	**Ligament Diameter, D_L (mm)**	**Secondary Drop size, D_s (mm)**	**Ligament Breakup time, τ_b (ms)**	**Capillary Time, τ_c (ms)**	**Pre-factor, τ_b/τ_c**
Water	0.065	0.094	0.27	0.062	4.30
	0.08	0.116	0.36	0.085	4.22
	0.11	0.143	0.63	0.142	4.42
	0.125	0.207	0.72	0.167	4.30
	0.15	0.234	0.92	0.214	4.28
	0.17	0.314	1.17	0.268	4.35
Ethanol	0.065	0.12	0.36	0.052	6.92
	0.08	0.129	0.74	0.080	9.23
	0.11	0.154	0.9	0.121	7.39
	0.125	0.247	1.3	0.145	8.94
	0.15	0.34	1.85	0.191	9.68
	0.184	0.456	2.59	0.259	9.97
RME	0.065	0.12	1.11	0.057	19.18
	0.08	0.187	1.26	0.079	15.94
	0.11	0.247	1.48	0.118	12.45
	0.125	0.306	1.66	0.156	10.62
	0.153	0.374	2.4	0.208	11.48
	0.205	0.467	2.7	0.324	8.33

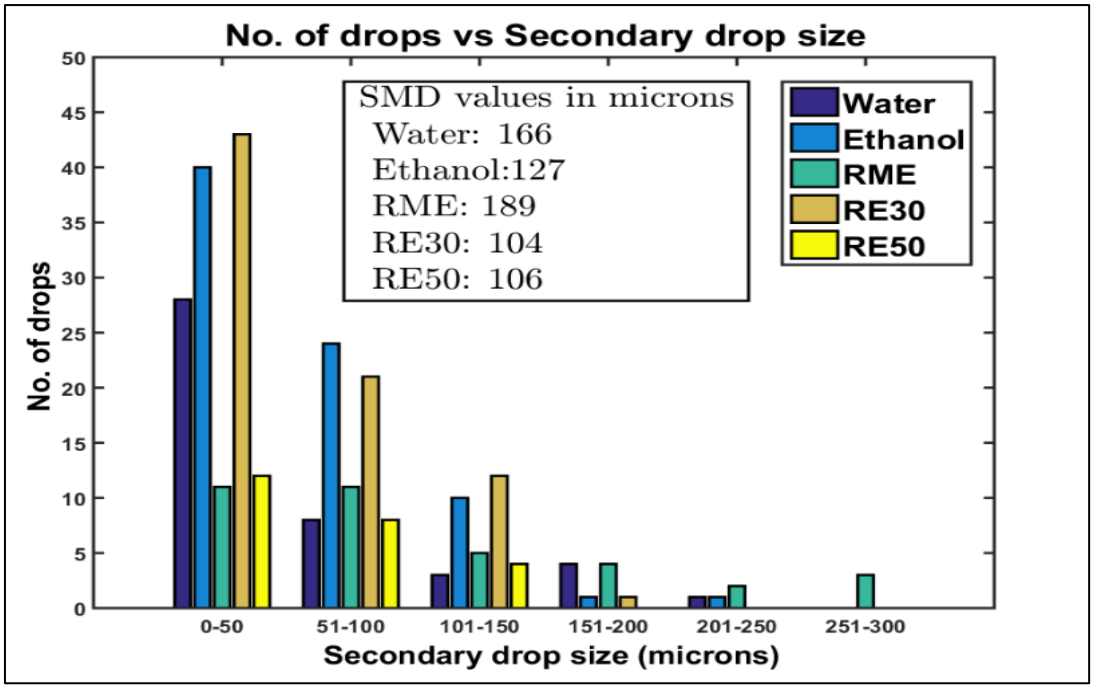

Figure 31. *Number of drops plotted against the secondary droplet size at E_l = 5.3 mJ, D_0 ~ 1.2 mm for different liquid droplets water, ethanol, RME, RE30, and RE50*[129].

Figure 31 shows the Sauter Mean Diameter (SMD) of the secondary droplets produced from the breakup of the parent droplet due to laser pulse. SMD indicates the mean diameter of an ensemble of droplets with the same volume to surface area ratio. Here, the size distribution is calculated from the shadowgraph images, and the secondary droplet sizes of the eccentricity of 0.75 to 1.0 were considered for SMD calculation. A higher SMD indicates the creation of large-sized secondary droplets from the fragmentation of parent droplet. The SMD is calculated as [3]

$$\mathrm{SMD} = \frac{\sum_{i=1}^{\infty} n_i * {d_i}^3}{\sum_{i=1}^{\infty} n_i * {d_i}^2} \qquad (5.1.3)$$

where d_i is the diameter of the i^{th} droplet and n_i is the number of the i^{th} drop. It is observed that the emulsion droplets have lower SMD values than RME and the single-component fuel droplets. The SMD of 189 µm for RME is observed at 5.3 mJ, D_0 = 1.2 mm. The secondary droplet size produced for RME fuel is in the range of ~15-400 µm at 2.5 mJ and ~15-300 µm at 5.3 mJ energy. For ethanol fuel, the SMD is ~13-300 µm at 2.5 mJ and ~13-220 µm at 5.3 mJ. The relation of calculated SMD for the different fuel droplet is $SMD_{RE30} < SMD_{RE50} < SMD_{Ethanol} < SMD_{Water} < SMD_{RME}$. The droplet of an emulsion of RME and ethanol shows a higher intensity fragmentation compared to pure RME or ethanol droplet even at lower

laser pulse energies. As discussed earlier, the higher viscosity of RME dampens the ligament-mediated breakup and inhibits the efficient atomization of RME droplets. Pure ethanol droplet exhibits stable sheet fragmentation at a laser energy of 2.5 mJ (see Figure 24 (a)) with secondary droplet diameters in the range of 60-100 µm. At the same laser energy, RE30 emulsion droplet exhibits complete disintegration of the droplet (see Figure 28 (c)), resulting in secondary droplets of a diameter less than 50 µm. A higher percentage of ethanol in RE50 does not improve the droplet disintegration due to its lower laser absorption compared to RE30.

5.4. Overview of the nanosecond laser study

In Figure 32, a comparison between different laser-induced breakup modes for the fuel droplets with respect to the laser pulse energy is presented. The ratio ($\bar{D}_S/D_0$) provides information about the average diameter of all secondary droplets generated to the initial onset droplet diameter. The different modes of breakup are categorized based on the measurement of droplet size and image analysis. This ratio indicates the strength of the breakup, which results in deformation or complete explosion of the drop. The type of breakup mainly depends on the laser energy supplied, initial droplet size, and properties of the fuel.

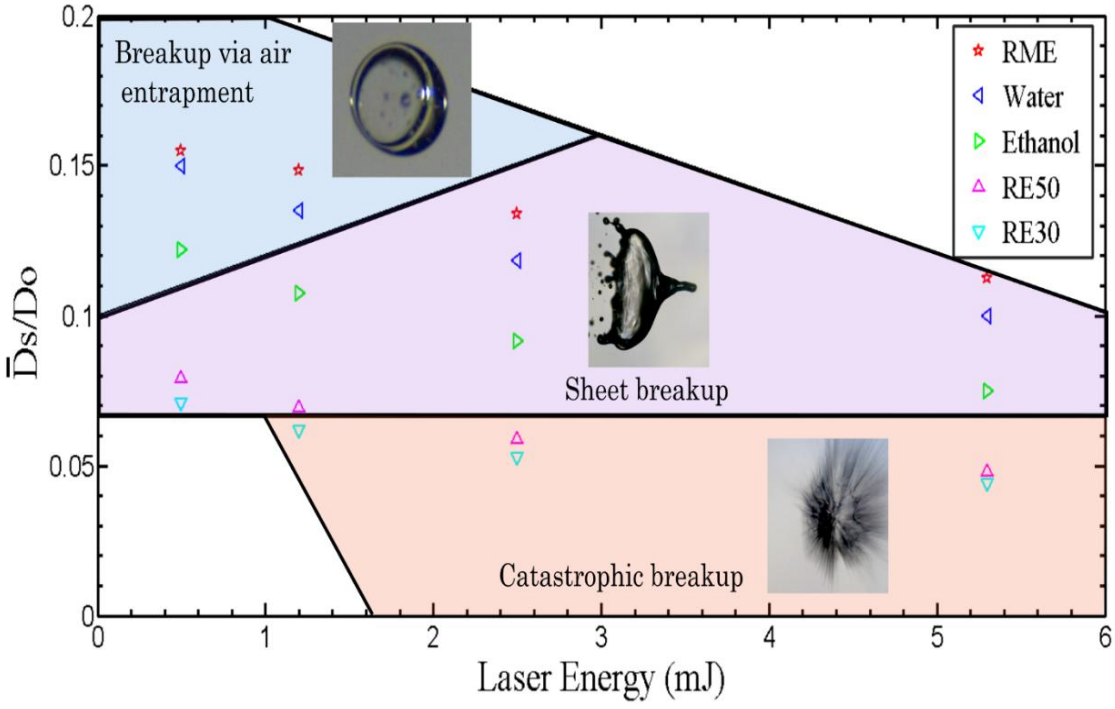

***Figure 32**. Overview of nanosecond laser-induced fragmentation for different liquid droplets*[129].

As mentioned earlier, the breakup modes are categorized into three categories: droplet breakup followed by air entrapment, sheet breakup, and catastrophic breakup. At lower energies and larger droplet sizes, rupture of droplet followed by air entrapment is observed, resulting in $(\bar{D}_S/D_0) > 0.1$. As the laser energy is increased for the same initial diameter of the droplet, sheet breakup and catastrophic breakup are observed for $(\bar{D}_S/D_0) < 0.1$. Furthermore, as seen in Figure 32, catastrophic breakup occurs primarily for higher laser energies (> 1.2 mJ).

5.5. Summary

In summary, this chapter examines the fragmentation behavior of droplets induced by nanosecond laser breakdown, focusing on single-component liquids, biofuels, and their emulsions, and employing high-speed imaging to capture the temporal progression of these processes. For single-component droplets, fragmentation occurs predominantly through low-strength air entrapment and sheet breakup mechanisms. In contrast, biofuel emulsions exhibit a higher resistance to fragmentation, demonstrating greater breakup strength. The study finds that prompt fragmentation becomes more prevalent as droplet size decreases, emphasizing the role of droplet scale in determining breakup dynamics. Ethanol, compared to water, shows significantly higher breakup strength, attributed to its superior light absorption properties, which enhance its interaction with the laser. On the other hand, rapeseed methyl ester (RME), a common biofuel, demonstrates a different behavior; its higher viscosity mitigates ligament-mediated breakup, despite its strong light absorption. Ligament formation and dynamics are observed to scale linearly with diameter across all tested liquids. RME, however, exhibits an order of magnitude higher breakup time, indicating its unique fragmentation characteristics under these conditions.The analysis also reveals a relationship between breakup strength and secondary droplet size. RME and its emulsions produce finer atomization, resulting in smaller secondary droplets and reduced Sauter mean diameter (SMD) values. Adding ethanol to RME further enhances atomization efficiency, leading to the formation of even smaller secondary droplets. These findings highlight the potential of RME emulsions to achieve efficient and fine atomization, positioning them as a promising alternative fuel source.

Overall, the chapter provides valuable insights into the atomization behaviors of biofuels, emphasizing the nuanced roles of viscosity, light absorption, and emulsion composition in shaping fragmentation and atomization. These findings are significant for optimizing biofuel performance in combustion devices, offering a pathway for improving efficiency and sustainability in energy applications.

6. Ultraviolet-Nanosecond laser induced breakdown in liquid droplets

In this section, we delve into the dynamics exhibited by various droplets when subjected to irradiation by a nanosecond laser with a ultraviolet wavelength of 266 nm. The laser energy of 20 mJ per pulse at this wavelength predominantly induces plasma generation within the droplet, a phenomenon discussed in the following sections. The ensuing opto-hydrodynamic behavior during the laser pulse-droplet interaction is contingent on the energy absorption characteristics. The dynamics of the droplet during this interaction are primarily dictated by the energy distribution of the incident laser and the properties of the liquid droplet. Upon focusing the laser within the droplet, a fraction of the energy is absorbed by the droplet, while the remainder is transmitted. The absorbed energy initiates plasma formation, leading to simultaneous expansion and fragmentation of the droplet. The residual energy is carried away by the ensuing shock wave. This study omits consideration of energy losses attributed to radiation, reflection, and scattering, given that their combined contribution has been reported to be less than one percent of the incident energy[28,156]. In our experiment, we exercised control over the location and mode of optical breakdown, influencing the direction of sheet formation or the propulsion of fragments. It became evident that the mode of optical breakdown underwent variations based on the properties of the liquid. Regardless of the specific breakdown mode, our observations indicate that the effective breakup of the target droplet occurs when most of the absorbed energy is dedicated to the process of droplet fragmentation. This typically results in the rapid formation of a thin sheet, which subsequently undergoes a swift collapse. The intricacies of these phenomena underscore the importance of fluid properties in shaping the dynamics of optical breakdown and subsequent droplet breakup. The liquid properties play a vital role in driving the fragmentation mechanisms for the hydrocarbon droplets.

6.1. Plasma formation and Shock wave dynamics

Figure 33 shows the bright spot in the droplet due to plasma formation (left image) and the shock wave (right image) indicated as the dim ring. Propagation of an expanding shock wave and vapor mist behind the drop is observed in Figure 33 (b). The expansion velocity of the shock wave is approximately 760 ± 50 m/s with corrections made for the geometrical distortion arising from the curvature of the drop, as reported by Kobel *et al.*[157]. This correction accounts for the specific geometric considerations, ensuring accurate measurements of the shock wave dynamics. This section highlights the comprehensive visual depiction of the dynamic interplay of optical breakdown, shock wave dynamics, and plasma-induced droplet fragmentation in a droplet. This provides valuable insights into the intricate phenomena occurring within the droplet under the influence of focused laser pulses. When a laser pulse is focused inside a droplet, optical breakdown occurs. This laser-induced breakdown initiates the radial outward movement of both plasma and shock waves, with multiple shock waves occurring in the case of multi-mode breakdown. The plasma and shock wave exhibit simultaneous motion for a duration of a few hundred nanoseconds, depending on the pulse energy. Following this period, the shock wave separates from the plasma, carrying away a significant portion of the absorbed energy[158,159].

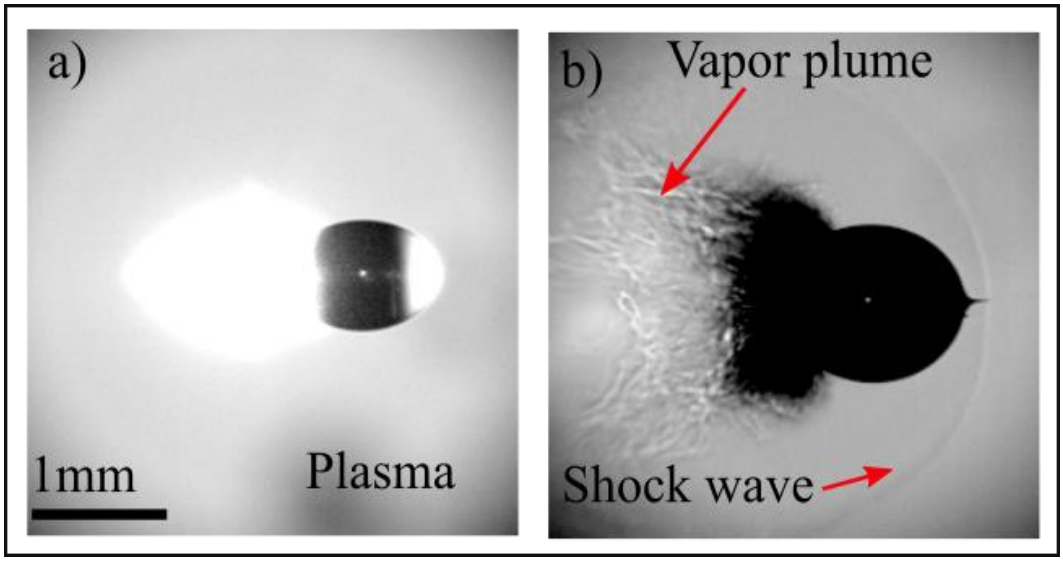

Figure 33. *Plasma and shock wave generation dynamics during laser droplet interaction.*

Consequently, the remaining energy within the plasma contributes to the breakup of the droplet, leading to the generation of fragments that move radially outward behind the shock wave. The shock wave is accompanied by the presence of a vapor plume and a mist cloud of vapor and droplets. This mist cloud is observable as a gray-to-black haze. Fragments are propelled just behind the shock wave for a short period. The white spot observed at the droplet corresponds to the high-temperature plasma, which is visible in the image. As the shock wave travels into the air, leading to pressure increases behind it. A close examination of the sheet's surface in Figure 35 (a) reveals a structure indicative of a Kelvin–Helmholtz instability.

6.2. Expansion dynamics

The expansion of the droplet after the laser pulse impact is discussed in this section. The stationary spherical droplet of radius R_0 in a quiescent environment e.g. levitator (considering the minimal effect of radiation force on the droplet, it does not change the acoustic frequency) keeps its original shape. After the laser impact, expansion occurs, and the radius of the droplet R(t) increases with time from R_0 to R_{max} and subsequently, it accelerates from u_0 to u. Considering the correction of $F(u_0, t, \sigma, \dots.)$, expanding radius can be rewritten as [53]

$$R(t) = R_0 = F(u_0, t, \sigma, \dots.). \quad (6.2.1)$$

When the droplet expands, its radius increases and reaches maximum expansion ($R_{max} \gg R_0$). Subsequently, the sheet thickness h decreases i.e. the aspect ratio h/R_{max} is very small. Thus, the dependent functions for radial velocity and thickness of the expanding drop are $u(R,t)$ and $h(R,t)$ respectively. By considering the slender slope approximation ($|\partial_R h(R,t)| \ll 1$), Euler equation can be written as

$$\rho(\partial_t u + u\partial_R u) = -\partial_R P, \quad (6.2.2)$$

$$R\partial_t h + \partial_R(uhR) = 0, \quad (6.2.3)$$

where $P(R,t)$ is the pressure in the liquid. R=R(t) radius of the expanding sheet which varies with time. There is no interaction with the surrounding gases.

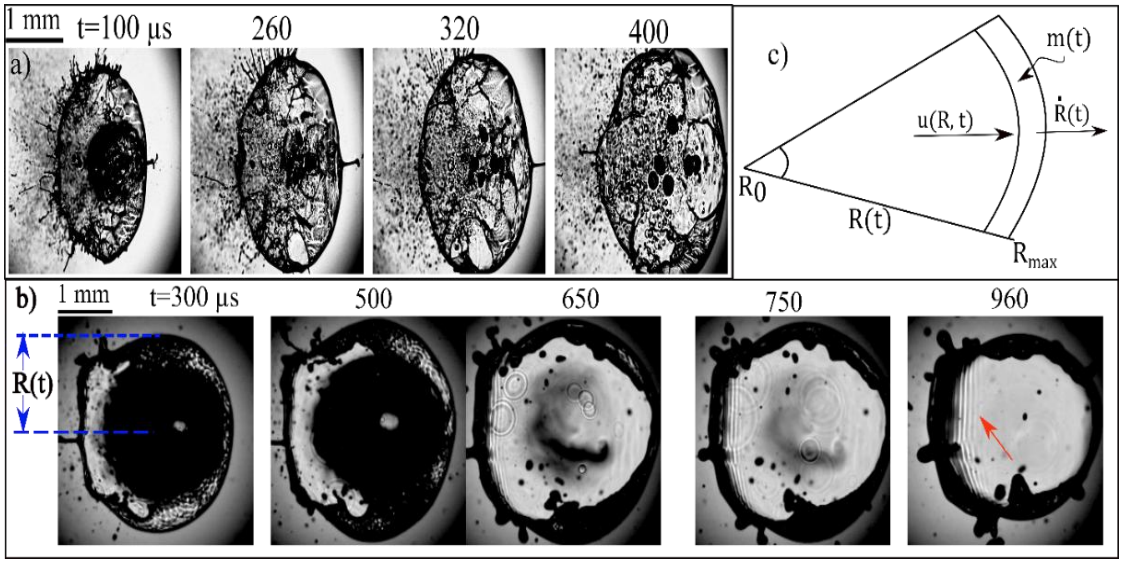

Figure 34. *Expansion dynamics: a) Vertical stretching and radial expulsion from the sheet edge b) Expansion of the sheet and gradual accumulation of liquid at the rim, the red arrow indicates the perturbations near the rim edge, c) A depiction of the rim with mass per unit arclength, denoted as m(t), attached to the sheet represents the sheet's outer edge with varying distribution of mass along its circumference. The sheet having a mass per unit arc length m (t), velocity u (r, t), and radius R(t) used for mass and momentum balances*[53].

The mean radius of the sheet expands until reaching a maximum value, denoted as R_{max}, depends on u_0, and the corrugation of the sheet rim. These undulations serve as the foundation for radial ligament formation. As the sheet expands, a hole originates. This hole extends to the corrugated rim, leading to the breakup of the ligaments and the formation of stable drops. The entire process, transitioning from the initial drop to stable fragments, completes shortly after the sheet rim begins to recede (i.e. when $\dot{R}(t) < 0$, where $\dot{R} = dR(t)/dt$). After the impact of the laser, the central liquid is fed to the sheet rim and the collection of radially fragmented particles at the rim by capillary wave action. The mass of liquid is transferred to the rim edge and concurrently rim becomes thick (Figure 34). By considering the initial volume of the drop $\alpha = \pi {D_0}^3/6$, the liquid volume constituting the sheet at time *t* is represented as [53]

$$\int_{R_0}^{R_{max}} 2\pi R h(R,t) dR = \alpha - \beta, \qquad (6.2.4)$$

where $\beta = \int_0^t [2\pi R(t)\{u(R,t) - \dot{R}\} h(R,t)]dt$ is the net volume accumulated at time t on the rim. When applying momentum conservation at the rim, we consider a system analogous to the propulsion concept given by Tsiolkovsky (1903)[160].

It states that the rate of change of the rim inertia is equal to the sum of the momentum it absorbs plus the net force acting on it [53] expressed as

$$\frac{d}{dt}\left(mR * \dot{R}\right) = \varphi u(R,t)R - 2\sigma(R - R_0), \tag{6.2.5}$$

$$\varphi = \rho h R[u(R,t) - \dot{R}], \tag{6.2.6}$$

$$\varphi = \frac{1}{R}\frac{d}{dt}(mR). \tag{6.2.7}$$

The velocity u (R, t) represents the liquid's velocity in the sheet at $R = R(t)$. The force term $2\sigma(R - R_0)$ refers to the initial drop with a radius R_0, which becomes zero when $R = R_0$. Equation (6.2.6) and (6.2.7) represent the conservation of the mass. The liquid pressure is considered to be the ambient pressure, independent of R. This assumption arises from neglecting interactions with the ambient medium and disregarding viscous stresses. Additionally, there is a correction, accounting for the curvature of the liquid interface as per Laplace's law. While this curvature is weak and diminishes over time for most of the radial curvature, it is more significant at the sheet rim ($R < R(t)$), where it is approximately of the order $\partial^2 h/\partial^2 R = \alpha/R^4$. The interface dissipates energy, the internal pressure is not expected to significantly increase compared to its value in the quasi-planar sheet. Thus, the pressure in the liquid remains nearly constant along R. By considering the velocity conservation and neglecting pressure gradients, the modified equation for the radius of the expanding sheet is expressed as

$$\ddot{R} + \frac{6}{(\tau_c - t)^2}(R - R_0) + \frac{4}{\tau_c - t}\dot{R} = 0. \tag{6.2.8}$$

Equation (6.2.8) reveals that the nonlinear dynamics of equations (6.2.1) and (6.2.2) lead to a linearly damped oscillatory motion of the sheet radius. This motion is characterized by a time-dependent frequency and damping factor, representing a balance between the initial drop's inertia and capillary restoring forces per Culick's law. The damping term arises from the ongoing transfer of momentum from the sheet to the rim. For the initial case, $R(0) = R_0$ and $\dot{R}(0) = u_0$, the radius of the expanding drop is modified as[53,54,110]

$$\frac{R(t)-R_0}{R_0} = \sqrt{\frac{2\,We_d}{3}}\,\frac{t}{\tau_c}\left(1-\frac{t}{\tau_c}\right)^2. \qquad (6.2.9)$$

This explains an asymmetric on-period oscillatory motion that fits well for various Weber numbers and has a duration of the period $\tau_c = \sqrt{\rho {D_0}^3/6\sigma}$. The rescaled Weber number, $We_d = \frac{E_{k,d}}{E_{k,p}}\,We$ depends on the kinetic energy used for deformation which is expressed as the ratio of deformation to propulsion kinetic energies and corresponding Weber number [55].

6.3. Fragmentation of Iso-octane droplet

Figure 35 displays the time sequences showing the different dynamics of laser-induced fragmentation of iso-octane droplets at different laser energy levels. The complete atomization of the iso-octane droplet is depicted in Figure 35 (a). The droplet is fragmented into a cloud of fine secondary drops. The droplet deformation and ligament-mediated breakup are shown in Figure 35 (b). One thick long ligament is formed which breaks due to instability. Figure 35 (c-d) presents time sequences of the dynamic evolution of the hole expansion and merging processes. This visual representation captures the successive stages in the behavior of the holes, including their expansion, the formation of rims, the merging of holes or interaction with straight rims, the emergence of quasi-symmetric liquid bridges, and the subsequent stretching and detachment into ligaments. Capillary and surface waves with the growth of the single hole on the sheet are observed in Figure 35 (c). The merging of multiple holes and their growth is shown in Figure 35 (d), which subsequently breaks the thin sheet, whereafter several secondary droplets are produced. Liquid accumulation at the edges of the circular sheet makes the rim thicker causing them to collapse under the influence of surface tension, as observed in Figure 35 (e). The detailed laser-induced dynamics of hydrocarbon droplets are discussed in the following subsections.

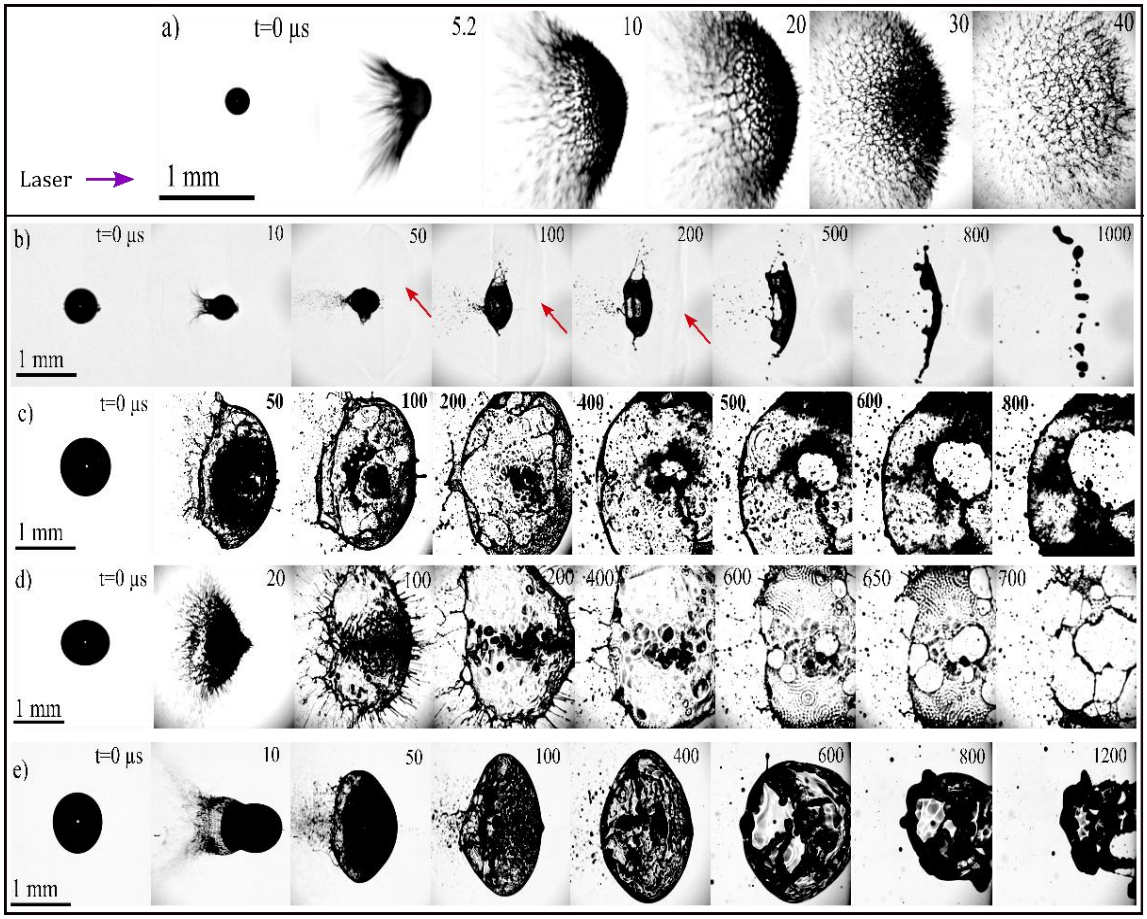

Figure 35. *Overview of laser-induced fragmentation processes of iso-octane droplets; a) Complete atomization of the droplet, D_0= 0.2 mm, E_l = 20 mJ; b) Ligament mediated breakup of iso-octane, D_0= 0.35 mm, E_l = 12 mJ; c) Sheet breakup through single hole formation within a droplet, D_0= 0.55 mm, E_l = 17 mJ; d) Sheet breakup of droplet through multiple holes merging, D_0= 0.54 mm, E_l = 20 mJ; e) Stable sheet collapse of a droplet, D_0= 0.54 mm, E_l = 17 mJ.*

6.3.1. Complete atomization

The later dynamics of fragmenting droplets are illustrated in Figure 35 (a). Droplet initially undergoes rapid fragmentation, resulting in the formation of a cloud of fine droplets. The smaller droplets, expelled first, are predominantly situated on the left side of the droplet. The brief duration required for the completion of the fragmentation process distinguishes this regime from the other. The small fragments are ejected at t= 10 µs, after the rupture of the droplet wall. These fragments travel initially at a speed of 680 ± 50 m/s. The speed of the fragments is almost four times faster than the speed of the sound in air at 293 K and 1 atm. We can estimate the maximum size of these fragments by considering the capillary length, λc_f, where the surface tension can counteract the acceleration experienced

by the fragments (a_f). It is observed that fragments achieve a velocity of about 380 m/s within 10 µs. Fragments experience an initial acceleration on the order of 10^8 m/s^2. From this, we can estimate the size of the stable fragment d_f as

$$d_f < \lambda c_f = \sqrt{\sigma/\rho\, a_f}, \qquad (6.3.1)$$

where ρ = 880 kg/m^3 and $\sigma = 0.025$ N/m are the density and surface tension of the liquid respectively. Hence, droplets with a diameter exceeding 1 µm are unable to withstand the extreme acceleration, resulting in the blurred appearance of the fragments near the shock front. Due to the limitations of the current experimental setup, these finer details couldn't be resolved. The overall shape of the fragmenting droplet shown in Figure 35 (a) is discussed in this paragraph. Initially, the right side of the droplet appears smooth, while the left side exhibits a rough surface with a complex pattern. These patterns manifest rapidly as the side expands towards the left. The sheet expands quickly after t = 5 µs, becoming apparent again at t = 10 µs. This suggests that the sheet undergoes significant shear forces between the relatively still air surrounding the droplet and the outflow from the vaporous explosion. A Kelvin–Helmholtz instability is likely at play in this regime, which is supported by additional experiments. These experiments reveal that, despite being highly corrugated, the sheet remains intact, with the dark structures representing crests of wavy corrugation on the sheet. Fragmentation delay with gradually increasing surface roughness is observed on the right side of the droplet. The wavelength of these structures is significantly smaller than the structures observed in the expanding sheet. The drop continuously deforms and is subsequently fragmented as characterized by a thinner leading edge at t = 30 µs. During the stage of deformation of the droplet, the small threads-like structure of the liquid on the drop surface is observed on the right side at t = 20 µs. We assume that numerous interactions between multiple waves and the droplet surface take place before the liquid film ruptures. This may be due to cavitation on the droplet surface. Impulsive acceleration of a free surface results in the generation of fast liquid jets from a curved surface[7,161,162]. The fragments are ejected initially at a very high speed and rapidly decelerate to 490 m/s after t = 15 µs. A similar study[7,122] has been reported for high velocities of the ejected fragments from the laser-induced cavitation bubbles near a curved free surface.

6.3.2. Droplet deformation and propulsion

The laser-produced plasma light source used in extreme ultraviolet (EUV) nanolithography extensively uses the laser-induced breakdown (LIB) phenomenon. The droplet deformation and its propulsion were previously reported by Klein *et al.*[55]. They observed that the primary driving force behind the observed drop propulsion and deformation is the localized and asymmetric boiling of the liquid, triggered by the absorption of laser energy on the illuminated side of the drop. The absorption of laser energy depends on fluid and laser properties. The resulting vapor recoil pressure is responsible for the deformation and propulsion of the drop (Figure 35 (b)). The absorbed laser energy E_{ab} and threshold energy E_{th} required for a liquid layer to achieve the boiling point, so the propulsion velocity V can be obtained as[55]

$$V \sim \frac{E_{ab} - E_{th}}{\rho \, R^3{}_0 \, \Delta H} \, u_T, \tag{6.3.2}$$

where ΔH is the latent heat of vaporization, $u_T = \sqrt{K_B T_b / M}$ is the thermal speed of the expelled vapor, K_B is the Boltzmann constant, and M is a molecular mass. From Figure 35 (b), the vapor plume is visible around the droplet and travels in the outward direction represented by the red arrow. This resembles that the evaporation occurs during the energy transfer process. The latent heat of vaporization of iso-octane is very low, which means that early phase change occurs for iso-octane. Along with the vapor plume, a little fine mist is coming out at the proximal side of the droplet. Therefore, the laser energy absorbed by the superficial layer of the iso-octane is sufficient to reach its boiling point. The droplet deforms in the vertical direction and subsequently, it propels forward. The subsequent vertical stretching of the droplet forms one thick long ligament. The ligament breaks into secondary droplets due to RT instability (at t=1000 μs). The lateral expansion of the drop is correlated with the drop propulsion as [53]

$$\frac{R(t) - R_0}{R_0} \sim We^{1/2} \sim \sqrt{\frac{\rho R_0}{\sigma}} \, \frac{E_{ab} - E_{th}}{\rho \, R^3{}_0 \, \Delta H} \tag{6.3.3}$$

where the Weber number is written as $We = \rho R_0 V^2/\sigma$. Therefore, both the propulsion speed and the maximum radius of expansion are directly proportional to the energy of the laser pulse. The comparison of the maximum relative expansion and Weber number is shown in Figure 36. It shows a best-fit power-law curve based on the average data points for the maximum sheet radii, which compares the square-root exponent of the Weber number (We) as predicted by Eq. (6.3.3). The solid blue line represents the best-fit curve, capturing not only the scaling dependencies [given by Villermaux and Bossa and Gelderblom *et al.*] but also providing a quantitative fit for the average data points. The curve demonstrates a strong correlation with the square-root dependence on the Weber number, particularly at lower and intermediate We values, thus accurately describing the sheet expansion behavior in these regimes. From equation 6.3.2, it is clear that propulsion is dependent upon energy applied and threshold energy. It indicates that when both energies are equal, propulsion is zero. When applied energy greater than threshold energy, we could see some propulsion. Therefore, to get propulsion specific amount of laser energy is required, here it is called threshold energy. Also, the formation of the mist along with the vapor plume indicates that the superficial layer of the droplet reaches the boiling point of liquid. It is an indicative of how much energy is absorbed by the droplet. Fig.35 (b) is the condition zero case where we start to observe the mist and vapor plume which is at 12 mJ laser energy. Below this laser energy, we did not observe mist and vapor cloud, but we observed little propulsion (see insets in Fig.36). From inset in Fig.36, the significant propulsion is observed above 10 mJ and more pronounced at 12 mJ laser energy. Therefore, the threshold energy required for propulsion is approximately 10 mJ, where we see significant propulsion of the droplet. Figure 36 represents the maximum expansion of the droplet with the corresponding Weber number. Theoretically, equation 6.3.3 shows the dependency of the sheet's expansion radius on the applied laser energy and threshold energy. The higher the laser energy, the greater the expansion and propulsion, resulting in a higher Weber number. The inset in Fig. 36 depicts the variation of propulsion speed with the function of the laser energy applied. Here, the propulsion speed is measured experimentally with respect to the laser energy applied. Hence, it indicates how much the droplet is propelled by different laser energies. As the laser energy increases, the propulsion speed of the droplet also increases.

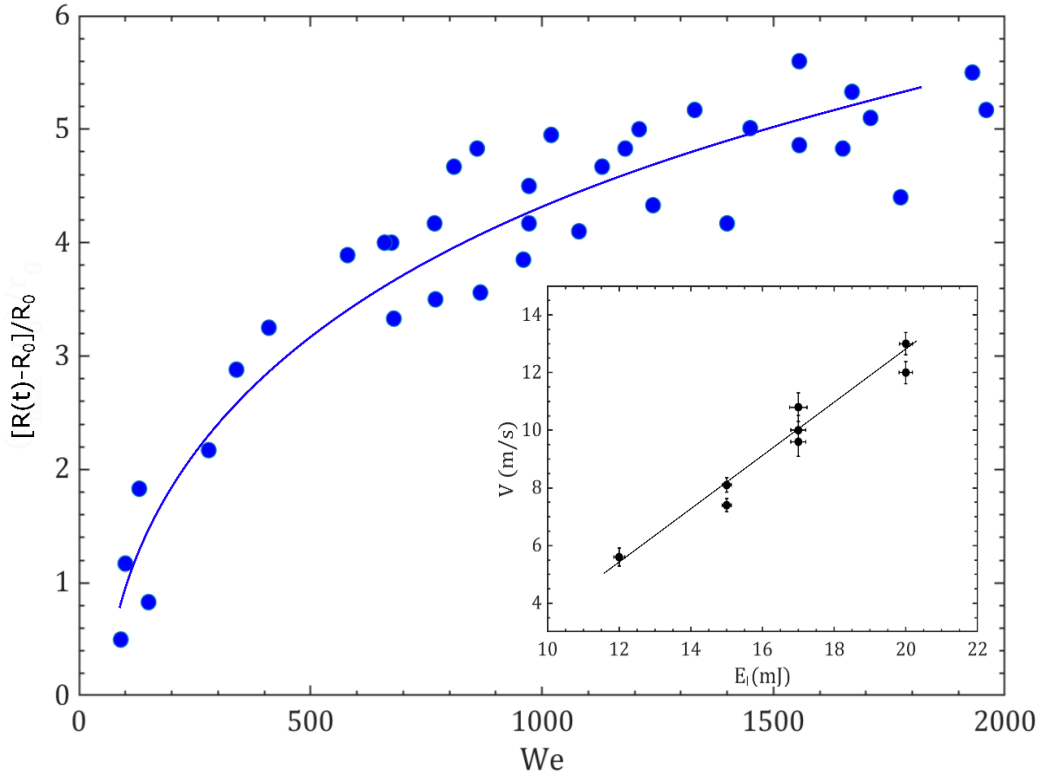

Figure 36. *Maximum expansion of the droplet as a function of the Weber number (We). The solid line represents the cubic fit with a pre-factor of 0.8. The inset represents the variation of the propulsion speed as a function of laser energy. (The solid line is linearly fitted with a pre-factor of 0.6.)*

6.3.3. Sheet breakup through hole formation

The high-speed shadowgraph images offer valuable insights into the liquid sheet's characteristics and show qualitative features such as radial instability waves, capillary waves, hole formation, and its growth, regions of breakup marked by ligaments, and the formation of secondary droplets. Two distinct scenarios are observed: hole–rim merging, corresponding to the interaction involving a single hole in a confined thin liquid sheet (Figure 35 (c)); and hole–hole merging (Figure 35 (d)), representing the dynamics involving two distinct holes in a thin liquid sheet. In both the hole–hole and hole–rim cases, the initial stages involve the expansion of the holes, leading to the formation of rims at their free ends. These rims can either merge with each other or with a sheet's rim, particularly in the case of a bounded liquid sheet. Following this process, a quasi-symmetric liquid bridge

emerges, connecting the two holes or the hole and the sheet rim. This characteristic liquid bridge is prominently visible in the seventh image of both Figure 35 (c) and Figure 35 (d). As time progresses, the liquid bridge undergoes stretching, concurrently with the continuous growth of the resulting hole after merging. Subsequently, the liquid bridge detaches into a ligament, characterized by blobs formed at its tips. This ligament, depending on its dynamics, has the potential to break into smaller droplets or recoil, ultimately forming a single, larger droplet.

The processes highlight the complex and dynamic nature of the liquid sheet evolution after the merging of holes in various configurations. The dimensions of the rim at the onset of the merging process between two holes are identical to the sheet rim. However, in the case of the hole rim, the size of the connecting rim increases. Notably, during hole–hole merging, the liquid bridge remains straight, while in hole–rim merging, it exhibits an outward curvature. This distinction arises from the differences in shape and size between the toroidal rim and the sheet rim in the hole–rim case. Specifically, the sheet rim possesses only one principal curvature, which is smaller than that of the toroidal rim. Consequently, during merging, the toroidal rim exerts a larger capillary pressure compared to the sheet rim, resulting in the outward curved shape of the liquid bridge. After the collision of the rims bounding two holes or the liquid sheet, the resulting liquid bridge undergoes deformation in the vertical direction (y-axis), leading to the formation of a vertically expanding free liquid sheet. As this occurs, the kinetic energy of the free liquid sheet gradually decreases. Subsequently, under the influence of capillary forces, the upper and lower edges of the vertically expanded liquid bridge recede and eventually merge. Following this, the liquid bridge undergoes deformation in the horizontal direction, forming a horizontally expanding free liquid sheet. This too recedes and merges again. The oscillation of the liquid bridge during these processes has the effect of drawing liquid from the central part of the bridge towards its ends, resulting in the formation of a cone that progressively thickens over time. This observation underscores the influence of geometric factors on the morphological features of the liquid bridge during the merging of holes in the thin liquid sheet. The expansion of the holes leads to the breakup of the thin sheet. By measuring the expansion velocity (U_H) of the holes, local planner thickness (h) can be calculated from the Taylor-Culick relation [153]

$$h = 2\,\sigma/\rho\,{U_H}^2. \qquad (6.3.4)$$

By considering a surface tension of σ = 0.0187 N/m and density ρ= 691 kg/m^3, the film thickness is calculated as 1.2 µm. By employing mass conservation, it compares to an average film thickness of 4.8 µm, neglecting mass loss on the proximal droplet side. The coalescence of these holes in the sheet gives rise to the creation of liquid ligaments. Subsequently, these ligaments undergo Rayleigh–Plateau instability, resulting in the formation of relatively large droplets compared to the initial ejecta on the left-hand side of the droplet (Figure 35 c-d, at t= 20 µs). The complete rupture of the sheet is observed approximately 700 µs later, in Figure 35 (d), reaching its maximum surface area at t = 600 µs. Figure 37 depicts the sheet breakup through the development of patches (pre-hole and hole) on the sheet. Figure 37 (a) shows the single pre-hole and subsequent hole formation on the sheet. Figure 37 (b) shows the multiple pre-holes and subsequent holes formed on the sheet. It is observed that the diameter of the patches increases with time. Yet, the growth rate of D_{patch} in the pre-hole regime is notably slow in comparison to the hole regime. To understand the evolution of pre-holes and holes in detail, we monitored the number of pre-holes and holes on the sheet.

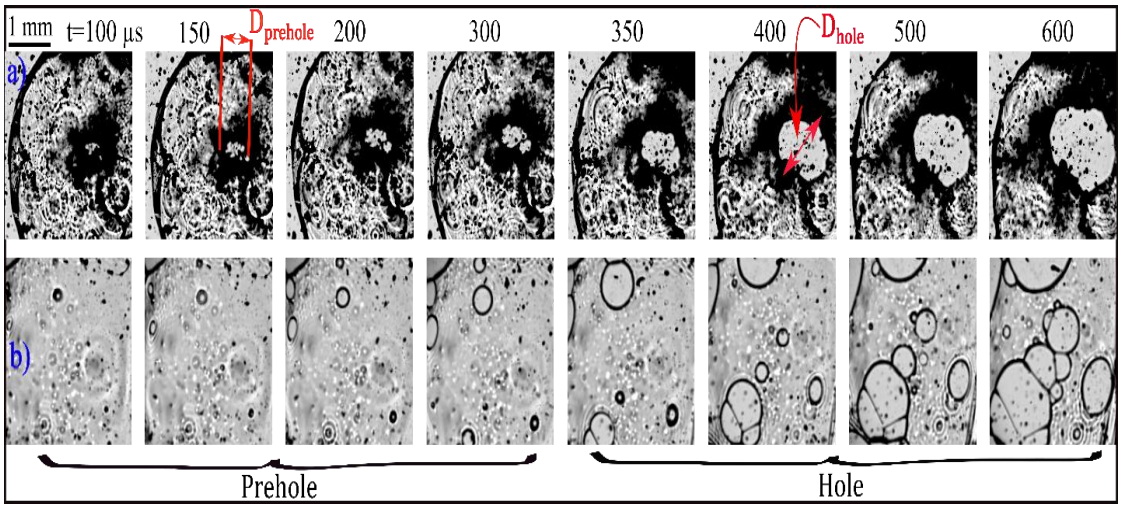

Figure 37. *Sheet breakup through nucleation of the holes in an iso-octane droplet: a) Single hole formation on the liquid sheet b) Multiple holes merging on the liquid sheet and its breakup.*

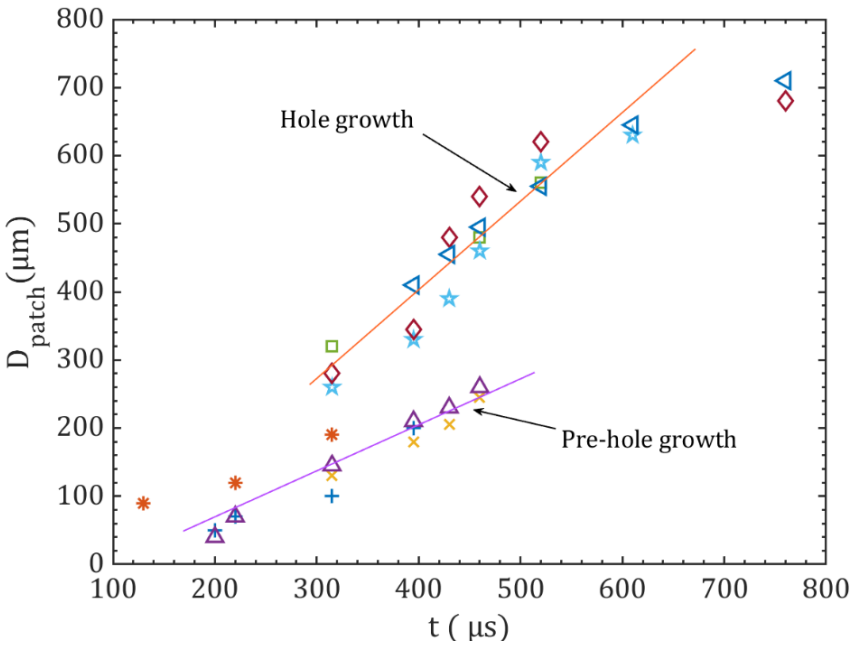

Figure 38. *The variation in diameter of pre-holes and holes over time corresponds to multiple instances of pre-holes and holes. The solid lines are linear fits.*

Figure 38 represents the temporal evolution of the diameter of patches i.e. $D_{prehole}$ and D_{hole}. The parameters $D_{prehole}$ and D_{hole} exhibit linear variations over time across all the monitored pre-holes and holes on the unstable sheet. The slope of the line representing $D_{prehole}$ is smaller in comparison to that of D_{hole} . This suggests that, even across a wider spectrum of pre-holes and holes, the growth of holes is considerably faster than that of pre-holes. The observed growth rate of holes in the experiment falls within the range of 0.5 to 2.4 m/s. By assuming the uniform and constant thickness of the sheet, theoretically the growth rate of the hole can be calculated by modifying the equation (6.3.4) as $U_H = \sqrt{\frac{2\,\sigma}{\rho\, h}}$. The theoretical hole growth rate is of order of 10 m/s, which agrees well with the experimental values.

6.3.4. Stable sheet collapse

The time sequence of stable circular sheet collapse for the iso-octane droplet is illustrated in Figure 35 (e). In this regime, initial fragments are visible at t= 20 μs due to the initial ejection of the mass at the proximal side of the droplet, typically it is fine mist captured at t = 10 μs. Simultaneously, the droplet stretches vertically and starts to form a circular sheet. The rim becomes notable at an earlier time, t = 50 μs and becomes more pronounced at t = 100 μs. The sheet experiences

substantial and non-uniform radial acceleration as fragments detach from the sheet. By analyzing Figure 35 (e), we can estimate the acceleration of the liquid on the proximal side toward the downstream end of the sheet. The acceleration of the sheet (a_s) measured is approximately order of 10^5 m/s^2. The sheet achieves the maximum vertical expansion typically at t = 400 µs and the liquid sheet starts to decelerate. At this point, the liquid starts to accumulate at the edges of the sheet making the rim thicker. The sheet collapses under the influence of the surface tension as captured at t = 800 µs. The capillary time $\tau_c = \sqrt{\rho R_0^3 / 6\sigma}$ is defined by balancing the surface energy with kinetic energy. This time scale represents the duration during which a hemispherical liquid sheet with a radius R_s collapses to a common center. Hence, converting surface energy into kinetic energy. We obtain τ_c= 460 µs for Figure 35 (e). It agrees well when compared to the observed duration of the sheet lifetime.

6.4. Fragmentation of n-hexane droplet

Figure 39 (a-f) shows the initial fragmentation of n-hexane droplets exposed to the laser pulse energy. Similar mechanisms are observed compared to iso-octane droplets. The major difference in the results observed for n-hexane droplets is the low angle of opening compared to iso-octane droplets. Fine mist at the distal side and larger fragments at the edges and the rim of the sheet are observed. The fragmentation is influenced by the location of the nucleation. Figure 39 (g) represents the graphical view of the laser pulse focus location inside the droplet. The two cases of laser positions are depicted in this figure, where the first case presents the laser position just near the edge of the droplet and the second case represents the laser position exactly at the center of the droplet. Depending on the position of the laser pulse focus, the angle of fragmentation changes and subsequently decides its strength. When the nucleation occurs very near to proximal side surface of the droplet, the lesser opening of the droplet, a relatively low angle of fragmentation is shown in Figure 39 (a). As the location of the nucleation moves from proximal to the center of the droplet, the angle of fragmentation increases from narrow to wide (Figure 39 (a-e)).

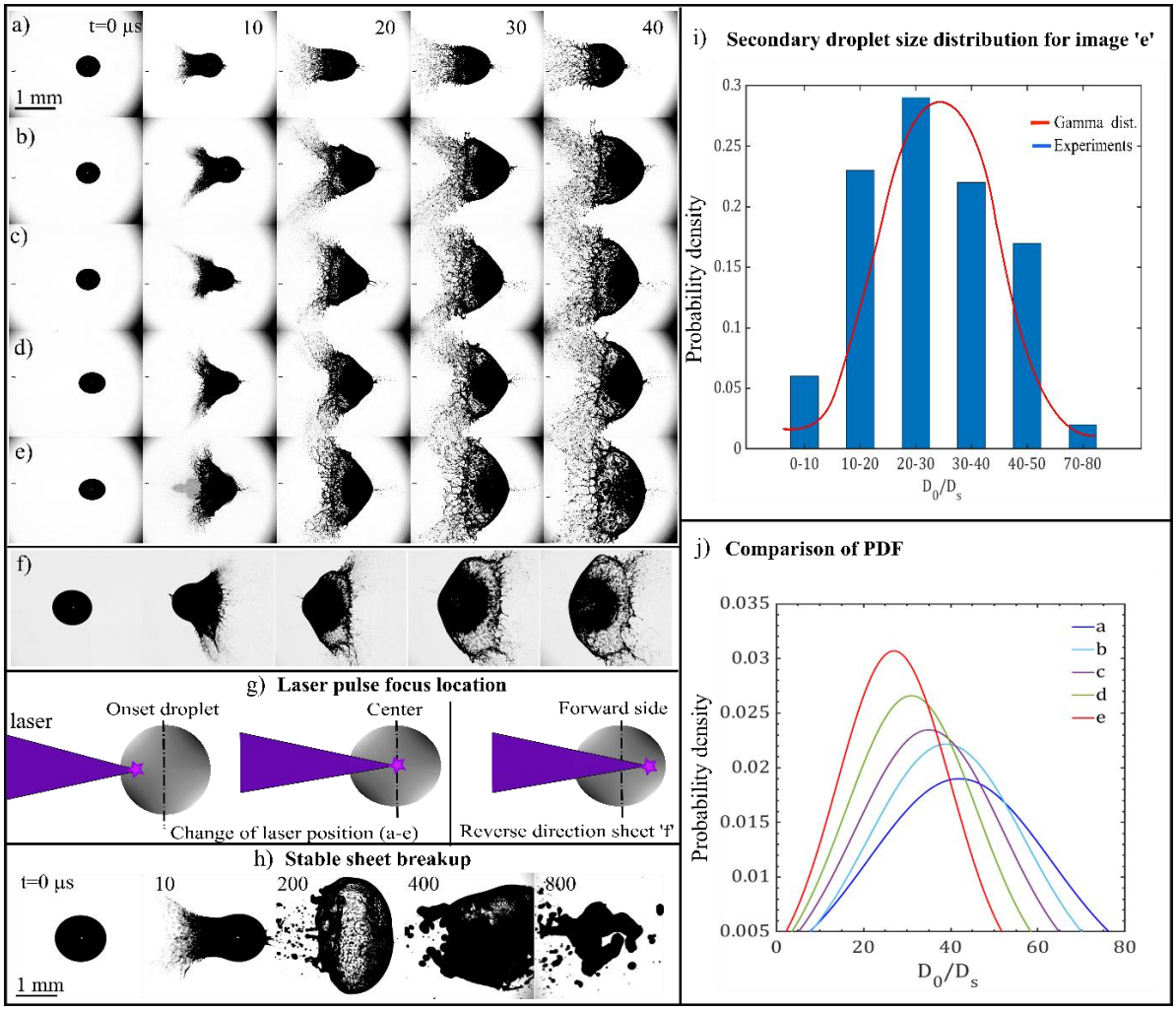

Figure 39. *Initial fragmentation of n-hexane droplet showing a vertical expansion of the droplet concerning laser pulse focus position (a-e). Initial narrow opening for (a) to wide opening for (e) at the proximal side of the droplet, see at t = 10 µs. f) Reverse direction fragmentation of the droplet. g) Graphical representation of the laser pulse focus position inside the droplet. h) Stable sheet breakup of the droplet i) Probability density and normalized secondary droplet size distribution of n-hexane droplet depicted in 'e'. j) Comparison of probability density function for images a-e.*

As the focus location moves towards the center, internal pressure is higher, and the material is ejected at a wider angle. Hence, a wider angle of fragmentation is observed at the center of the droplet (Figure 39 (e)). When laser focus is beyond the center point of the droplet, away from the proximal side, the reverse direction of the sheet is observed. Hence the angle of the fragmentation is opposite to the earlier cases observed (Figure 39 (f)). After the droplet wall ruptures violent ejection of the vapor mist and fragments is observed. This high-speed ejection is caused by the pressure difference developed between the inside and surrounding of the droplet. A rapid multiphase flow of ejected fragments and vapor mist is

observed. This develops an expanding jet flow of gas and fragments. The sheet/main droplet body also gains momentum along with the fast-ejected materials. The center of the mass of the closed system remains stationary.

As a combined effect, the main droplet propels forward and expands vertically to form a sheet (Figure 39 (h)). The sheet is formed after the bulk of the gas comes out of the back side due to a reduction in pressure at the proximal side of the droplet. The secondary droplets produced from fragmented droplets follow a gamma distribution, consistent with the reported literature[21,163]. Villermaux (2007)[21] demonstrated that gamma distributions are more effective at fitting drop-size distribution data when compared to distributions such as Poisson or log-normal. Normalized secondary drop size distribution for fragmented droplets for case 'e' is shown in Figure 39 (i). A similar distribution is observed for all the fragmenting droplets in the present study. The comparison of the probability density function for change in the location of the laser pulse focus is represented in Figure 39 (j). The location of the laser focus with respect to the center of the droplet decides the distribution for the number density and sizes produced. The wider opening of the droplet results in larger-sized droplets being ejected and more violet fragmentation. In the case of a low angle of opening of the droplet, it produces relatively small secondary size droplets but less material ejection.

6.5. Shear layer formation in fragmenting drop

The breakup of two similar-sized droplets by a laser pulse with the same laser energy is depicted in Figure 40 (a, b). It shows the repeatable fluid mechanics, evidenced by the similar sizes of the resulting fragments. This includes the formation of a fine mist on the proximal side and larger fragments originating from the sheet and its edges. Upon closer examination of the images, it reveals that the angle at which fragmentation occurs is influenced by the location of the nucleation. In Figure 40 (a), the nucleation is closer to the proximal side. Subsequently, it ruptures through the droplet wall and mass is ejected at a wider angle as its internal pressure is higher. At this specific condition, we observe two dark stripes on the distal side. These stripes become apparent roughly 20 µs after the laser pulse. After some time, these strips become invisible as they are carried away by turbulent flow.

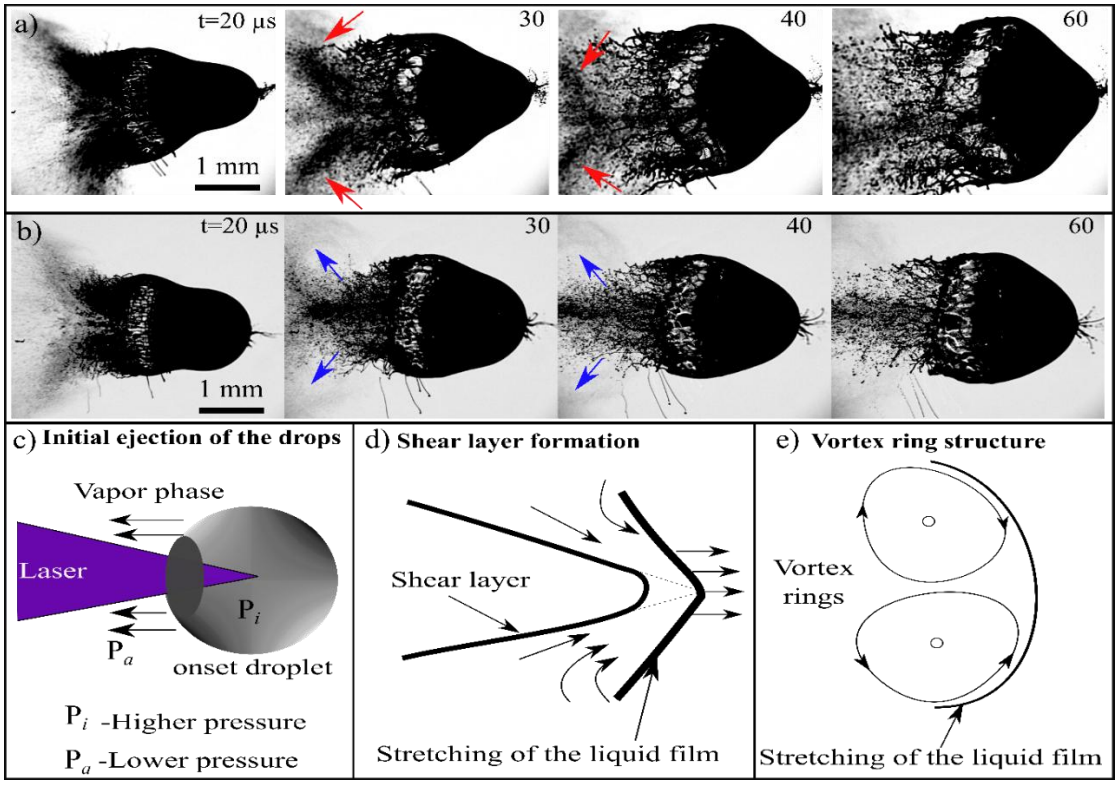

Figure 40. *The initial ejection of the fragments and shear layer formation in the stretching liquid sheet. a) & d): - Shear layer formation; b) & e): - Vortex ring formation around the ejecting drops; c) Initial ejection of the drops.*

Despite initially resembling two distinct stripes, their actual structure comprises an area with densely packed fine droplet fragments, forming a cone shape. This specific cone shape likely arises from the flow pattern trapping the fragments and increasing their concentration. Such a phenomenon may be attributed to a localized region of reduced gas velocity, such as a shear layer between two dominant flows. The phenomenon of the shear layer formation is well demonstrated in Figure 40 (d). The fine mist present at the distal side creates a vortex ring formation around the stretched liquid sheet. These vortex rings are observed in Figure 40 (b), approximately 20 µs after the laser pulse and it is marked by blue arrows. The phenomenon of the vortex ring formation is well depicted in Figure 40 (e). The violent ejection of fragmented drops along with the fine vapor mist is observed as the droplet ruptures by a laser pulse. It creates a fast-multiphase flow with higher pressure (P_i) inside the droplet and lower pressure (P_a) in the surroundings, this phenomenon is demonstrated in Figure 40 (c). This results in the formation of an expanding jet stream comprising both gas and fragmented particles. When regarding the droplet and surrounding air as a closed system, conservation of

momentum dictates that the fast-expelled material imparts momentum to the main droplet/sheet, ensuring that the system's center of mass remains stationary. The sheet is formed as a droplet expands radially outward in the distal direction. This decrease in pressure on the proximal side leads to the suction of gas from the surrounding bulk, contributing to the formation of a sheet at the back. At the rear side of the droplet, the expanding jet and the inflow of gas move in opposite directions, resulting in the formation of a stagnation zone along a stagnation surface where they meet and compete. The dark stripes observed in Figure 40 (a) at time t = 20 µs are now understood to correspond to the stagnation surface. At this point, droplets accumulate due to the reduced velocity. Subsequently, as both flows diverge, turbulence is expected to carry these accumulated droplets. This phenomenon is also witnessed in the study by Avila *et al.* [122].

6.6. Fragments impact on the liquid sheet

Droplets are captured in a vorticial flow at the far end of the sheet. The ejected droplets may be captured in this flow and eventually impact the sheet. It leads to capillary wave generation on the sheet which subsequently ruptures the sheet. This process deforms the sheet and leads to eventual fragmentation of the sheet. Figure 41 depicts the successive time frames of the phenomenon of impact of the fragments and eventual capillary/surface wave travel. The droplet sheet is marked with a green arrow to represent different droplets/fragment's impact during successive frames.

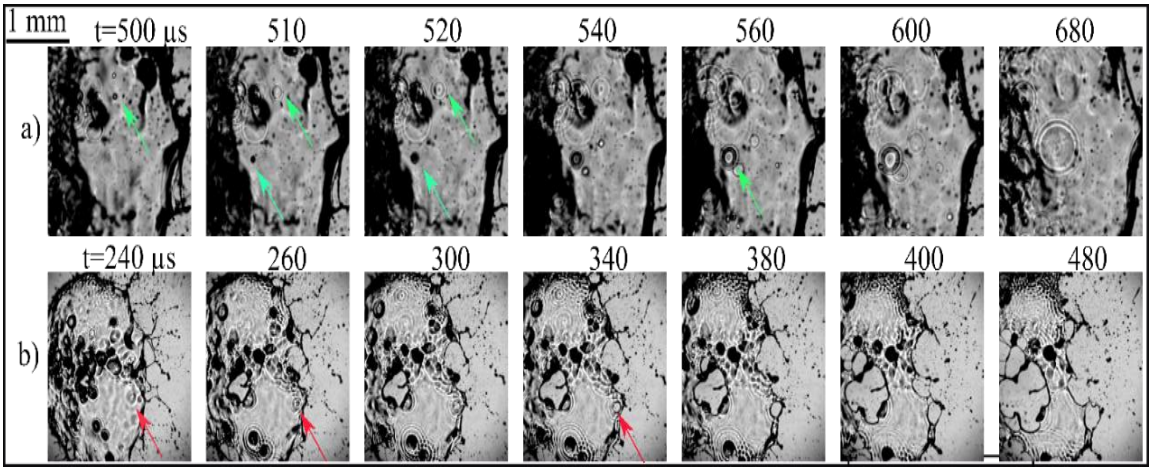

Figure 41. *The fragments impacting the liquid sheet membrane: a) capillary waves on the surface We = 0.5 b) Rupture of the membrane We = 4.3.*

The impacting droplet has a radius r and V_{rel} is the relative velocity between the sheet and impacting droplet. The relative velocity measured is 3.9 m/s. The Weber number (We) is calculated by comparing the kinetic energy of the droplet and the surface energy of the sheet, $We = \rho r V_{rel}^2/\sigma$. The rupture of the membrane due to fragment impact and surface waves on the surface occurs at We in the range of 4.3 to 6.8. In most observed cases, we predominantly witness either coalescence or bouncing with We < 4.3. There has been no instance of droplet tunneling through the sheet.

Figure 41 (a) illustrates a scenario where the sheet undergoes deformation but does not rupture, with the impacting droplets tracked by the green-colored arrows. Similarly, Figure 41 (b) depicts the rupture of the membrane by fragment impact. Avila *et al.*[122] reported the study on the film ruptured by a single droplet impact on the sheet. A detailed study of a droplet's impact on a thin film has been reported by Courbin & Stone (2006)[164]. For Weber numbers W_e <16, Gilet & Bush (2009)[165] observed bouncing and coalescence, a finding that was approximately corroborated by Kim & Wu (2010)[166]. A surface tension gradient is observed during the impact of droplets on the sheet of the liquid. Marangoni stresses are observed during the rupture of a thin splash of water because of the impact of ethanol droplets [7,119]. Gilet & Bush(2009)[165] used higher surface tension liquid impacting on the soap film, whereas the present study has the same liquid impacts on the thin sheet.

6.7. Instabilities

6.7.1. Rayleigh-Taylor (RT)

The liquid ejection through fine jets and surface waviness is observed in earlier sections. To get more clarity, the wave generation and jet ejection from the surface are shown in Figure 42. The smaller mass is displaced from the upper and lower sides of the droplet which is a potential cause of triggering the R-T instability. The surface undulations are the starting point to the jet formed and fragments ejected from the edges of the sheet. The underlying mechanism for this phenomenon may be similar to jetting resulting from impulse pressure as reported by Antkowiak et al. [161]. They reported concentrated flows are directed toward concave regions of the liquid-gas interface, leading to the acceleration of slender jets. When the surface

geometry does not align with the impulse pressure distribution, gradients in the liquid are established, leading to the acceleration of the fluid. In our experiments, the fragment's impact and collapse create a rapid inward flow that experiences an abrupt cessation and reversal, transforming into an outgoing flow.

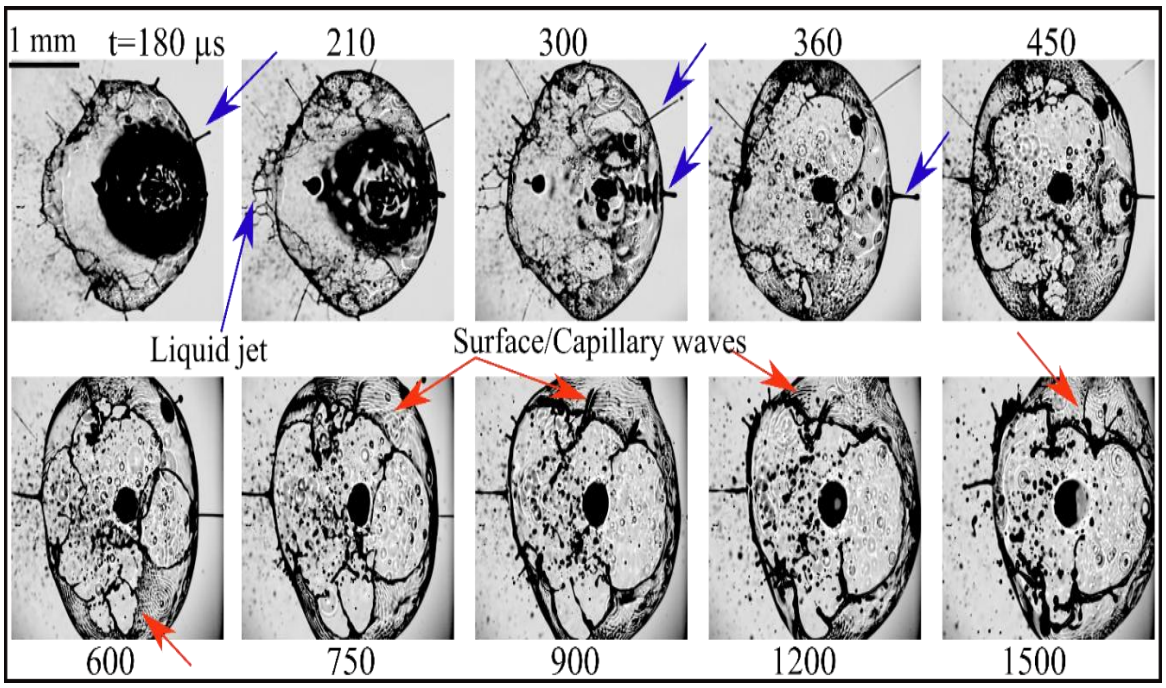

Figure 42. *Liquid jet ejection and surface/capillary wave propagation from the liquid sheet surface. The blue arrow shows the liquid jet ejected from the sheet and the red arrow shows the surface/capillary waves travel on the sheet surface.*

Neglecting the intricacies of the collapse phase, the final liquid velocity post-collapse can be characterized by the gradient of an impulse pressure. In this case, the surface corrugations deviate from the expected impulse pressure distribution, which usually entails spherical waves originating from the surface of the sheet. The impulse pressure must adhere to the constant pressure boundary condition near the droplet-gas interface for it to serve as a solution to the Laplace equation. Consequently, pressure gradients near the surface are anticipated to meet the boundary condition. Particles near the rim of the sheet belong to a continuously decelerating density interface. Therefore, there is no pressure gradient along the radial direction and hence no net body force. According to Culick´s law, the expansion and recoil dynamics are made under constant pressure where liquid inertia is balanced by restoring force concentrated at the edge of the rim. Despite the rim of the sheet experiencing deceleration for a significant portion of its

development period, the occurrence of a global Rayleigh–Taylor instability in the expanding sheet is improbable. This is because the deceleration primarily affects the fluid particles located in the rim of the sheet, and most of the liquid in the sheet does not undergo this deceleration.

As a result, the conditions necessary for a global Rayleigh–Taylor instability, which typically involves a widespread disturbance in the fluid, are not prevalent in the main body of the expanding sheet. Instability is confined to the rim where the deceleration is taking place. The breakup is instigated by individual fragments colliding with the sheet. Notably, the ejected mass resulting from the early jetting phenomenon, as mentioned earlier, serves as the source of these fragments. Importantly, this ejected mass travels at a significantly higher velocity than the expanding sheet, making it improbable for later collisions with the sheet. Bremond and Villermaux (2005)[112] have observed the nucleation of holes in micro-meter-thick, freely suspended liquid sheets. In their study, an impulsive acceleration of the sheet initiated a Rayleigh–Taylor instability, leading to the development of growing corrugations that ultimately pierced the sheet. The observed number of holes is determined to rise proportionally with the Weber number calculated based on the forward velocity (and consequently the acceleration) of the sheet. Simultaneously, the characteristic rupture time exhibited a decrease with the Weber number [112].

6.7.2. Rayleigh-Plateau (RP)

In 1873, Joseph Plateau was the first to identify this instability, drawing on previous research by Savart. He observed that instability occurred when the length of the liquid column exceeded its diameter by approximately 3.13 times[167]. Later, Lord Rayleigh validated Plateau's findings by providing a theoretical explanation for this phenomenon. As a drop expands, the liquid jets and ligaments are ejected, initially maintaining a constant radius until they rupture due to surface tension effects. These jets and ligaments gradually elongate, generating surface perturbations. The development of instabilities is dependent upon the growth rate and length scale of these perturbations. The growth rate is crucial in determining which disturbances trigger instability. As perturbations on the fluid surface grow, they create increasingly steep gradients. This heightened curvature results in greater pressure

gradients, driving a stronger momentum flux from areas of high to low pressure, ultimately leading to the formation of droplets as pinched regions rupture. Droplet formation is initiated when pressure gradients induce internal flux, pushing fluid from troughs to peaks. Surface tension amplifies this process, with higher surface tension intensifying pressure gradients and accelerating droplet formation. Finally, the length of ligaments eventually reaches a critical value where they fragment into a stream of smaller droplets, marking a significant stage in the atomization process. Figure 43 shows the instabilities occurred to the liquid jet ejected and ligaments formed during the expansion of the droplet. The ejected liquid jets are shown in blue arrows and ligaments formed are marked as red color arrows. The thin ligaments are formed that becomes RP unstable and subsequently breaks into smaller secondary drops.

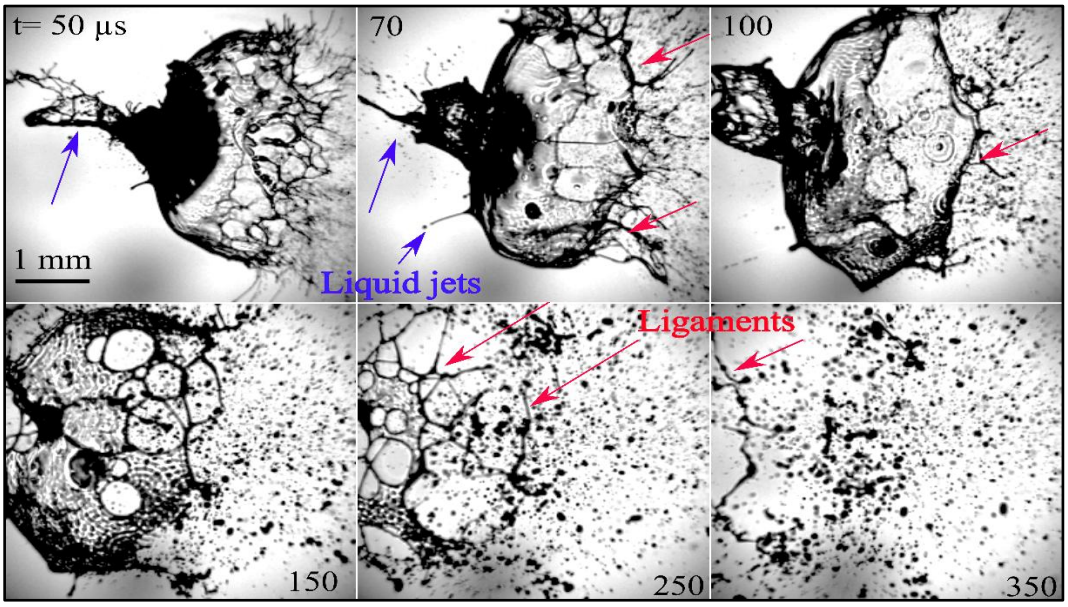

Figure 43. Ligament breaking under the RP instability.

6.7.3. Kelvin–Helmholtz (KH)

The instability mechanism is initially understood by von Helmholtz in 1868 and later quantitatively described by Kelvin using the dispersion relation in 1871. The Kelvin-Helmholtz (KH) instability arises from the rapid acceleration of a liquid sheet, inducing velocity shear within an expanding drop. It is primarily driven by the relative motion between the expanding sheet and the surrounding air, causing wave-like disturbances that grow and lead to the breakup of the liquid sheet. It

represents the interplay between gravitational force and shearing force resulting from the relative motion between two fluid layers. It is influenced by factors such as density, viscosity contrasts, surface tension, and flow speed. In the case of a levitated droplet, this concept extends to the instability between the shear force caused by acoustic streaming velocity at the droplet surface and the net downward or upward force acting on the droplet.

6.8. Summary

This study explores the distinct characteristics of laser-induced plasma, shock wave dynamics, and the subsequent breakdown of iso-octane and n-hexane droplets, detailing the hydrodynamic response of droplets to laser impact, including propulsion, deformation, expansion, and fragmentation. Initially, plasma formation and shock wave evolution propel the droplet forward, causing radial expansion into a thin sheet. Fragmentation occurs through mechanisms influenced by the Weber number and the distribution of kinetic energy, leading to sheet breakup due to small disturbances and variations in sheet thickness. Additionally, forward acceleration destabilizes the sheet through hole nucleation and merging, exhibiting complex dynamics influenced by capillary pressure and bridge shape. Fragmentation arises from Rayleigh–Taylor and Rayleigh-Plateau instabilities, with the fuels exhibiting rapid phase changes: n-hexane forms a grey haze while iso-octane undergoes complete atomization, with iso-octane's higher viscosity resulting in wider expansion, a higher opening angle, and more violent breakup compared to n-hexane's generally stable sheet breakup.

7. Droplet Evaporation

7.1. Introduction

The oil and gas industry seeks innovative, eco-friendly solutions to mitigate crisis of fossil fuel and greenhouse gas emission. Cellulose nanomaterials (CNMs) offer promise due to their abundance, cost-effectiveness, renewability, and exceptional properties, including high surface area and tunable chemistry. Three main types of CNMs: cellulose nanofibers (CNFs), cellulose nanocrystals (CNCs), and bacterial cellulose (BC) are produced using various methods, making them valuable for sustainable oil and gas development initiatives[31,34,168]. The modern composites industry prioritizes sustainable and environmentally friendly products, with natural fiber-reinforced polymer composites gaining traction. Cellulose, a renewable resource, is key in this regard. Recent focus has been on cellulosic nanomaterials, including nano fibrillated, nanocrystalline, and bacterial celluloses, which offer unique properties like nanoscale dimensions and high strength. These materials show promise in developing new composites with improved mechanical and barrier properties, particularly for eco-friendly applications like packaging and coatings[169,170]. Cellulose nanocrystals (CNCs) are derived from various cellulose sources through acid hydrolysis, which removes the less ordered cellulose phase. While sulphuric acid hydrolysis is commonly used for efficient extraction, other hydrolysis methods like hydrochloric acid or formic acid are also effective. The properties of CNCs and their water-based suspensions, as well as the yield, depend not only on the cellulose source but also on the conditions of sulphuric acid hydrolysis and subsequent sonication processes[171–174]. CNCs are firm, rod-shaped particles made up of parallel cellulose chains, their sizes in the sub-micron range determined by the initial material. Due to electrostatic stabilization from negatively charged sulfate surface groups, they maintain a stable aqueous suspension. Beyond critical concentration, they undergo a phase transition to form a chiral nematic liquid crystalline phase. The color and strength are provided by chiral nematic structures that are found in animals and plants. Higher ionic strength raises the critical concentration for phase formation while reducing the pitch of the resulting chiral nematic structure[174–177]. CNCs derived from natural cellulose fibrils have the inherent ability to self-assemble at the nanoscale, forming similar structures that

can reflect light within the visible spectrum. When aqueous suspensions of CNCs evaporate, they produce iridescent chiral nematic films that exhibit reflection colors within the visible spectrum. A significant challenge lies in regulating the chiral nematic pitch of these films, which ultimately determines their reflection colors. We discuss the liquid crystalline properties of cellulose nanocrystals in suspension and review methods for directing their self-assembly into vibrant, structurally colored materials. We explain techniques for controlling the optical characteristics, including color and angular response, emphasizing the influence of geometric confinement on self-assembly. Additionally, we explore strategies for improving cellulose nanocrystal-based optical materials to expand their functional applications.

Further the study explored the evaporation of the CMC and Silica droplets. Comparing the evaporation dynamics of cellulose nanocrystal (CNC), carboxyl methyl cellulose (CMC), and silica droplets offers valuable insights into their unique behaviors and potential applications. While CNCs derive from natural cellulose and exhibit remarkable mechanical and optical properties, CMC serves as a water-soluble polymer with versatile rheological characteristics. Silica droplets, composed of dispersed silica nanoparticles, boast high surface area and chemical inertness. The comparison reveals differences in evaporation rates, self-assembly behaviors, and final morphologies among the materials. CNC droplets may undergo self-assembly into ordered structures, CMC droplets may form gel-like structures due to polymer chain entanglement, and silica droplets may exhibit aggregation of nanoparticles. Such comparisons aid in understanding the diverse properties of these materials, informing their potential applications across fields such as materials science, biotechnology, and nanotechnology, including sustainable initiatives within the oil and gas industry.

7.2. Laser induced evaporation of CNCs drops

We are examining how electrostatic and solvation-induced stabilizations affect the self-ordering of CNC suspensions as they evaporate. The self-ordering of CNC suspensions refers to the spontaneous arrangement of the CNC particles as the

suspension undergoes evaporation. This process occurs due to various factors, including the interactions between CNC particles and their interactions with the surrounding solvent. During evaporation, as the solvent evaporates, the CNC particles come closer together, leading to interactions such as van der Waals forces, hydrogen bonding, and electrostatic interactions between the particles. These interactions drive the CNC particles to organize themselves into ordered structures, typically with long-range positional and orientational correlations. The self-ordering behavior of CNC suspensions is influenced by factors such as the concentration of CNC particles, the properties of the solvent, temperature, and the presence of additives or stabilizers. Understanding and controlling the self-ordering process is crucial for applications such as, fabrication of CNC-based materials with tailored properties like optical properties, mechanical strength, and conductivity[171,172,178].

The experimental setup involved investigating various concentrations of CNCs at 0.5%, 1%, 2.5%, and 5%, employing both natural evaporation and heating methods with different laser energies (2.5W and 5W). To facilitate the evaporation process, a continuous laser is employed, ensuring thorough drying of the CNC droplets. Following evaporation, the resulting samples are subjected to analysis using a scanning electron microscope (SEM) to observe any structural changes or phenomena. Interestingly, similar observations are made across all concentration levels and experimental conditions, revealing similar morphological changes. For a more comprehensive analysis, particular attention is given to the results obtained from the highest CNC concentration subjected to the maximum laser energy. By focusing on this specific condition, we aim to provide a detailed understanding of the temporal evolution during the evaporation process induced by the laser.

These experiments enabled us for a detailed examination of the effects of concentration and laser energy on the evaporation dynamics and resulting morphological changes in the CNC droplets. Figure 44 illustrates the chronological progression observed during the laser-induced evaporation of a CNC droplet with a concentration of 5% under the influence of 5W laser energy. Initially, as the CNC droplet undergoes evaporation, the solvent molecules at the surface of the droplet gain sufficient energy to overcome the intermolecular forces holding them together, transitioning into the vapor phase. This rapid evaporation phase is evident in the

initial stages (up to t=400 s). During this stage, the solvent content decreases significantly, leading to high concentration of CNC particles near the droplet's surface. Once the solvent completely evaporates (around t=500 s), the CNC particles become more concentrated near the surface due to capillary forces. This concentration of CNC particles at the surface initiates the next phase of the process, i.e. marking the onset of CNC accumulation. As the CNC particles accumulate near the surface, a flat thin film begins to form at the centre of the droplet, the process continues until approximately t=550 s. Subsequent heating further accelerates the accumulation of CNC particles, causing the droplet to start flattening around t=560 s. As the droplet flattens completely by t=600 s, the self-assembly process of the CNC particles begins. This phase, which commences around t=650 s, sees the CNC particles organizing themselves into ordered structures. Finally, as the self-assembly process progresses, the CNC droplet adopts a hyperbolic paraboloid or saddleback shape by t=710 s. This shape indicates the completion of the self-assembly process and reflects the ordered arrangement of CNC particles within the droplet.

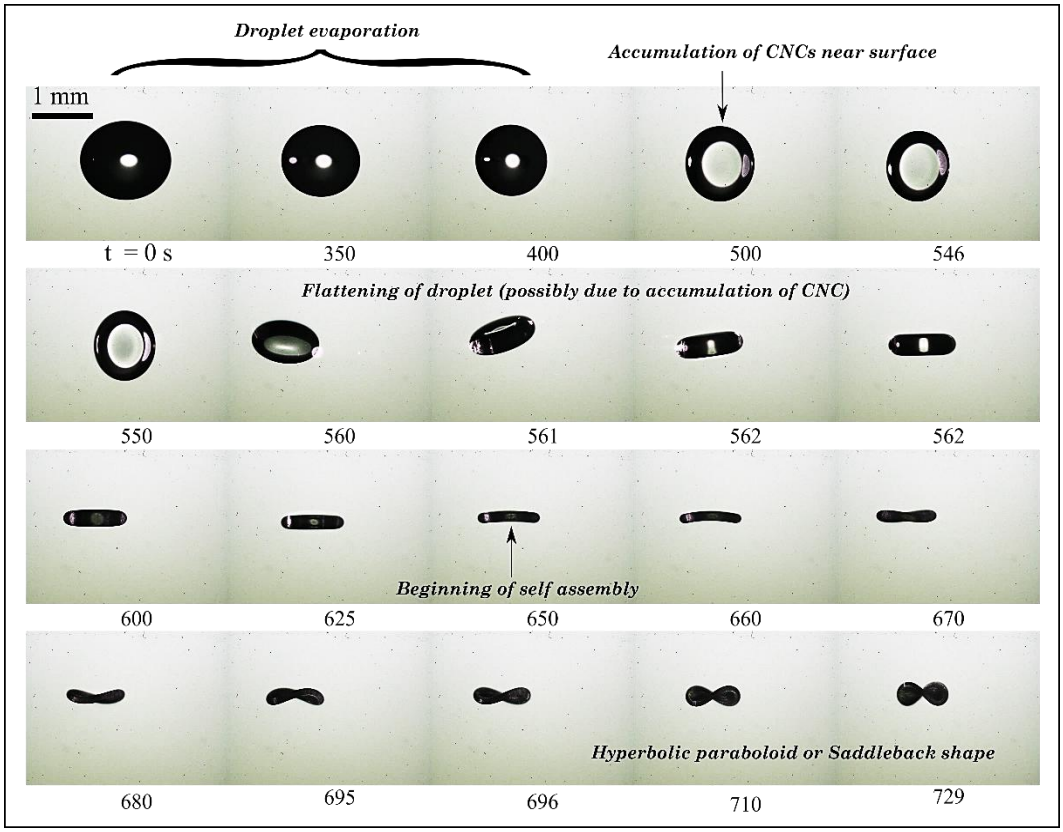

Figure 44. *Laser-induced evaporation of CNC droplet of D_0= 1.65 mm at 5 W and 5 % concentration.*

The colour nature of CNC droplets arises due to their structural properties, specifically their ability to scatter and reflect light. As the CNC droplet evolves during evaporation, its structural arrangement undergoes changes, influencing its optical properties. Initially, when the droplet is relatively thick and uniform, light scattering within the droplet leads to a white appearance. However, as the droplet evaporates and the CNC particles accumulate near the surface, the structural arrangement of these particles' changes. This alteration in structure affects the interaction of light with the droplet, resulting in the emergence of vivid, structurally colored patterns. The final shape of the CNC droplet, observed and confirmed under scanning electron microscopy (SEM) as depicted in Figure 45 (h), provides crucial insights into the self-assembly process and the arrangement of CNC particles near the surface. SEM imaging offers high-resolution visualization, to examine the morphology of the CNC particle in detail. The observed shape, whether it be a hyperbolic paraboloid or a saddleback shape, reflects the intricate arrangement of CNC particles resulting from the self-assembly process. This shape is significant for the establishment of ordered structures within the droplet.

The evaporation process of solvents from cellulose nanocrystal (CNC) droplets is a dynamic phenomenon influenced by various factors, each contributing to the intricate kinetics of the process. Temperature plays a pivotal role, as it directly affects the vapor pressure of the solvent and thus the rate of evaporation. Higher temperatures lead to increased kinetic energy of solvent molecules, facilitating their escape from the droplet's surface and accelerating the evaporation rate. Additionally, concentration gradients within the droplet influence the diffusion of solvent molecules towards the surface, impacting the overall evaporation kinetics. Changes in CNC concentration alters the viscosity and surface tension of the droplet, further modulating its evaporation behavior. During experimental investigations, CNC concentration varied from 0.5% to 5% and keeping uniform diameter of CNC at different energy levels depicted in Figure 45. It provides crucial insights into the relationship between CNC concentration, energy input, and evaporation dynamics.

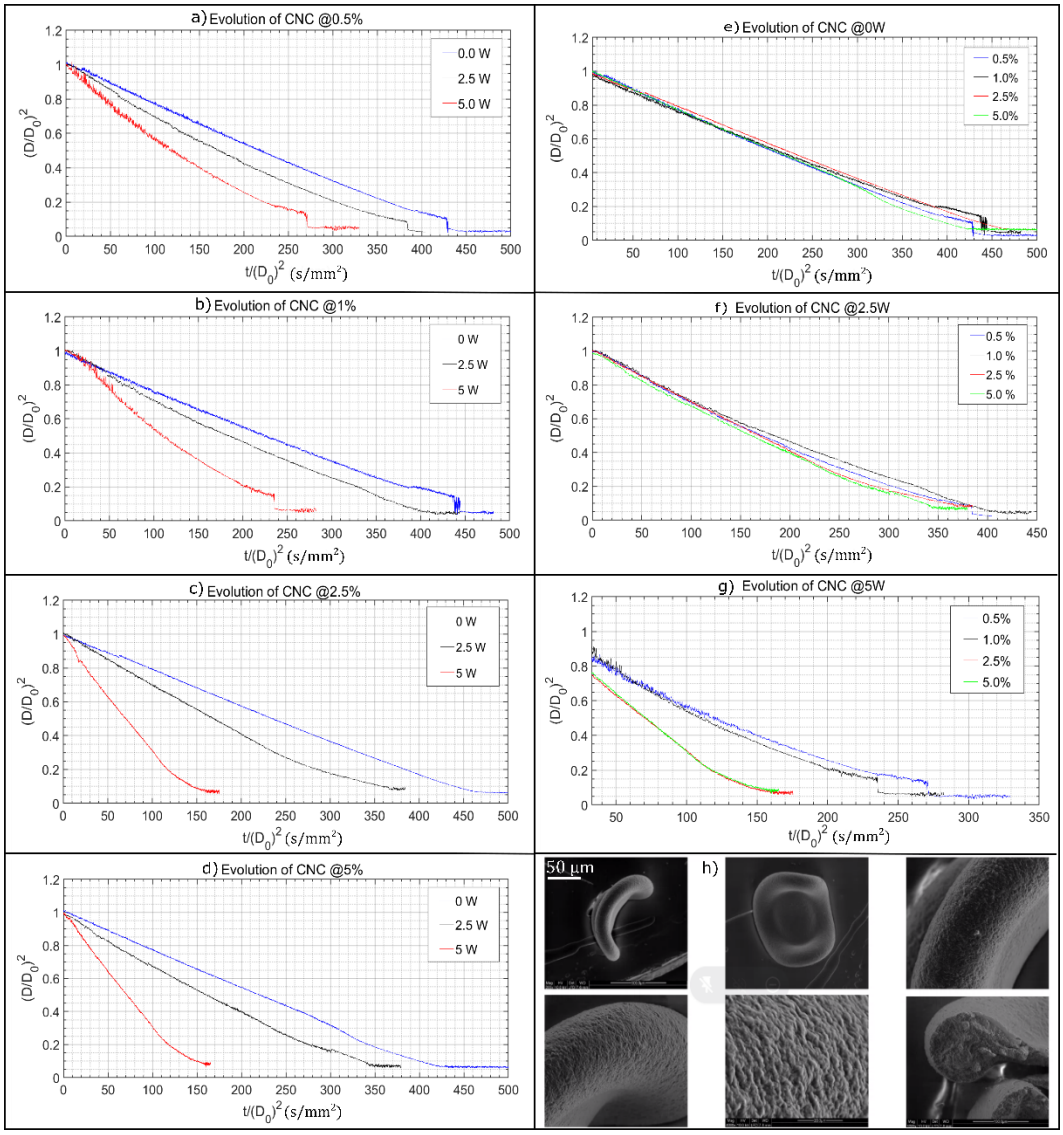

Figure 45. *Laser-induced evaporation of CNC droplets at different initial concentrations and laser energy. a) 0.5 %; b) 1 %; c) 2.5%; d) 5%; e) 0 W; f) 2.5 W; g) 5 W; h) SEM images of the end sample after the evaporation.*

Lower CNC concentrations result in a more dilute solution with fewer CNC particles available for self-assembly, leading to slower evaporation rates across all energy levels. Conversely, higher CNC concentrations yield a denser solution with more CNC particles, promoting faster evaporation rates and shorter times required for self-assembly. Comparing evaporation with and without external energy input, such as heating, highlights the significant impact of energy levels on evaporation kinetics. Natural evaporation processes, reliant solely on ambient conditions, take longer durations for self-assembly compared to instances where energy is applied externally. The application of energy increases the kinetic energy of solvent

molecules, expediting their escape from the droplet's surface and enhancing the evaporation rate. This accelerated evaporation facilitates quicker self-assembly of CNC particles, resulting in shorter overall process durations. Understanding these intricate relationships between CNC concentration, energy input, and evaporation dynamics is essential for controlling the fabrication of CNC-based materials with tailored structural and optical properties. By elucidating the underlying mechanisms governing CNC evaporation kinetics and self-assembly behavior, we can optimize fabrication processes and design CNC-based materials for various applications, including optoelectronic devices, coatings, and biomaterials.

7.3. Laser induced evaporation of CMC drops

Carboxyl Methyl Cellulose (CMC) is a water-soluble polymer derived from cellulose, offering unique rheological properties in solution. Unlike CNCs, CMC does not possess nanoscale particle interactions but forms networks or aggregates of polymer chains during evaporation. Its solubility in water allows for the formation of clear, viscous solutions without the need for additional solvents. The evaporation process of CMC droplets follows principles similar to CNC droplets, with solvent molecules escaping from the surface, leading to increased viscosity and gelation of the solution. CMC finds extensive use as a thickening agent, stabilizer, and emulsifier in various industries such as food, pharmaceuticals, and cosmetics, leveraging its water-solubility and rheological properties for diverse applications[179,180]. The analysis of Figure 46, depicting the temporal dynamics of the laser-induced evaporation of a 5% concentration Carboxyl Methyl Cellulose (CMC) droplet at 5W laser energy, provides valuable insights into the differences between CMC and CNC droplets during evaporation. The higher CMC concentration is chosen to enable a comparison with CNC droplets. The observation of a slower evaporation rate for the CMC droplet, as indicated by the longer duration until flattening begins at t=750 s, suggests differences in the evaporation kinetics between CMC and CNC droplets. Additionally, the solid sample remaining at the end of the evaporation process suggests the formation of a gel-like structure due to the polymer chains of CMC becoming entangled and forming a network during evaporation. This gel-like structure contrasts with the self-assembly of CNC

particles observed near the surface, which results in the acquisition of a specific shape. Overall, the comparison highlights the distinct behaviors and outcomes of CMC and CNC droplets during evaporation. CMC forms a thick, stable sample with a gel-like structure, while CNC undergoes self-assembly near the surface, leading to specific shape formation. This detailed analysis provides valuable insights for understanding and controlling the evaporation dynamics of CMC and CNC droplets and tailoring their properties for various applications.

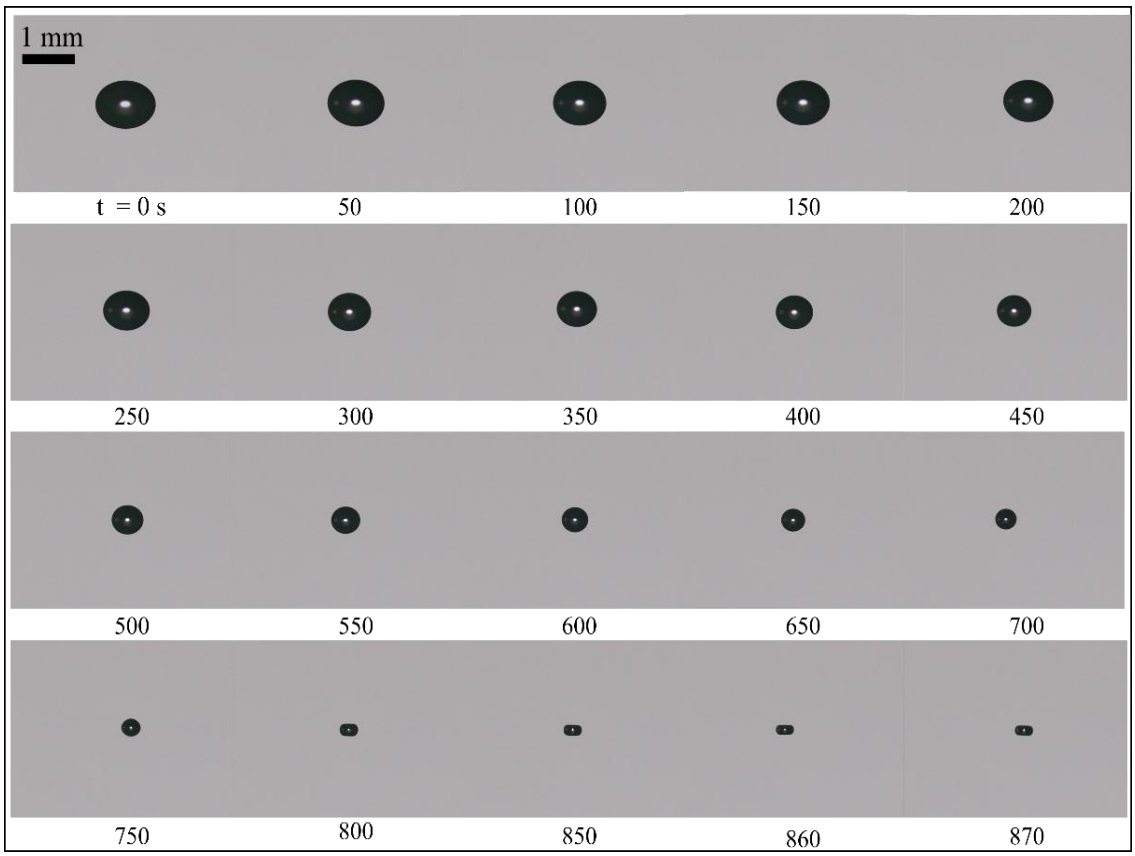

Figure 46. *Laser-induced evaporation of CMC droplet of D_0= 1.61 mm at 5 W and 5 % concentration.*

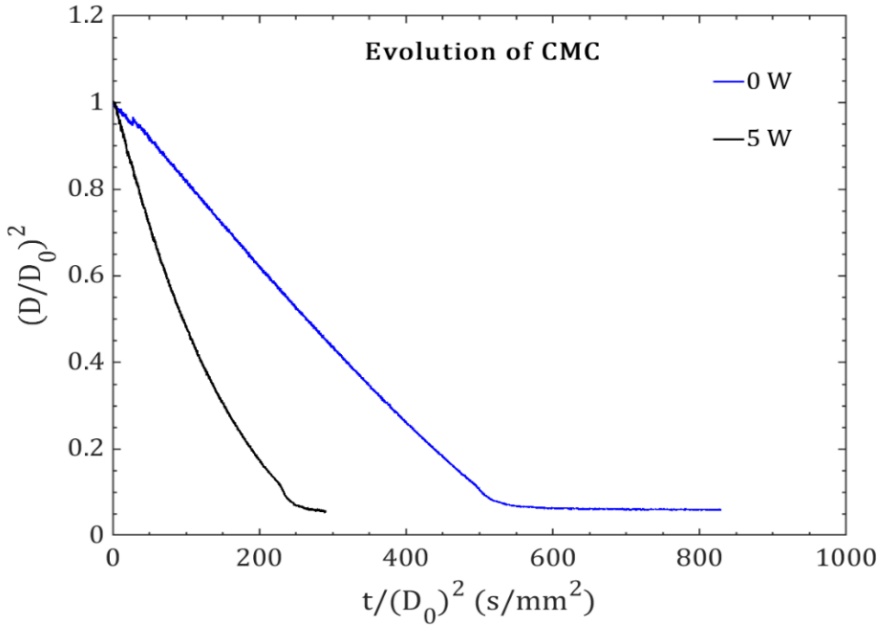

Figure 47. *Laser-induced evaporation of CMC droplet at 0 W and 5 W laser power.*

The comparison presented in Figure 47 between natural evaporation and heating using a laser provides a detailed analysis of the evaporation kinetics of Carboxyl Methyl Cellulose (CMC) droplets. Firstly, the observation of a slower evaporation rate for naturally evaporated droplets compared to those evaporated with a laser suggests that the application of external energy accelerates the evaporation process. This acceleration is attributed to the additional energy input from the laser, which increases the kinetic energy of solvent molecules, facilitating their escape from the droplet's surface. The sudden decrease in the evaporation rate observed with the laser-evaporated droplet, as depicted in the graph, indicates a rapid removal of solvent molecules from the droplet's surface, leading to a more abrupt decrease in droplet volume. These differences in evaporation kinetics between natural and laser-induced evaporation are attributed to the properties of CMC droplets, including viscosity, surface tension, and molecular interactions.

7.4. Laser induced evaporation of Silica drops

Figure 48 provides a comprehensive overview of the temporal dynamics observed during the laser-induced evaporation of silica droplets, focusing on the distinct properties and behaviors inherent to silica droplets during the evaporation process.

Initially, rapid evaporation is observed at t = 50 s, indicative of the high volatility of the solvent within the droplet. This rapid evaporation leads to a gradual reduction in droplet size, reflecting the loss of solvent molecules from the droplet's surface. As evaporation progresses, the droplet undergoes deformation in the axial direction, indicating internal changes within the droplet structure, which becomes evident around t = 110 s. This phase of deformation is accompanied by nucleation events inside the droplet, possibly indicating the formation of new structures or phases because of the evaporation process. Subsequently, the droplet flattens horizontally, signifying further evaporation and compression of the droplet's structure. The reduction in size and flattening of the droplet may be attributed to the continued loss of solvent molecules and the rearrangement of silica nanoparticles within the droplet. As heating continues, fragments are ejected from the droplet surface, beginning around t = 256 s, indicating increased instability and internal pressure within the droplet. This ejection of fragments persists, ultimately leading to the fragmentation of the droplet into several parts at t = 275 s, signifying the culmination of the evaporation process.

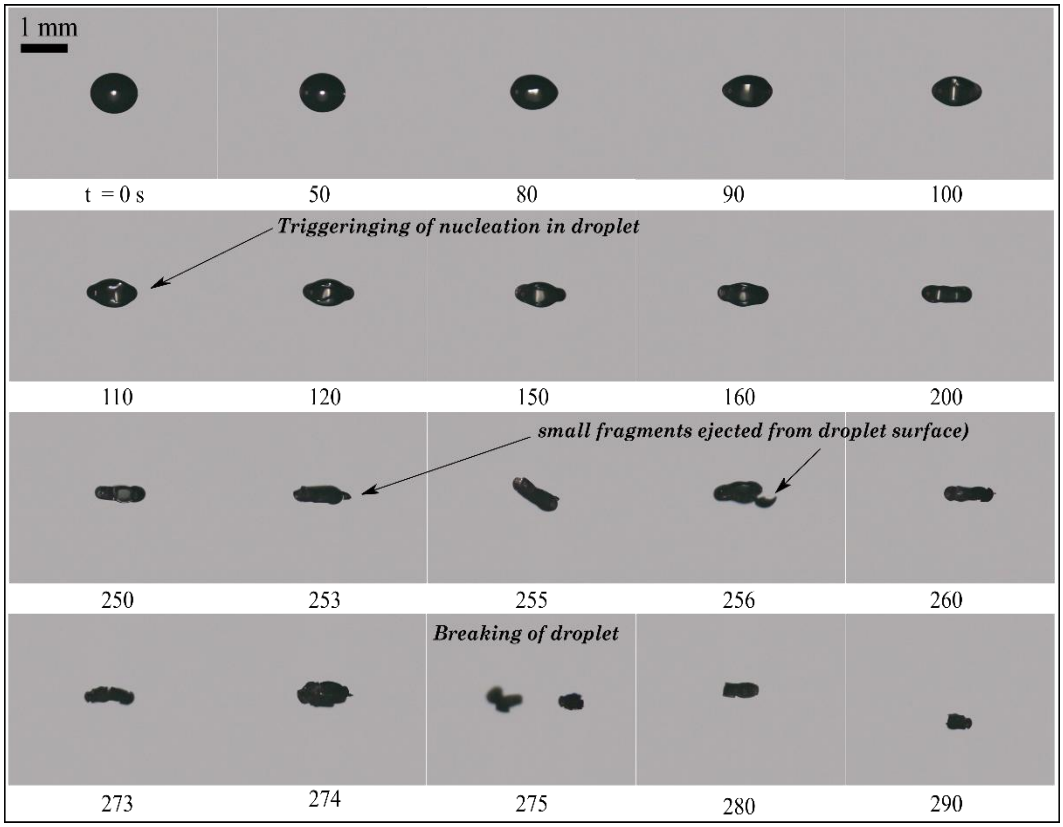

Figure 48. *Laser-induced evaporation of Silica droplet of D_0= 1.61 mm at 5 W laser energy.*

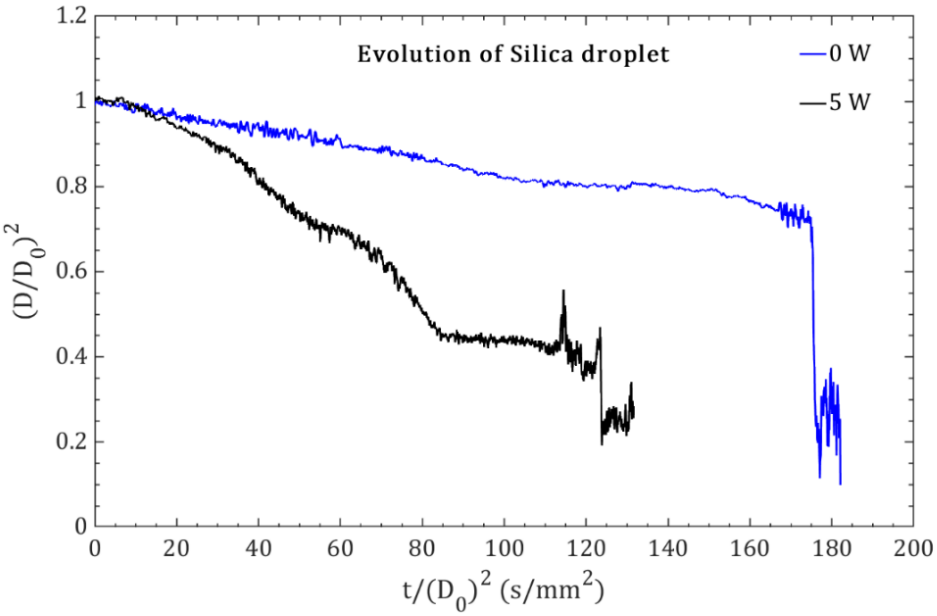

Figure 49. *Laser-induced evaporation of Silica droplet of D_0= 1.61 mm at 0 W and 5 W.*

The detailed temporal dynamics observed during the evaporation of silica droplets offer insights into the complex behavior and structural changes occurring within the droplet, highlighting the diverse stages involved in the evaporation process. Understanding these properties and behaviors is essential for harnessing the potential of silica droplets in various applications, including materials science, nanotechnology, and biotechnology, where precise control over droplet evaporation dynamics is crucial. Figure 49 presents a comparative analysis of the evaporation rate observed during the evaporation of silica droplets, both with and without the application of a laser. When comparing the two scenarios, distinct characteristics emerge. In the case of laser-induced evaporation, rapid evaporation initiates the process, leading to a gradual reduction in droplet size. Deformation in the axial direction follows, accompanied by nucleation events within the droplet, suggesting internal restructuring. Subsequent flattening of the droplet and ejection of fragments from its surface occur as heating continues, ultimately resulting in droplet fragmentation. In contrast, without laser assistance, the evaporation process may follow a slower trajectory, with potentially different morphological and kinetic characteristics. This comparison underscores the significant influence of external energy sources, such as laser heating, on the evaporation kinetics and behaviors of silica droplets. Understanding these differences is crucial for optimizing processes involving silica droplets, from materials synthesis to biotechnological applications.

7.5. Summary

The study examines the evaporation dynamics of cellulose nanocrystal (CNC), carboxyl methyl cellulose (CMC), and silica droplets, highlighting their distinct properties and behaviors. CNC droplets exhibit self-assembly into ordered structures, while CMC droplets form gel-like structures due to polymer chain entanglement. Silica droplets undergo rapid evaporation, deformation, nucleation, and fragmentation, influenced by external factors such as laser heating. CNC and CMC droplets may have slower evaporation rates compared to silica, with differences attributed to material composition and internal interactions. Understanding these properties and evaporation rates is crucial for optimizing processes and applications involving these droplets, from materials science to biotechnology, and tailoring them for specific needs in various industries.

8. Conclusions and future scope

8.1. Conclusions

This study investigates the opto-hydrodynamics phenomena triggered by single nanosecond and multiple femtosecond laser pulses, with a particular focus on laser-induced plasma formation, shock wave propagation, droplet deformation, expansion, bubble generation, and fragmentation in both single and multicomponent liquid droplets. Additionally, the study explores the laser-induced evaporation of cellulose nanomaterials. The findings are categorized into three distinct parts:

1. Nanosecond laser study:

The study examines droplet fragmentation using nanosecond laser-induced breakdown in single-component droplets, biofuels, and their emulsions. High-speed imaging reveals distinct temporal evolution patterns of atomization modes induced by focused laser pulses.

a. Single-component droplets primarily fragment through low-strength air entrapment and sheet breakup mechanisms, while biofuel emulsions exhibit higher breakup strength.
b. The addition of ethanol to biofuel (RME) enhances atomization efficiency, leading to the formation of smaller secondary droplets, which suggests improved fragmentation and atomization characteristics. This is suggesting the RME emulsions can be an alternative fuel sources for combustion devices.
c. As the sheet accelerates forward, holes begin to form and merge, resulting in intricate dynamics between the hole edges and surrounding material. This leads to fragmentation driven by Rayleigh-Taylor instabilities, where the droplet expands into a thin sheet that eventually ruptures due to the Rayleigh-Plateau instability.
d. Additionally, differences in properties between fuels, such as phase changes and viscosity, influence the extent and violence of breakup,

with iso-octane exhibiting wider expansion and more violent breakup compared to n-hexane.

2. Femtosecond laser study:

This study investigates the atomization of liquid droplets through laser-induced dynamics, focusing on two key phases: early-time bubble formation and late-time droplet breakup. Bubble diameter and breakup exhibit a logarithmic relationship with laser energy, regardless of the liquid. Lower laser energy levels produce smaller bubbles, while higher energy levels lead to earlier rupture of the film separating the expanding bubble from the atmosphere. Laser pulse energy and pulse number influence ligament generation and size distribution of micro-bubbles. Consecutive pulses induce strong interactions and coalescence of pulsating bubbles through the Bjerknes force, typically ranging from 0.2 to 1.5 mN, facilitated by a laser-induced acoustic field.

a. Initial stages involve bubble generation and droplet stretching, while later stages witness droplet breaking through sheet formation and catastrophic breakup, irrespective of laser energy.
b. Larger droplets or moderate laser energies result in late film rupture, causing less violent droplet acceleration and deformation into sheets. Sheet behavior depends on liquid surface tension and size, with smaller sheets collapsing back into droplets due to surface tension, while larger, thinner sheets are prone to rupture, forming Rayleigh-Plateau unstable liquid films.

3. Evaporation study:

The evaporation dynamics of cellulose nanocrystal (CNC), carboxyl methyl cellulose (CMC), and silica droplets are studied. CNC droplets demonstrate self-assembly into ordered structures, while CMC droplets form gel-like structures due to polymer chain entanglement. Silica droplets undergo rapid evaporation, deformation, nucleation, and fragmentation, influenced by external factors such as laser heating.

a. CNC and CMC droplets exhibit slower evaporation rates compared to silica. These differences are attributed to material composition and internal interactions within the droplets.
b. Understanding the distinct properties and evaporation rates of these droplets is crucial for optimizing processes and applications in various industries.

8.2. Future scope

Utilizing Laser-Induced Breakdown (LIB) techniques on both single and multicomponent liquid droplets enables the comprehensive study of their hydrodynamics and evaporation processes. This research can extend to real-time monitoring of dynamic phenomena in various environmental conditions, with applications spanning industries such as biomedical and pharmaceutical research. Moreover, the application of LIB can be expanded to investigate different types of biofuels, further enhancing its versatility and applicability. These advancements are poised to significantly enhance the precision and utility of LIB across scientific and industrial domains. In the realm of nanosecond laser studies, priorities include optimizing biofuel emulsions for improved combustion efficiency, refining high-speed imaging techniques for a deeper understanding of droplet fragmentation dynamics, and evaluating the environmental impacts of biofuel usage. Meanwhile, femtosecond laser studies offer opportunities to delve into bubble dynamics and coalescence, with potential applications in medicine and materials science, as well as precision material processing. In parallel, evaporation studies can focus on designing novel materials with tailored properties, optimizing industrial evaporation processes for increased efficiency, and exploring the influence of environmental factors on evaporation dynamics. Together, these research directions hold the promise of transformative advancements in fuel technology, materials science, environmental sustainability, and healthcare.

Appendix

By considering the initial volume of the drop $\alpha = \pi {D_0}^3/6$, the liquid volume constituting the sheet at time *t* is represented as [53]

$$\int_{R_0}^{R_{max}} 2\pi R h(R,t) dR = \alpha - \beta, \quad (1)$$

where $\beta = \int_0^t [2\pi R(t)\{u(R,t) - \dot{R}\} h(R,t)] dt$ is the net volume accumulated at time t on the rim. When applying momentum conservation at the rim, we consider a system analogous to the propulsion concept given by Tsiolkovsky (1903)[160]. It states that the rate of change of the rim inertia is equal to the sum of the momentum it absorbs plus the net force acting on it [53] expressed as

$$\frac{d}{dt}\left(mR * \dot{R}\right) = \varphi u(R,t) R - 2\sigma(R - R_0), \quad (2)$$

$$\varphi = \rho h R[u(R,t) - \dot{R}], \quad (3)$$

$$\text{With } \varphi = \frac{1}{R}\frac{d}{dt}(mR). \quad (4)$$

The velocity *u* (*R*, *t*) represents the liquid's velocity in the sheet at *R* = *R*(*t*). The force term $2\sigma(R - R_0)$ refers to the initial drop with a radius R_0, which becomes zero when $R = R_0$. Equation (3) and (4) represent the conservation of the mass. $\dot{m}R$ can be neglected because $\left|\dot{m}R/mR\right| \gg \left|\ddot{R}/\dot{R}\right|$ for all times. Hence equation (2) deduce to

$$\rho h R\left[u(R,t) - \dot{R}\right]^2 = 2\sigma\left(1 - \frac{R_0}{R}\right) \quad (5)$$

The terms used are

$$u(R,t) = -\frac{\dot{f}}{f(t)}(R - R_0) \text{ , where } \dot{f} = \frac{d\,f(t)}{dt} \quad (6)$$

$$h(R,t) = \frac{f(t)}{R} \quad (7)$$

$$\tau_c = \sqrt{\rho\,\alpha\,/6\,\sigma} \text{ , where } \alpha = \pi {D_0}^3/6$$

By considering above terms and from equations (1) and (5) modified equation is

$$f(t)[R(t) - R_0] = \frac{\alpha}{2\,\pi}\left(1 - \frac{t}{\tau_c}\right)^2 \quad (8)$$

Integrating the momentum equation (6.2.1) between $R = R_0$ and $R = R(t)$ with (6) for $u(R, t)$ and isobaric approximations, equation yields

$$\ddot{R} + \frac{6}{(\tau_c - t)^2}(R - R_0) + \frac{4}{\tau_c - t}\dot{R} = 0. \qquad (9)$$

Equation (9) reveals that the nonlinear dynamics of equations (6.2.1) and (6.2.2) lead to a linearly damped oscillatory motion of the sheet radius. This motion is characterized by a time-dependent frequency and damping factor, representing a balance between the initial drop's inertia and capillary restoring forces per Culick's law. The damping term arises from the ongoing transfer of momentum from the sheet to the rim. For the initial case, $R(0) = R_0$ and $\dot{R}(0) = u_0$, the radius of the expanding drop is modified as[53,54,110]

$$\frac{R(t) - R_0}{R_0} = \sqrt{\frac{2\,We_d}{3}}\,\frac{t}{\tau_c}\left(1 - \frac{t}{\tau_c}\right)^2. \qquad (10)$$

This explains an asymmetric on-period oscillatory motion that fits well for various Weber numbers and has a duration of the period $\tau_c = \sqrt{\rho {D_0}^3/6\sigma}$. The rescaled Weber number, $We_d = \frac{E_{k,d}}{E_{k,p}}\,We$ depends on the kinetic energy used for deformation which is expressed as the ratio of deformation to propulsion kinetic energies and corresponding Weber number [55].

$$\frac{E_{k,d}}{E_{k,p}} = \frac{\int_0^R {u_R}^2 h\, R\, dR}{U^2 \int_0^R h\, R\, dR} = \frac{R^2}{3U^2 t^2}$$

References

(1) Lefebvre, A. H. Properties of Sprays. *Part. Part. Syst. Charact.* **1989**, *6* (1–4), 176–186. https://doi.org/10.1002/ppsc.19890060129.

(2) Marmottant, P. H.; Villermaux, E. On Spray Formation. *J. Fluid Mech.* **2004**, *498*, 73–111. https://doi.org/10.1017/S0022112003006529.

(3) Lefebvre, A. H.; McDonell, V. G. *Atomization and Sprays*, 2nd ed.; Taylor & Francis, 2017.

(4) Reiter, G. Dewetting of Thin Polymer Films. *Phys. Rev. Lett.* **1992**, *68* (1), 75–80. https://doi.org/10.1140/epje/i2006-10057-5.

(5) Vernay, C.; Ramos, L.; Douzals, J. P.; Goyal, R.; Castaing, J. C.; Ligoure, C. Drop Impact Experiment as a Model Experiment to Investigate the Role of Oil-in-Water Emulsions in Controlling the Drop Size Distribution of an Agricultural Spray. *At. Sprays* **2016**, *26* (8), 827–851. https://doi.org/10.1615/AtomizSpr.2015013630.

(6) Rozhkov, A.; Prunet-Foch, B.; Vignes-Adler, M. Impact of Drops of Surfactant Solutions on Small Targets. *Proc. R. Soc. A Math. Phys. Eng. Sci.* **2010**, *466* (2122), 2897–2916. https://doi.org/10.1098/rspa.2010.0015.

(7) Thoroddsen, S. T.; Etoh, T. G.; Takehara, K. Crown Breakup by Marangoni Instability. *J. Fluid Mech.* **2006**, *557*, 63–72. https://doi.org/10.1017/S002211200600975X.

(8) Aljedaani, A. B.; Wang, C.; Jetly, A.; Thoroddsen, S. T. Experiments on the Breakup of Drop-Impact Crowns by Marangoni Holes. *J. Fluid Mech.* **2018**, *844*, 162–186. https://doi.org/10.1017/jfm.2018.178.

(9) Worthington A. M. *A Study of Splashes*; London: Longmans, Green, 1908.

(10) Rioboo, R. AAS 1102 (187-200).Pdf.

(11) Yarin, A. L.; Weiss, D. A. Impact of Drops on Solid Surfaces: Self-Similar Capillary Waves, and Splashing as a New Type of Kinematic Discontinuity. *J. Fluid Mech.* **1995**, *283*, 141–173.

https://doi.org/10.1017/S0022112095002266.

(12) Cossali, G. E.; Coghe, A.; Marengo, M. The Impact of a Single Drop on a Wetted Solid Surface. *Exp. Fluids* **1997**, *22* (6), 463–472. https://doi.org/10.1007/s003480050073.

(13) Wang, A. B.; Chen, C. C. Splashing Impact of a Single Drop onto Very Thin Liquid Films. *Phys. Fluids* **2000**, *12* (9), 2155–2158. https://doi.org/10.1063/1.1287511.

(14) Yarin, A. L. Drop Impact Dynamics: Splashing, Spreading, Receding, Bouncing.. *Annu. Rev. Fluid Mech.* **2006**, *38*, 159–192. https://doi.org/10.1146/annurev.fluid.38.050304.092144.

(15) Patil, N. D.; Bhardwaj, R.; Sharma, A. Droplet Impact Dynamics on Micropillared Hydrophobic Surfaces. *Exp. Therm. Fluid Sci.* **2016**, *74*, 195–206. https://doi.org/10.1016/j.expthermflusci.2015.12.006.

(16) Wang, X.; Xu, B.; Guo, S.; Zhao, Y.; Chen, Z. Droplet Impacting Dynamics: Recent Progress and Future Aspects. *Adv. Colloid Interface Sci.* **2023**, *317* (May). https://doi.org/10.1016/j.cis.2023.102919.

(17) Khojasteh, D.; Kazerooni, M.; Salarian, S.; Kamali, R. Droplet Impact on Superhydrophobic Surfaces: A Review of Recent Developments. *J. Ind. Eng. Chem.* **2016**, *42*, 1–14. https://doi.org/10.1016/j.jiec.2016.07.027.

(18) Josserand, C.; Thoroddsen, S. T. T.; Josserand, C.; Drop, S. T. T. T.; Annual, S. Drop Impact on a Solid Surface To Cite This Version : HAL Id : Hal-02172346 Drop Impact on a Solid. **2019**, *48* (1), 365–391. https://doi.org/10.1146/)).

(19) Prosperetti, A.; Oğuz, H. N. The Impact of Drops on Liquid Surfaces and the Underwater Noise of Rain. *Annu. Rev. Fluid Mech.* **1993**, *25* (1), 577–602. https://doi.org/10.1146/annurev.fl.25.010193.003045.

(20) Rein, M. Phenomena of Liquid Drop Impact on Solid and Liquid Surfaces. *Fluid Dyn. Res.* **1993**, *12* (2), 61–93. https://doi.org/10.1016/0169-5983(93)90106-K.

(21) Villermaux, E. Fragmentation. *Annu. Rev. Fluid Mech.* **2007**, *39*, 419–446.

https://doi.org/10.1146/annurev.fluid.39.050905.110214.

(22) Meyerand R. G.; F., H. A. L). *Phys. Rev. Lett.* **1963**, *11* (9), 401–403.

(23) A, R. S.; P, S. © 1964 Nature Publishing Group. *Nature* **1964**, *203* (4951), 1217–1219.

(24) Morgan c Grey. Laser-Induced Breakdown of Gases. *Reports Prog. Phys.* **1975**, *621*.

(25) Klein, A. L.; Bouwhuis, W.; Visser, C. W.; Lhuissier, H.; Sun, C.; Snoeijer, J. H.; Villermaux, E.; Lohse, D.; Gelderblom, H. Drop Shaping by Laser-Pulse Impact. *Phys. Rev. Appl.* **2015**, *3* (4), 1–6. https://doi.org/10.1103/PhysRevApplied.3.044018.

(26) Kennedy, P. K.; Hammer, D. X.; Rockwell, B. A. Laser-Induced Breakdown in Aqueous Media. *Prog. Quantum Electron.* **1997**, *21* (3), 155–248. https://doi.org/10.1016/S0079-6727(97)00002-5.

(27) Sinibaldi, G.; Occhicone, A.; Alves Pereira, F.; Caprini, D.; Marino, L.; Michelotti, F.; Casciola, C. M. Laser Induced Cavitation: Plasma Generation and Breakdown Shockwave. *Phys. Fluids* **2019**, *31* (10), 103302 (1-12). https://doi.org/10.1063/1.5119794.

(28) Noack, J.; Vogel, A. Laser-Induced Plasma Formation in Water at Nanosecond to Femtosecond Time Scales: Calculation of Thresholds, Absorption Coefficients, and Energy Density. *IEEE J. Quantum Electron.* **1999**, *35* (8), 1156–1167. https://doi.org/10.1109/3.777215.

(29) Rao, D. C. K.; Singh, A. P.; Basu, S. Laser-Induced Deformation and Fragmentation of Droplets in an Array. *Int. J. Multiph. Flow* **2022**, *148* (September 2021), 103925. https://doi.org/10.1016/j.ijmultiphaseflow.2021.103925.

(30) Yuen, M. C.; Chen, L. W. Heat-Transfer Measurements of Evaporating Liquid Droplets. *Int. J. Heat Mass Transf.* **1978**, *21* (5), 537–542. https://doi.org/10.1016/0017-9310(78)90049-2.

(31) Li, M. C.; Liu, X.; Lv, K.; Sun, J.; Dai, C.; Liao, B.; Liu, C.; Mei, C.; Wu, Q.; Hubbe, M. Cellulose Nanomaterials in Oil and Gas Industry: Current

Status and Future Perspectives. *Prog. Mater. Sci.* **2023**, *139* (January), 101187. https://doi.org/10.1016/j.pmatsci.2023.101187.

(32) Islam, M. S.; Chen, L.; Sisler, J.; Tam, K. C. Cellulose Nanocrystal (CNC)-Inorganic Hybrid Systems: Synthesis, Properties and Applications. *J. Mater. Chem. B* **2018**, *6* (6), 864–883. https://doi.org/10.1039/c7tb03016a.

(33) Trache, D.; Tarchoun, A. F.; Derradji, M.; Hamidon, T. S.; Masruchin, N.; Brosse, N.; Hussin, M. H. *Nanocellulose: From Fundamentals to Advanced Applications*; 2020; Vol. 8. https://doi.org/10.3389/fchem.2020.00392.

(34) Lau, H. C.; Yu, M.; Nguyen, Q. P. Nanotechnology for Oilfield Applications: Challenges and Impact. *J. Pet. Sci. Eng.* **2017**, *157* (July), 1160–1169. https://doi.org/10.1016/j.petrol.2017.07.062.

(35) Debye P. D e r Lichtdruck Awf Ew g e l N. *Optik (Stuttg).* **1907**.

(36) Roosen, G. A Theoretical and Experimental Study of the Stable Equilibrium Positions of Spheres Levitated by Two Horizontal Laser Beams. *Opt. Commun.* **1977**, *21* (1), 189–194. https://doi.org/10.1016/0030-4018(77)90107-9.

(37) Hee K. Park, Costas P. Grigoropoulos, Wing P. Leung, A. C. T. A Practical Excimer Laser-Based Cleaning Tool For Removal Of Surface Contaminants. *IEEE Trans. Components Packag. Manuf. Technol. Part A* **1994**, *17* (4), 631–643. https://doi.org/10.1109/95.335050.

(38) Vogel, A.; Schweiger, P.; Frieser, A.; Asiyo, M.; Birngruber, R. Working Mechanisms, Damage Range, and Reduction of Collateral Effects in Intraocular Nd:YAG Laser Surgery. *Fortschritte der Ophthalmol.* **1990**, *87* (6), 675–687.

(39) Shangguan, H. Q.; Casperson, L. W.; Shearin, A.; Gregory, K. W.; Prahl, S. A. Drug Delivery with Microsecond Laser Pulses into Gelatin. *Opt. InfoBase Conf. Pap.* **1998**, *35* (19), 287–297. https://doi.org/10.1364/ao.35.003347.

(40) Di, J.; Kim, J.; Hu, Q.; Jiang, X.; Gu, Z. Spatiotemporal Drug Delivery

Using Laser-Generated-Focused Ultrasound System. *J. Control. Release* **2015**, *220*, 592–599. https://doi.org/10.1016/j.jconrel.2015.08.033.

(41) Oscillation, T.; Bubbles, C.; Stone, N. During Electrohydraulic Lithotripsy. **1997**, *11* (1), 55–61.

(42) Yavas, O.; Leiderer, P.; Park, H. K.; Grigoropoulos, C. P.; Poon, C. C.; Leung, W. P.; Do, N.; Tam, A. C. Optical and Acoustic Study of Nucleation and Growth of Bubbles at a Liquid-Solid Interface Induced by Nanosecond-Pulsed-Laser Heating. *Appl. Phys. A Solids Surfaces* **1994**, *58* (4), 407–415. https://doi.org/10.1007/BF00323618.

(43) Park, B.-S.; Armstrong, R. L. Laser Droplet Heating: Fast and Slow Heating Regimes. *Appl. Opt.* **1989**, *28* (17), 3671. https://doi.org/10.1364/ao.28.003671.

(44) Skripov, P. V.; Skripov, A. P. The Phenomenon of Superheat of Liquids: In Memory of Vladimir P. Skripov. *Int. J. Thermophys.* **2010**, *31* (4–5), 816–830. https://doi.org/10.1007/s10765-010-0738-4.

(45) P., C. V. *Liquid-Vapor Phase Change Phenomenon*, 3rd ed.; Taylor & Francis, 1992; Vol. 1560320745.

(46) Sigrist, M. W.; Kneubohl, F. K. Laser-Generated Stress Waves in Liquids. *J. Acoust. Soc. Am.* **1978**, *64* (6), 1652–1663. https://doi.org/10.1121/1.382132.

(47) Teng, P.; Nishioka, N. S.; Anderson, R. R.; Deutsch, T. F. Optical Studies of Pulsed-Laser Fragmentation of Biliary Calculi. *Appl. Phys. B Photophysics Laser Chem.* **1987**, *42* (2), 73–78. https://doi.org/10.1007/BF00694813.

(48) Rayleigh, Lord. VIII. On the Pressure Developed in a Liquid during the Collapse of a Spherical Cavity . *London, Edinburgh, Dublin Philos. Mag. J. Sci.* **1917**, *34* (200), 94–98. https://doi.org/10.1080/14786440808635681.

(49) Vogel A., L. W.; Timm, R. Optical and Acoustic Investigations of the Dynamics of Laser-Produced Cavitation Bubbles near a Solid Boundary. *J. Fluid Mech.* **1989**, *206*, 299–338.

https://doi.org/10.1017/S0022112089002314.

(50) Do, N.; Klees, L.; Tam, A. C.; Leung, P. T.; Leung, W. P. Photodeflection Probing of the Explosion of a Liquid Film in Contact with a Solid Heated by Pulsed Excimer Laser Irradiation. *J. Appl. Phys.* **1993**, *74* (3), 1534–1538. https://doi.org/10.1063/1.354853.

(51) Gannena, K. S. R.; Rao, D. C. K.; Roy, D.; Kumar, A.; Basu, S. Bubble Dynamics and Atomization in Evaporating Polymeric Droplets. *J. Fluid Mech.* **2022**, *951* (November). https://doi.org/10.1017/jfm.2022.894.

(52) Taylor, P.; Oolman, T. O.; Blanch, H. W. Bubble Coalescence in Stagnant Liquids. **2007**, No. August 2013, 37–41.

(53) Villermaux, E.; Bossa, B. Drop Fragmentation on Impact. *J. Fluid Mech.* **2011**, *668*, 412–435. https://doi.org/10.1017/S002211201000474X.

(54) Klein, A. L.; Kurilovich, D.; Lhuissier, H.; Versolato, O. O.; Lohse, D.; Villermaux, E.; Gelderblom, H. Drop Fragmentation by Laser-Pulse Impact. *J. Fluid Mech.* **2020**, *893* (A7), 1–36.

(55) Gelderblom, H.; Lhuissier, H.; Klein, A. L.; Bouwhuis, W.; Lohse, D.; Villermaux, E.; Snoeijer, J. H. Drop Deformation by Laser-Pulse Impact. *J. Fluid Mech.* **2016**, *794*, 676–699. https://doi.org/10.1017/jfm.2016.182.

(56) Sacchi, C. A. Laser-Induced Electric Breakdown in Water. *J. Opt. Soc. Am. B* **1991**, *8* (2), 337. https://doi.org/10.1364/josab.8.000337.

(57) Glezer, E. N.; Schaffer, C. B.; Nishimura, N.; Mazur, E. Minimally Disruptive Laser-Induced Breakdown in Water. **1997**, *22* (23), 1817–1819.

(58) Fu, L.; Wang, S.; Xin, J.; Wang, S.; Yao, C.; Zhang, Z.; Wang, J. Experimental Investigation on Multiple Breakdown in Water Induced by Focused Nanosecond Laser. *Opt. Express* **2018**, *26* (22), 28560. https://doi.org/10.1364/oe.26.028560.

(59) Grigoryev, S. Y.; Lakatosh, B. V.; Krivokorytov, M. S.; Zhakhovsky, V. V.; Dyachkov, S. A.; Ilnitsky, D. K.; Migdal, K. P.; Inogamov, N. A.; Vinokhodov, A. Y.; Kompanets, V. O.; Sidelnikov, Y. V.; Krivtsun, V. M.; Koshelev, K. N.; Medvedev, V. V. Expansion and Fragmentation of a

Liquid-Metal Droplet by a Short Laser Pulse. *Phys. Rev. Appl.* **2018**, *10* (6), 064009 (1-15). https://doi.org/10.1103/PhysRevApplied.10.064009.

(60) Rao, D. C. K.; Mooss, V. S.; Mishra, Y. N.; Hanstorp, D. Controlling Bubble Generation by Femtosecond Laser-Induced Filamentation. *Sci. Rep.* **2022**, *12* (1), 1–16. https://doi.org/10.1038/s41598-022-20066-1.

(61) Labutin, T. A.; Lednev, V. N.; Ilyin, A. A.; Popov, A. M. Femtosecond Laser-Induced Breakdown Spectroscopy. *J. Anal. At. Spectrom.* **2016**, *31* (1), 90–118. https://doi.org/10.1039/c5ja00301f.

(62) Qi, P.; Su, Q.; Lin, L.; Liu, W. Bubble Dynamics Driven by a Few Successive Femtosecond Laser Pulses in Methanol under 1 KHz: Publisher's Note. *J. Opt. Soc. Am. B* **2018**, *35* (11), 2915. https://doi.org/10.1364/josab.35.002915.

(63) Geints, Y. E.; Zemlyanov, A. A. Phase Explosion of a Water Drop by a Femtosecond Laser Pulse: I. Dynamics of Optical Breakdown. *Atmos. Ocean. Opt.* **2009**, *22* (6), 581–589. https://doi.org/10.1134/S1024856009060037.

(64) Kotzagianni, M.; Couris, S. Femtosecond Laser Induced Breakdown for Combustion Diagnostics. *Appl. Phys. Lett.* **2012**, *100* (26), 264104 (1-4). https://doi.org/10.1063/1.4731781.

(65) Efimenko, E. S.; Malkov, Y. A.; Murzanev, A. A.; Stepanov, A. N. Femtosecond Laser Pulse-Induced Breakdown of a Single Water Microdroplet. *J. Opt. Soc. Am. B* **2014**, *31* (3), 534–541. https://doi.org/10.1364/josab.31.000534.

(66) Jaouen, M.; Laplanche, G.; Rachman, A. Multiphoton Ionization in Hydrogen-like Atoms by Intense Linearly Polarized Light. *Phys. Lett. A* **1973**, *43* (2), 101–102. https://doi.org/10.1016/0375-9601(73)90564-1.

(67) Vaidyanathan, A.; Walker, T. W.; Guenther, A. H. The Relative Roles of Avalanche Multiplication and Multiphoton Absorption in Laser-Induced Damage of Dielectrics. *IEEE J. Quantum Electron.* **1980**, *16* (1), 89–93. https://doi.org/10.1109/JQE.1980.1070331.

(68) Bebb, H. B.; Gold, A. Multiphoton Ionization of Hydrogen and Rare-Gas Atoms. *Phys. Rev.* **1966**, *143* (1), 1–24. https://doi.org/10.1103/PhysRev.143.1.

(69) Crowell, R. A.; Bartels, D. M. Multiphoton Ionization of Liquid Water with 3.0-5.0 EV Photons. *J. Phys. Chem.* **1996**, *100* (45), 17940–17949. https://doi.org/10.1021/jp9610978.

(70) Kennedy, P. K. A First-Order Model for Computation of Laser-Induced Breakdown Thresholds in Ocular and Aqueous Media: Part I—Theory. *IEEE J. Quantum Electron.* **1995**, *31* (12), 2241–2249. https://doi.org/10.1109/3.477753.

(71) CLAUD10 DEMICHELIS. Laser Induced Gas Breakdown: A Bibiliographical Review. *IEEE J. Quantum Electron.* **1969**, *QE-5, No.4* (April), 188–201.

(72) Hanna, D. C. The Principles of Nonlinear Optics. *Optics & Laser Technology*. 1985, p 104. https://doi.org/10.1016/0030-3992(85)90011-8.

(73) Lauterborn, W. High-Speed Photography of Laser-Induced Breakdown in Liquids. *Appl. Phys. Lett.* **1972**, *21* (1), 27–29. https://doi.org/10.1063/1.1654204.

(74) Wood, C. F.; Leach, D. H.; Zhang, J.; Chang, R. K.; Barber, P. W. Time-Resolved Shadowgraphs of Large Individual Water and Ethanol Droplets Vaporized by a Pulsed CO_2 Laser. *Appl. Opt.* **1988**, *27* (11), 2279–2286. https://doi.org/10.1364/ao.27.002279.

(75) Zhang, J.; Lam, J. K.; Wood, C. F.; Chu, B.; Chang, R. K. Explosive Vaporization of a Large Transparent Droplet Irradiated by a High Intensity Laser. *Appl. Opt.* **1987**, *26* (22), 4731–4737. https://doi.org/10.1364/ao.26.004731.

(76) Lindinger, A.; Hagen, J.; Socaciu, L. D.; Bernhardt, T. M.; Wöste, L.; Duft Denis, Leisner, T. Time-Resolved Explosion Dynamics of H2O Droplets Induced by Femtosecond Laser Pulses. *Appl. Opt.* **2004**, *43* (27), 5263–5269. https://doi.org/10.1364/AO.43.005263.

(77) Liu, W.; Kosareva, O.; Golubtsov, I. S.; Iwasaki, A.; Becker, A.; Kandidov, V. P.; Chin, S. L. Femtosecond Laser Pulse Filamentation versus Optical Breakdown in H2O. *Appl. Phys. B Lasers Opt.* **2003**, *76* (3), 215–229. https://doi.org/10.1007/s00340-002-1087-1.

(78) Schaffer, C. B.; Brodeur, A.; Mazur, E. Laser-Induced Breakdown and Damage in Bulk Transparent Materials Induced by Tightly Focused Femtosecond Laser Pulses. *Meas. Sci. Technol.* **2001**, *12* (11), 1784–1794. https://doi.org/10.1088/0957-0233/12/11/305.

(79) Ahamer, C. M.; Pedarnig, J. D. Femtosecond Double Pulse Laser-Induced Breakdown Spectroscopy: Investigation of the Intensity Enhancement. *Spectrochim. Acta - Part B At. Spectrosc.* **2018**, *148* (May), 23–30. https://doi.org/10.1016/j.sab.2018.05.027.

(80) Zhang, C.; Tang, M.; Zhang, H.; Lu, J. Optical Breakdown during Femtosecond Laser Propagation in Water Cloud. *Opt. Express* **2019**, *27* (6), 8456–8475. https://doi.org/10.1364/oe.27.008456.

(81) Potemkin, F. V.; Mareev, E. I. Dynamics of Multiple Bubbles, Excited by a Femtosecond Filament in Water. *Laser Phys. Lett.* **2015**, *12* (1), 15405. https://doi.org/10.1088/1612-2011/12/1/015405.

(82) Abraham, E.; Minoshima, K.; Matsumoto, H. Femtosecond Laser-Induced Breakdown in Water: Time-Resolved Shadow Imaging and Two-Color Interferometric Imaging. *Opt. Commun.* **2000**, *176* (4), 441–452. https://doi.org/10.1016/S0030-4018(00)00547-2.

(83) Chaudhary, K.; Rizvi, S. Z. H.; Ali, J. Laser-Induced Plasma and Its Applications. *Plasma Sci. Technol. - Prog. Phys. States Chem. React.* **2016**. https://doi.org/10.5772/61784.

(84) Singh, J. P. and T. S. N. *Laser Induced Breakdown Spectroscopy*, 2nd ed.; Elsevier Science, 2007.

(85) Giovannini, A. Z.; Gambino, N.; Rollinger, B.; Abhari, R. S. Angular Ion Species Distribution in Droplet-Based Laser-Produced Plasmas. *J. Appl. Phys.* **2015**, *117* (3). https://doi.org/10.1063/1.4906277.

(86) Scheers, J.; Schupp, R.; Meijer, R.; Ubachs, W.; Hoekstra, R.; Versolato, O. O. Time- And Space-Resolved Optical Stark Spectroscopy in the Afterglow of Laser-Produced Tin-Droplet Plasma. *Phys. Rev. E* **2020**, *102* (1), 13204. https://doi.org/10.1103/PhysRevE.102.013204.

(87) Yanagida, T.; Nagano, H.; Wada, Y.; Yabu, T.; Nagai, S.; Soumagne, G.; Hori, T.; Kakizaki, K.; Sumitani, A.; Fujimoto, J.; Mizoguchi, H.; Endo, A. Characterization and Optimization of Tin Particle Mitigation and EUV Conversion Efficiency in a Laser Produced Plasma EUV Light Source. In *SPIE advanced lithography*; 2011; Vol. 7969, p 79692T. https://doi.org/10.1117/12.879189.

(88) Zhao, Z.; Li, W. Numerical Simulation of Laser-Produced Plasma Expansion on a Droplet Surface. *Sci. Rep.* **2023**, *13* (1), 1–12. https://doi.org/10.1038/s41598-023-31069-x.

(89) Brujan, E. Shock Wave Emission from Laser-Induced Cavitation Bubbles in Polymer Solutions. **2008**, *48*, 423–426. https://doi.org/10.1016/j.ultras.2008.02.001.

(90) Rosselló, J. M.; Reese, H.; Raman, K. A.; Ohl, C. D. Bubble Nucleation and Jetting inside a Millimetric Droplet. *J. Fluid Mech.* **2023**, *968*, 1–35. https://doi.org/10.1017/jfm.2023.542.

(91) Delale, C. F. *Bubble Dynamics and Shock Waves*; 2013. https://doi.org/10.1007/978-3-642-34297-4.

(92) Emmony, D. C.; Siegrist, M.; Kneubühl, F. K. Laser-Induced Shock Waves in Liquids. *Appl. Phys. Lett.* **1976**, *29* (9), 547–549. https://doi.org/10.1063/1.89179.

(93) Tagawa, Y.; Yamamoto, S.; Hayasaka, K.; Kameda, M. On Pressure Impulse of a Laser-Induced Underwater Shock Wave. *J. Fluid Mech.* **2016**, *808*, 5–18. https://doi.org/10.1017/jfm.2016.644.

(94) Jang, D.; Oh, J. H.; Jong-Myoung; Kim, D. Enhanced Efficiency of Laser Shock Cleaning Process by Geometrical Confinement of Laser-Induced Plasma □. *J. Appl. physicsapplied Phys.* **2009**, *014913* (106).

https://doi.org/10.1063/1.3160315.

(95) Jang, D.; Park, J.-G.; Kim, D. Enhancement of Airborne Shock Wave by Laser-Induced Breakdown of Liquid Column in Laser Shock Cleaning □. *J. Appl. Phys.* **2011**, *073101* (109). https://doi.org/10.1063/1.3558989.

(96) Strycker, B. D.; M.M.Springer; A.J. Traverso, A.A.Kolomenskii, G.W.Kattawar, A. V. S. Femtosecond-Laser-Induced Shockwaves in Water Generated at an Air-Water Interface. *Opt. Express* **2013**, *21* (20), 23772–23784. https://doi.org/10.1117/12.808822.

(97) Hsiang, L. P.; Faeth, G. M. Drop Deformation and Breakup Due to Shock Wave and Steady Disturbances. *Int. J. Multiph. Flow* **1995**, *21* (4), 545–560. https://doi.org/10.1016/0301-9322(94)00095-2.

(98) Xu, Z.; Wang, T.; Che, Z. Droplet Deformation and Breakup in Shear Flow of Air. *Phys. Fluids* **2020**, *32* (5). https://doi.org/10.1063/5.0006236.

(99) Lim, K. Y.; Quinto-Su, P. A.; Klaseboer, E.; Khoo, B. C.; Venugopalan, V.; Ohl, C. D. Nonspherical Laser-Induced Cavitation Bubbles. *Phys. Rev. E - Stat. Nonlinear, Soft Matter Phys.* **2010**, *81* (1), 1–9. https://doi.org/10.1103/PhysRevE.81.016308.

(100) Venugopalan, V.; Guerra, A.; Nahen, K.; Vogel, A. Role of Laser-Induced Plasma Formation in Pulsed Cellular Microsurgery and Micromanipulation. *Phys. Rev. Lett.* **2002**, *88* (7), 781031–781034. https://doi.org/10.1103/PhysRevLett.88.078103.

(101) Nath, A.; Khare, A. Transient Evolution of Multiple Bubbles in Laser Induced Breakdown in Water. *Laser Part. Beams* **2011**, *29* (1), 1–9. https://doi.org/10.1017/S0263034610000662.

(102) Potemkin, F. V.; Mareev, E. I.; Podshivalov, A. A.; Gordienko, V. M. Highly Extended High Density Filaments in Tight Focusing Geometry in Water: From Femtoseconds to Microseconds. *New J. Phys.* **2015**, *17*, 053010(1-10). https://doi.org/10.1088/1367-2630/17/5/053010.

(103) Jukna, V.; Jarnac, A.; Milián, C.; Brelet, Y.; Carbonnel, J.; André, Y. B.; Guillermin, R.; Sessarego, J. P.; Fattaccioli, D.; Mysyrowicz, A.; Couairon,

A.; Houard, A. Underwater Acoustic Wave Generation by Filamentation of Terawatt Ultrashort Laser Pulses. *Phys. Rev. E* **2016**, *93* (6), 063106 (1-10). https://doi.org/10.1103/PhysRevE.93.063106.

(104) Jukna, V.; Albert, S.; Millon, C.; Mahieu, B.; Guillermin, R.; Rabau, G.; Fattaccioli, D.; Mysyrowicz, A.; Couairon, A.; Houard, A. Control of the Acoustic Waves Generated by Intense Laser Filamentation in Water. *Opt. Express* **2022**, *30* (6), 9103–9111. https://doi.org/10.1364/oe.453749.

(105) Zhang, H.; Chang, M.; Liu, F.; Li, S.; Jin, M. Rising Dynamics of Bubbles Generated by Femtosecond Laser Filamentation in Water. *Phys. Plasmas* **2022**, *29* (12), 123302 (1-7). https://doi.org/10.1063/5.0103593.

(106) Koukouvinis, P.; Gavaises, M.; Supponen, O.; Farhat, M. Simulation of Bubble Expansion and Collapse in the Vicinity of a Free Surface. *Phys. Fluids* **2016**, *28* (5). https://doi.org/10.1063/1.4949354.

(107) Raman, K. A.; Rosselló, J. M.; Reese, H.; Ohl, C. D. Microemulsification from Single Laser-Induced Cavitation Bubbles. *J. Fluid Mech.* **2022**, *953*, 1–24. https://doi.org/10.1017/jfm.2022.971.

(108) Zhong, X.; Eshraghi, J.; Vlachos, P.; Dabiri, S.; Ardekani, A. M. A Model for a Laser-Induced Cavitation Bubble. *Int. J. Multiph. Flow* **2020**, *132*, 103433. https://doi.org/10.1016/j.ijmultiphaseflow.2020.103433.

(109) Akhatov, I.; Lindau, O.; Topolnikov, A.; Mettin, R.; Vakhitova, N.; Lauterborn, W. Collapse and Rebound of a Laser-Induced Cavitation Bubble. *Phys. Fluids* **2001**, *13* (10), 2805–2819. https://doi.org/10.1063/1.1401810.

(110) Villermaux, E.; Clanet, C. Life of a Flapping Liquid Sheet. *J. Fluid Mech.* **2002**, *462*, 341–363. https://doi.org/10.1017/S0022112002008376.

(111) J. C. Lasheras; Hopfinger, E. J. LIQUID JET INSTABILITY AND ATOMIZATION IN A COAXIAL GAS STREAM. *Annu. Rev. Fluid Mech.* **2000**, *32* (2000), 275–308. https://doi.org/10.1146/annurev.genom.1.1.409.

(112) Bremond, N.; Villermaux, E. Bursting Thin Liquid Films. *J. Fluid Mech.*

2005, *524*, 121–130. https://doi.org/10.1017/S0022112004002411.

(113) Hirahara, H.; Kawahashi, M. Experimental Investigation of Viscous Effects upon a Breakup of Droplets in High-Speed Air Flow. *Exp. Fluids* **1992**, *13* (6), 423–428. https://doi.org/10.1007/BF00223250.

(114) A. A. Shraiber, A. M. Podvysotsky, and V. V. D. DEFORMATION AND BREAKUP OF DROPS BY AERODYNAMIC FORCES. *At. Sprays* **1996**, *6*, 667–692.

(115) Liu, Z.; Reitz, R. D. An Analysis of the Distortion and Breakup Mechanisms of High Speed Liquid Drops. *Int. J. Multiph. Flow* **1997**, *23* (4), 631–650. https://doi.org/10.1016/S0301-9322(96)00086-9.

(116) Joseph, D. D.; J. Belanger, Beavers, G. S. Breakup of a Liquid Drop Suddenly Exposed to a High-Speed Airstream. *Int. J. Multiph. Flow* **1999**, *25* (2), 1263–1303. https://doi.org/10.1016/j.ijmultiphaseflow.2003.11.004.

(117) Jalaal, M.; Mehravaran, K. Fragmentation of Falling Liquid Droplets in Bag Breakup Mode. *Int. J. Multiph. Flow* **2012**, *47*, 115–132. https://doi.org/10.1016/j.ijmultiphaseflow.2012.07.011.

(118) Theofanous, G. T.; Li, J. G. On the Physics of Aerobreakup. *Phys. Fluids* **2008**, *20* (5). https://doi.org/10.1063/1.2907989.

(119) Thoroddsen, S. T.; Takehara, K.; Etoh, T. G.; Ohl, C. D. Spray and Microjets Produced by Focusing a Laser Pulse into a Hemispherical Drop. *Phys. Fluids* **2009**, *21* (11), 1–15. https://doi.org/10.1063/1.3253394.

(120) Marmottant, P.; Villermaux, E. Fragmentaion of Stretched Liquid Ligaments. *Phys. Fluids* **2004**, *16* (8), 2732–2741. https://doi.org/10.1063/1.1756030.

(121) Dombrowski, N.; Fraser, R. P.; House, B.; Dombrowski, B. N. Ro· Yal Society of London a Photographic Investigation Into the Disintegration of Liquid Sheets a Photographic Investigation Into the Disintegrati on of Liquid Sheets. *Math. Phys. Sci.* **1954**, *247* (924), 101–130.

(122) Avila, S. R. G.; Ohl, C. D. Fragmentation of Acoustically Levitating Droplets by Laser-Induced Cavitation Bubbles. *J. Fluid Mech.* **2016**, *805*,

551–576. https://doi.org/10.1017/jfm.2016.583.

(123) Chaitanya Kumar Rao, D.; Basu, S. Phenomenology of Disruptive Breakup Mechanism of a Levitated Evaporating Emulsion Droplet. *Exp. Therm. Fluid Sci.* **2020**, *115*, 1–22. https://doi.org/10.1016/j.expthermflusci.2020.110086.

(124) Agbaglah, G. G. Breakup of Thin Liquid Sheets through Hole-Hole and Hole-Rim Merging. *J. Fluid Mech.* **2021**, *911*, 1–15. https://doi.org/10.1017/jfm.2020.1016.

(125) Ling, Y.; Fuster, D.; Zaleski, S.; Tryggvason, G. Spray Formation in a Quasiplanar Gas-Liquid Mixing Layer at Moderate Density Ratios: A Numerical Closeup. *Phys. Rev. Fluids* **2017**, *2* (1), 1–17. https://doi.org/10.1103/PhysRevFluids.2.014005.

(126) Schulkes, R. M. S. M. The Contraction of Liquid Filaments. *J. Fluid Mech.* **1996**, *309*, 277–300. https://doi.org/10.1017/S0022112096001632.

(127) Castrejón-Pita, A. A.; Castrejón-Pita, J. R.; Hutchings, I. M. Breakup of Liquid Filaments. *Phys. Rev. Lett.* **2012**, *108* (7), 15–19. https://doi.org/10.1103/PhysRevLett.108.074506.

(128) Hoepffner, J.; Paré, G. Recoil of a Liquid Filament: Escape from Pinch-off through Creation of a Vortex Ring. *J. Fluid Mech.* **2013**, *734*, 183–197. https://doi.org/10.1017/jfm.2013.472.

(129) Jagadale, V. S.; Rao, D. C. K.; Deshmukh, D.; Hanstorp, D.; Mishra, Y. N. Modes of Atomization in Biofuel Droplets Induced by a Focused Laser Pulse. *Fuel* **2022**, *315* (January), 123190. https://doi.org/10.1016/j.fuel.2022.123190.

(130) Jagadale, V. S.; Deshmukh, D.; Hanstorp, D.; Mishra, Y. N. Bubble Dynamics and Atomization of Acoustically Levitated Diesel and Biodiesel Droplets Using Femtosecond Laser Pulses. *Sci. Rep.* **2024**, *14* (1), 1–17. https://doi.org/10.1038/s41598-024-57802-8.

(131) Andrade, M. A. B.; Pérez, N.; Adamowski, J. C. Review of Progress in Acoustic Levitation. *Brazilian J. Phys.* **2018**, *48* (2), 190–213.

https://doi.org/10.1007/s13538-017-0552-6.

(132) Yarin, A. L.; Pfaffenlehner, M.; Tropea, C. On the Acoustic Levitation of Droplets. *J. Fluid Mech.* **1998**, *356*, 65–91.

(133) Marzo, A.; Barnes, A.; Drinkwater, B. W. TinyLev: A Multi-Emitter Single-Axis Acoustic Levitator. *Rev. Sci. Instrum.* **2017**, *88* (085105), 1–6. https://doi.org/10.1063/1.4989995.

(134) Foresti, D.; Nabavi, M.; Poulikakos, D. On the Acoustic Levitation Stability Behaviour of Spherical and Ellipsoidal Particles. *J. Fluid Mech.* **2012**, *709*, 581–592. https://doi.org/10.1017/jfm.2012.350.

(135) Meneses-Nava, M. A.; Rosas-Roman, I.; Barbosa-García, O.; Rodriguez, M.; Maldonado, J. L. Stability Evaluation of Water Droplets Levitated by a TinyLev Acoustic Levitator for Laser Induced Breakdown Spectroscopy. *Spectrochim. Acta - Part B At. Spectrosc.* **2020**, *168* (January), 105855. https://doi.org/10.1016/j.sab.2020.105855.

(136) Andrade, M. A. B.; Marzo, A. Numerical and Experimental Investigation of the Stability of a Drop in a Single-Axis Acoustic Levitator. *Phys. Fluids* **2019**, *31* (117101), 1–12. https://doi.org/10.1063/1.5121728.

(137) Rao, D. C. K.; Basu, S. Atomization Modes for Levitating Emulsified Droplets Undergoing Phase Change. *Exp. Fluids* **2020**, *61* (2), 1–20. https://doi.org/10.1007/s00348-019-2873-4.

(138) Gis, W.; Żółtowski, A.; Bocheńska, A. Properties of the Rapeseed Oil Methyl Esters and Comparing Them with the Diesel Oil Properties. *J. KONES Powertrain Transp.* **2011**, *18* (4), 121–127.

(139) Merkisz, J.; Fuć, P.; Lijewski, P.; Kozak, M. Rapeseed Oil Methyl Esters (RME) as Fuel for Urban Transport. In *Alternative Fuels, Technical and Environmental Conditions*; 2016; pp 23–39. https://doi.org/10.5772/62218.

(140) Hoekman, S. K.; Broch, A.; Robbins, C.; Ceniceros, E.; Natarajan, M. Review of Biodiesel Composition, Properties, and Specifications. *Renew. Sustain. Energy Rev.* **2012**, *16* (1), 143–169. https://doi.org/10.1016/j.rser.2011.07.143.

(141) Kiełczyński, P.; Ptasznik, S.; Szalewski, M.; Balcerzak, A.; Wieja, K.; Rostocki, A. J. Thermophysical Properties of Rapeseed Oil Methyl Esters (RME) at High Pressures and Various Temperatures Evaluated by Ultrasonic Methods. *Biomass and Bioenergy* **2017**, *107*, 113–121. https://doi.org/10.1016/j.biombioe.2017.09.015.

(142) Bach, C.; Schwabe, D. Surface Waves in Thermocapillary Flow–Revisited. *Eur. Phys. J. Spec. Top.* **2015**, *224* (2), 319–340. https://doi.org/10.1140/epjst/e2015-02363-5.

(143) Sogandares, F. M.; Fry, E. S. Absorption Spectrum (340-640 Nm) of Pure Water. *Appl. Opt.* **1997**, *36* (33), 8699–8709.

(144) Cabrera, H.; Marcano, A.; Castellanos, Y. Absorption Coefficient of Nearly Transparent Liquids Measured Using Thermal Lens Spectrometry. *Condens. Matter Phys.* **2006**, *9* (2), 385–389. https://doi.org/10.5488/CMP.9.2.385.

(145) Sadrolhosseini, A. R.; Moksin, M. M.; Nang, H. L. L.; Norozi, M.; Yunus, M. M. W.; Zakaria, A. Physical Properties of Normal Grade Biodiesel and Winter Grade Biodiesel. *Int. J. Mol. Sci.* **2011**, *12* (4), 2100–2111. https://doi.org/10.3390/ijms12042100.

(146) Gregorčič, R. P. and P. A Laser Probe Measurement of Cavitation Bubble Dynamics Improved by Shock Wave Detection and Compared to Shadow Photography. *J. Appl. Phys.* **2007**, *102*, 044909 (1-9).

(147) Kirkpatrick, R. D.; Lockett, M. J. The Influence of Approach Velocity on Bubble Coalescence. *Chem. Eng. Sci.* **1974**, *29* (12), 2363–2373. https://doi.org/10.1016/0009-2509(74)80013-8.

(148) Cain, F. W.; Lee, J. C. A Technique for Studying the Drainage and Rupture of Unstable Liquid Films Formed between Two Captive Bubbles: Measurements on KCl Solutions. *J. Colloid Interface Sci.* **1985**, *106* (1), 70–85. https://doi.org/10.1016/0021-9797(85)90382-0.

(149) Doinikov, A. A. Translational Motion of Two Interacting Bubbles in a Strong Acoustic Field. **2001**, *64* (February), 1–6.

https://doi.org/10.1103/PhysRevE.64.026301.

(150) Jiao, J.; He, Y.; Kentish, S. E.; Ashokkumar, M.; Manasseh, R.; Lee, J. Experimental and Theoretical Analysis of Secondary Bjerknes Forces between Two Bubbles in a Standing Wave. *Ultrasonics* **2015**, *58*, 35–42. https://doi.org/10.1016/j.ultras.2014.11.016.

(151) Ma, Y.; Zhang, G.; Ma, T. Ultrasonics Sonochemistry Interaction of Two Bubbles with Distortion in an Acoustic Field. *Ultrason. Sonochem.* **2022**, *84* (December 2021), 105953. https://doi.org/10.1016/j.ultsonch.2022.105953.

(152) Rao, D. C. K.; Karmakar, S.; Basu, S. Bubble Dynamics and Atomization Mechanisms in Burning Multi-Component Droplets. *Phys. Fluids* **2018**, *30* (6), 067101–067117. https://doi.org/10.1063/1.5035384.

(153) Culick, F. E. C. Journal of Applied Physics. *J. Appl. Phys.* **1960**, *31 (6)* (January 1960), 1128–1129.

(154) Swinscow, T. D. V.; Campbell, M. J. *Statistics at Square One*; 1996.

(155) Rao, D. C. K.; Karmakar, S.; Basu, S. Atomization Characteristics and Instabilities in the Combustion of Multi-Component Fuel Droplets with High Volatility Differential. *Sci. Rep.* **2017**, *7* (1), 1–15. https://doi.org/10.1038/s41598-017-09663-7.

(156) Joarder, R.; Gebel, G. C.; Mosbach, T. Two-Dimensional Numerical Simulation of a Decaying Laser Spark in Air with Radiation Loss. *Int. J. Heat Mass Transf.* **2013**, *63*, 284–300. https://doi.org/10.1016/j.ijheatmasstransfer.2013.03.072.

(157) Kobel, P.; Obreschkow, D.; De Bosset, A.; Dorsaz, N.; Farhat, M. Techniques for Generating Centimetric Drops in Microgravity and Application to Cavitation Studies. *Exp. Fluids* **2009**, *47* (1), 39–48. https://doi.org/10.1007/s00348-009-0610-0.

(158) Singh, A. P.; Padhi, U. P.; Joarder, R.; Roy, A. Spatio-Temporal Effect of the Breakdown Zone in the Laser-Initiated Ignition of Atomized Ethyl Alcohol-Air Mixture. *Appl. Energy* **2019**, *247* (September 2018), 140–154.

https://doi.org/10.1016/j.apenergy.2019.04.045.

(159) Phuoc, T. X. Laser-Induced Spark Ignition Fundamental and Applications. *Opt. Lasers Eng.* **2006**, *44* (5), 351–397. https://doi.org/10.1016/j.optlaseng.2005.03.008.

(160) Konstantin E. Tsiolkovsky. The Exploration of Cosmic Space by Means of Reaction Devices. *Rev. Sci. Phil. Lit.* **1903**, *5*, 1–23.

(161) Antkowiak, A.; Bremond, N.; Le Dizès, S.; Villermaux, E. Short-Term Dynamics of a Density Interface Following an Impact. *J. Fluid Mech.* **2007**, *577*, 241–250. https://doi.org/10.1017/S0022112007005058.

(162) Peters, I. R.; Tagawa, Y.; Oudalov, N.; Sun, C.; Prosperetti, A.; Lohse, D.; Van Der Meer, D. Highly Focused Supersonic Microjets: Numerical Simulations. *J. Fluid Mech.* **2013**, *719*, 587–605. https://doi.org/10.1017/jfm.2013.26.

(163) Kooij, S.; Sijs, R.; Denn, M. M.; Villermaux, E.; Bonn, D. What Determines the Drop Size in Sprays? *Phys. Rev. X* **2018**, *8* (3), 31019. https://doi.org/10.1103/PhysRevX.8.031019.

(164) Courbin, L.; Stone, H. A. Impact, Puncturing, and the Self-Healing. *Phys. Fluids* **2006**, *18* (9), 91105. https://doi.org/10.1063/1.2336102.

(165) Gilet, T.; Bush, J. W. M. The Fluid Trampoline: Droplets Bouncing on a Soap Film. *J. Fluid Mech.* **2009**, *625*, 167–203. https://doi.org/10.1017/S0022112008005442.

(166) Kim, I.; Wu, X. L. Tunneling of Micron-Sized Droplets through Soap Films. *Phys. Rev. E - Stat. Nonlinear, Soft Matter Phys.* **2010**, *82* (2), 1–8. https://doi.org/10.1103/PhysRevE.82.026313.

(167) PLATEAU, J. Statique Expérimentale et Théorique Des Liquides Soumis Aux Seules Forces Moléculaires / EXPERIMENTAL AND THE ORETICAL STATICS OF LIQUIDS - SUBJECT TO MOLECULAR FORCES ONLY. *Gauthier-Villars, Paris* **1873**.

(168) LIU, H.; JIN, X.; DING, B. Application of Nanotechnology in Petroleum Exploration and Development. *Pet. Explor. Dev.* **2016**, *43* (6), 1107–1115.

https://doi.org/10.1016/S1876-3804(16)30129-X.

(169) Calvino, C.; Macke, N.; Kato, R.; Rowan, S. J. Development, Processing and Applications of Bio-Sourced Cellulose Nanocrystal Composites. *Prog. Polym. Sci.* **2020**, *103*. https://doi.org/10.1016/j.progpolymsci.2020.101221.

(170) Nagy, S.; Fekete, E.; Móczó, J.; Koczka, K.; Csiszár, E. Heat-Induced Changes in Cellulose Nanocrystal/Amino-Aldehyde Biocomposite Systems. *J. Therm. Anal. Calorim.* **2020**, *142* (6), 2371–2383. https://doi.org/10.1007/s10973-020-10188-x.

(171) Tran, A.; Boott, C. E.; MacLachlan, M. J. Understanding the Self-Assembly of Cellulose Nanocrystals—Toward Chiral Photonic Materials. *Adv. Mater.* **2020**, *32* (41). https://doi.org/10.1002/adma.201905876.

(172) Jativa, F.; Schütz, C.; Bergström, L.; Zhang, X.; Wicklein, B. Confined Self-Assembly of Cellulose Nanocrystals in a Shrinking Droplet. *Soft Matter* **2015**, *11* (26), 5374–5380. https://doi.org/10.1039/c5sm00886g.

(173) Tran, A.; Hamad, W. Y.; MacLachlan, M. J. Fabrication of Cellulose Nanocrystal Films through Differential Evaporation for Patterned Coatings. *ACS Appl. Nano Mater.* **2018**, *1* (7), 3098–3104. https://doi.org/10.1021/acsanm.8b00947.

(174) Bruel, C.; Davies, T. S.; Carreau, P. J.; Tavares, J. R.; Heuzey, M. C. Self-Assembly Behaviors of Colloidal Cellulose Nanocrystals: A Tale of Stabilization Mechanisms. *J. Colloid Interface Sci.* **2020**, *574*, 399–409. https://doi.org/10.1016/j.jcis.2020.04.049.

(175) He, J.; Liu, S.; Li, L.; Piao, G. Lyotropic Liquid Crystal Behavior of Carboxylated Cellulose Nanocrystals. *Carbohydr. Polym.* **2017**, *164*, 364–369. https://doi.org/10.1016/j.carbpol.2017.01.080.

(176) Mu, X.; Gray, D. G. Formation of Chiral Nematic Films from Cellulose Nanocrystal Suspensions Is a Two-Stage Process. *Langmuir* **2014**, *30* (31), 9256–9260. https://doi.org/10.1021/la501741r.

(177) Klockars, K. Evaporation-Induced Self-Assembly of Cellulose

Nanocrystals from Aqueous Suspensions into Chiral Nematic Solid Structures. **2018**, No. May, 67.

(178) Habibi, Y.; Lucia, L. A.; Rojas, O. J. Cellulose Nanocrystals: Chemistry, Self-Assembly, and Applications. *Chem. Rev.* **2010**, *110* (6), 3479–3500. https://doi.org/10.1021/cr900339w.

(179) Li, H.; Shi, H.; He, Y.; Fei, X.; Peng, L. Preparation and Characterization of Carboxymethyl Cellulose-Based Composite Films Reinforced by Cellulose Nanocrystals Derived from Pea Hull Waste for Food Packaging Applications. *Int. J. Biol. Macromol.* **2020**, *164*, 4104–4112. https://doi.org/10.1016/j.ijbiomac.2020.09.010.

(180) Fernández-Santos, J.; Valls, C.; Cusola, O.; Roncero, M. B. Composites of Cellulose Nanocrystals in Combination with Either Cellulose Nanofibril or Carboxymethylcellulose as Functional Packaging Films. *Int. J. Biol. Macromol.* **2022**, *211* (January), 218–229. https://doi.org/10.1016/j.ijbiomac.2022.05.049.